DOCTOR OF PHILOSOPHY

Applications of Optical Manipulation for Low Cost Implementation, Beam Shaping and Biophysical Force Measurements

McDonald, Craig

Award date:
2017

Applications of Optical Manipulation for Low Cost Implementation, Beam Shaping and Biophysical Force Measurements.

Craig McDonald

A thesis submitted for the degree of

Philosophiæ Doctor (Ph.D.)

University of Dundee

Contents

1 Introduction to Optical Trapping **1**

1.1 Other micromanipulation methods 2

1.1.1 Physical probes 2

1.1.2 Dielectrophoretic traps 6

1.1.3 Magnetic tweezers 8

1.1.4 Acoustic manipulation 9

1.2 Optical tweezers 12

1.2.1 Radiation pressure 13

1.2.2 Optical guiding and the first radiation pressure trap . . 14

1.2.3 Optical levitation 15

1.2.4 Single beam gradient trap 16

1.2.5 Conservative vs non-conservative forces 17

1.3 Cutting edge systems 19

1.3.1 As a tool in life sciences 19

1.3.2 Measuring forces 19

1.3.3 Beam shaping techniques 20

1.4 Outline of thesis 21

2 Theoretical and Experimental Considerations **24**

2.1 Optical manipulation 25

2.1.1 Geometrical optics regime 26

2.1.2 Rayleigh regime 32

2.1.3 Intermediate regime 35
2.2 Experimental systems 36
2.2.1 Design considerations 37
2.3 Force measuring techniques 45
2.3.1 Displacement measurement - QPD vs camera 46
2.3.2 Trap stiffness measurement 52
2.4 Beam shaping 58
2.4.1 Static beam shaping 59
2.4.2 Dynamic beam shaping 60
2.5 Conclusion 64

3 Characterising Conical Refraction Optical Tweezers 65
3.1 Introduction to conical refraction 65
3.2 Overview of the theory of conical refraction 67
3.2.1 Optical classification of crystals 67
3.2.2 Conical refraction 68
3.3 Experimental system 75
3.4 Beam shape characterisation using beam profiler 76
3.5 Trap stiffness measurements 80
3.5.1 Levitation investigation 85
3.6 Conclusion and future work 88

4 HoloHands: Games Console Interface for Controlling Holographic Optical Manipulation 90
4.1 The need for control 90
4.2 Experimental system 93
4.3 Results and discussion 95
4.3.1 Efficiency measurements 99
4.4 Conclusion and future work 103

5 Examining the Effect of Kindlin-3 Binding Site Mutation on LFA-1 - ICAM-1 Bonds 106

5.1 Introduction to biological manipulation . . . 106
5.2 Introduction to integrin-ligand binding . . . 108
5.2.1 Leukocyte adhesion deficiency (LAD) . . . 111
5.2.2 TTT/AAA β2 integrin knock in mouse model . . . 112
5.3 Cell and bead preparation . . . 112
5.3.1 Effector T cell generation . . . 112
5.3.2 ICAM-1 bead coating . . . 113
5.4 Experimental system . . . 114
5.5 Cell adhesion under static conditions . . . 118
5.5.1 Single-beam adhesion program . . . 119
5.5.2 Single bond frequency . . . 119
5.5.3 WT vs KI bond strength . . . 121
5.6 Cell adhesion under shear flow . . . 124
5.6.1 CASBAH: Co-Aligned Single-Beam And Holographic optical trapping systems . . . 124
5.6.2 CASBAH adhesion program . . . 125
5.6.3 Binding under shear flow - proof of concept . . . 127
5.6.4 The future of CASBAH . . . 130
5.7 Conclusion . . . 132

6 Low-cost Optical Manipulation using Polymer Lenses and Bubble Wrap 134

6.1 Low-cost solutions for high-tech problems . . . 134
6.1.1 Repurposing materials . . . 136
6.2 Materials and methods . . . 137
6.2.1 Cell culture in bubble wrap . . . 137
6.2.2 Making trapping lens and curing with lamp . . . 138
6.2.3 Making imaging lens and combining with phone . . . 141
6.2.4 Illumination and optical tweezers setup assembly . . . 142

6.3 Results and discussion 144
6.3.1 Trapping in bubble wrap 144
6.3.2 Trapping cells in bubble wrap 144
6.3.3 Trapping with drip lens 146
6.3.4 Trapping with drip lens in bubble wrap 148
6.3.5 Imaging with drip lens and phone 149
6.4 Conclusion and future work 151

7 Conclusion and Outlook **154**
7.1 Discussion 154
7.2 Final thoughts 159

List of Figures

1.1 Micropipette adhesion assay. 3
1.2 Illustration of an AFM system. 5
1.3 Illustration of optoelectronic tweezers. 7
1.4 Ultrasonic standing wave trap. 11
1.5 Arthur Ashkin's First Experimental System 15

2.1 The three optical trapping regimes 26
2.2 Comparison of the theoretical trap stiffness in the three trapping regimes. 27
2.3 Trapping in x, y and z in the geometrical optics regime 29
2.4 Geometrical optics illustration of a sphere trapped in a single, Gaussian beam tweezers. 31
2.5 High NA focussing optics greatly contribute to axial gradient force 32
2.6 Trapping in the Rayleigh regime 34
2.7 A basic optical tweezers system 38
2.8 Köhler illumination 42
2.9 4f optical system for beam steering 44
2.10 Optical trapping as a Hookean spring 47
2.11 Position measurements using a QPD in BFPI mode 50
2.12 QPD calibration curve 52
2.13 Power spectrum of a 1 μm silica bead trapped in water 57

2.14 Schematic of an SLM 62

3.1 The seven crystal systems corresponding to optically isotropic, uniaxial or biaxial crystals. 69
3.2 Illustration of conical refraction in a crystal 70
3.3 Wave surface diagrams for a biaxial crystal 71
3.4 Conical refraction ray cone. 72
3.5 Basic structure of a conically refracted beam 73
3.6 Simulation of the intensity and polarisation distributions for a conically refracted beam 74
3.7 Experimental system used for conical refraction optical tweezers 77
3.8 Differing intensity patterns in beam spot when imaged in transmission and reflection mode 78
3.9 Beam profiles of circularly polarised, conically refracted beam with and without a trapped particle 79
3.10 Trap stiffness of a conically refracted beam as a function of trap power 81
3.11 Illustration of voltage vs time output from a QPD 82
3.12 The height of a 5.2 μm bead above the Lloyd/Poggendorff ring plane as a function of trap power. 86
3.13 An example power spectrum obtained for a 5.2 μm bead trapped in a Gaussian trap 87

4.1 Kinect controlled holographic optical tweezers setup. 94
4.2 Example of the HoloHands program. 96
4.3 Screenshot of Kinect controlled HOT, via the HoloHands program. 98
4.4 Two particles trapped with the HoloHands program. 98
4.5 Kinect control of two trapped particles. 99
4.6 Displacement vs. time graphs for three separate tracking events. 102

5.1 LFA-1 structure and conformations 109

5.2 β2 integrin activation due to kindlin-3 binding 110
5.3 Force measuring optical tweezers system used for static adhesion assays 115
5.4 Example power spectrum obtained for an optically trapped bead 116
5.5 Construction of a QPD calibration sample and trapping chambers. 117
5.6 Example calibration curve obtained during QPD calibration . 118
5.7 The five steps of a static adhesion measurement 120
5.8 Typical force versus time graph obtained for an integrin-ligand unbinding event 120
5.9 Unbinding force of integrin-ligand pairs for both WT and KI cells 122
5.10 Force measuring CASBAH system used for measuring cell adhesion under flow 126
5.11 CASBAH five step adhesion measurement of integrin-ligand binding under shear flow conditions 128
5.12 Integrin-ligand binding measurement under static conditions using the CASBAH system 129
5.13 Illustration of cell trapped with one and three optical traps . . 132

6.1 Steps used to fabricate a droplet lens. 140
6.2 Transmission spectrum of PDMS doped with Sudan II dye. . . 141
6.3 Experimental system used for low-cost optical tweezers based on hanging droplets of PDMS. 143
6.4 Trapping in bubble wrap using a high NA objective. 145
6.5 Airy disk produced by a PDMS droplet lens. 146
6.6 3.93 μm silica bead trapped with a PDMS droplet lens. 147
6.7 Imaging through the bubble wrap and meniscus. 149
6.8 Optically trapped effector T cell in bubble wrap. 150

6.9 Bead trapped with a clear PDMS droplet lens and imaged with a Sudan II doped PDMS droplet lens attached to a smartphone camera. 151

List of symbols

r	particle radius
λ	wavelength
n_p	refractive index of particle
n_m	refractive index of suspending medium
F_s	scattering force
F_g	gradient force
F	total force
P	laser power
c	speed of light
θ	angle of incidence
ϕ	angle of refraction
R	Fresnel reflection coefficient
T	Fresnel transmission coefficient
Q	efficiency of momentum transfer
I_0	incident intensity
m	relative refractive index of particle and suspending medium
α	polarisability of particle
$\mathbf{E}$	electric field
ω_0	Gaussian beam waist
d	smallest resolvable spot by microscope objective
k	trap stiffness
x	trapped particle displacement

$V_{1...4}$	output voltage for QPD quadrants
$V_{x,\,y,\,z}$	voltage position in x, y and z
β	QPD calibration constant
F_{Stokes}	Stokes' drag force
v	relative velocity of sphere and fluid
η	dynamic viscosity of medium
k_B	Boltzmann's constant
T	temperature
d	particle diameter
f	frequency
f_c	corner frequency
S_0	zero-frequency intercept of power spectrum
$S\,(f)$	power spectrum
γ	Stokes' drag coefficient
$\mathbf{D}$	Displacement vector
$\mathbf{k}$	Wavevector
$\mathbf{S}$	Poynting vector
D	Einstein's diffusion coefficient
N_b	Number of bonds
$P\,(N_b)$	Probability of given number of bonds forming

List of Abbreviations

2D	Two Dimensions
3D	Three Dimensions
AOD	Acousto-Optical Deflector
BFPI	Back Focal Plane Interferometry
CASBAH	Co-Aligned Single Beam And Holographic tweezer
CCD	Charge Coupled Device
CPU	Central Processing Unit
DAQ	Data Acquisition Card
DMD	Digital Mirror Device
DOE	Diffractive Optical Element
GPU	Graphics Processing Unit
HOT	Holographic Optical Tweezer
ICAM-1	Intercellular Adhesion Molecule 1
KI	Knock In
LAD	Leukocyte Adhesion Deficiency
LFA-1	Lymphocyte Function-associated Antigen 1
LG	Laguerre-Gaussian

NA	Numerical Aperture
P.B.S.	Phosphate Buffered Saline
PBS	Polarising Beam Splitter
PDMS	Polydimethylsiloxane
QPD	Quadrant Photodiode
SDK	Software Development Kit
SLM	Spatial Light Modulator
WT	Wild Type

Acknowledgements

While it is true that most Ph.D. projects rarely travel in a straight line, this is one Ph.D. which must have taken a few more scenic detours than others. First and foremost, I would like to thank my supervisor, Dr David McGloin, for always taking the time to answer my questions (stupid ones or otherwise), correct abstracts and generally being available, even if this means answering emails while on holiday. Also, David's patience with my "let's shoot a laser at it and see what happens" approach and ability to keep a straight face when pitching projects based on bubble wrap cannot be overstated.

Much of the work presented here has been a truly collaborative effort, and so my thanks must also be extended to Dr Susanna Fagerholm, my second supervisor. Explaining biology to a physicist cannot be an easy task (who knew cells aren't spherical?), but Susanna always took the time to explain things clearly and concisely, even after moving to Finland.

During my Ph.D. I was fortunate enough to work in a number of groups filled with some excellent researchers, who each contributed to my studies in their own way. Drs. Suman Anand, Giuseppe Smirne and Craig McDougall taught me everything I know about building, aligning and testing optical systems, as well as making pakora, brewing beer and flying kites. My thanks also go to Drs. Stella Corsetti, Yuri Belotti and Michael Conneely who were down in the trenches with me and helped make the whole experience much more enjoyable. Additionally, Dr Dan Burnham, who may have escaped the lab before I started but could not escape my emails about the software he left

behind and for providing useful advice and comments. Of course, Matthew MacPherson deserves a huge thank you for his work on the HoloHands project and for providing technical assistance for years after his time in our lab. On the biology side of things, Drs. Vicky Morrison, Matthew MacPherson and Hwee San Lek were always there to teach me all that I needed to know about dissection, cell culture and everything in between.

My thanks also extend to Dr Gary Callon, Grant Kydd, Stuart Anthony and Callum Moore, who always went above and beyond to provide technical assistance, repair broken electronics or supply an extended array of tools when the lab tool box was lacking.

I would also like to thank Prof. Dave Castner and Prof. Lara Gamble, as well as everyone else in the NESAC/BIO group at the University of Washington, for giving me the opportunity to spend a year with them, learning completely new applications of optical techniques.

Then there are the ones who I was not lucky enough to directly work with but nevertheless deserve my utmost thanks: Stephen Hogg for his many helpful discussions over many more games of MarioKart; Dr Graham Brodie for providing lots of insider information on how to complete an optics-based Ph.D. and pointing out design pitfalls before they became an issue; Dr Paul O'Mahoney for his knowledge of the colour wheel, his excellent cornflour and water mixing abilities and unparalleled ability to find the fun in experiments; and Dr Andrew Brown, for always getting the beers in.

On a more personal note, I want to thank my parents for their unfailing support and enthusiasm.

Last, but by no means least, I cannot thank my wife, Dr Hannah Aitchison, enough. For without her gentle (and sometimes not so gentle) nudging along the way, this whole ordeal would have been much harder.

Author's Declaration

I am the author of the work named in this document and hereby grant permission to the Library and Learning Centre administrators to make the work available as described.

I have exercised reasonable care to ensure that the work is original and to the best of my knowledge it does not break any UK law or infringe any third party's copyright or other Intellectual Property Right.

Signed (author) _____

Date _____

Supervisor's Declaration

As the supervisor of the above named author, I confirm that I agree with their requirements for restricting access and that, to the best of me knowledge, they have exercised reasonable care to ensure that the work is original and does not break any UK law or infringe any third party's copyright or other Intellectual Property Right.

Signed (supervisor) _____

Date _____

Abstract

There are a growing variety of research fields requiring non-contact micro-manipulation. An increasing number of these fields are turning to optical tweezers as a solution, owing to their high spatial and temporal resolution. Optical tweezers have the ability to quantitively exert and measure forces on the piconewton scale, a convenient force scale for soft biological materials, and are hugely versatile due to the wide assortment of beam shaping techniques that can be employed.

The work in this thesis can be broadly divided into two main themes: that quantifying the optical trapping forces in shaped beams; and bringing control and simplification of complex systems to non-expert users who may utilise optical tweezers as part of interdisciplinary collaborations.

Static beam shaping is used to generate a conically refracted optical trap and the trapping properties are characterised. It is shown that trapping in the lower Raman spot gives full, 3D gradient trapping, while the upper Raman spot allows for particle guiding due to its levitation properties. Particles in the Lloyd/Poggendorff rings experience a lower trap stiffness than particles in the lower Raman spot but benefit from rotational control.

Dynamic beam shaping techniques are exploited for the simplification of complex systems through the development and testing of the HoloHands program. This software allows a holographic optical tweezers experiment to be controlled by gestures that are detected by a Microsoft Kinect. Multiple particle manipulation is demonstrated, as well as a calibration of the tweezers system.

Application of trapping forces is demonstrated through an examination of integrin – ligand bond strength. Both wild type effector T cells and those with a kindlin-3 binding site mutation similar to that found in neutrophils from Leukocyte Adhesion Deficiency sufferers are investigated. Through the

use of back focal plane interferometry, a bond rupture force of (17.9 ± 0.6) pN at a force loading rate of (30 ± 4) pN/s, was measured for single integrins expressed on wild type cells. As expected, a significant drop in rupture force of bonds was found for mutated cells, with a measured rupture force of (10.1 ± 0.9) pN at the same pulling rate. Therefore, kindlin-3 binding to the cytoplasmic tail of the β2-tail directly affects bond strength of single integrin-ligand bonds. An experimental system for studying these cells under more physiologically relevant conditions is also presented.

Additionally, a low-cost optical micromanipulation system that makes use of simple microfabricated components coupled to a smartphone camera for imaging is proposed and demonstrated. Through the layering of hanging droplets of polydimethylsiloxane (PDMS) on microscope coverslips, lenses capable of optical trapping are created. Combination of PDMS with Sudan II dye led to the fabrication of long pass filters. An extension of this low-cost system into the life sciences is proposed through the adaptive use of bubble wrap, which allows for the culturing of cells in a chamber compatible with optical trapping.

Peer-Reviewed Publications

1. C. McDonald, M. McPherson, C. McDougall and D. McGloin *"Holo-Hands: games console interface for controlling holographic optical manipulation"* J. Opt. **15** (2013) 035708.

2. C. McDonald, C. McDougall, E. Rafailov and D. McGloin *"Characterising conical refraction optical tweezers"* Opt. Lett. **39** (2014) 6691 – 6694.

3. C. McDonald and D. McGloin *"Low-cost optical manipulation using hanging droplets of PDMS"* RSC Adv. **5** (2015) 55561 – 55565.

4. C. McDonald and D. McGloin *"Bubble wrap for optical trapping and cell culturing"* Biomed. Opt. Express. **6** (2015) 3757 – 3764.

Publications unrelated to this work:

1. S. Corsetti, R. E. H. Miles, C. McDonald, Y. Belotti, J. P. Reid, J. Kiefer and D. McGloin *"Probing the evaporation dynamics of ethanol/gasoline biofuel blends using single droplet manipulation techniques"* J. Phys. Chem. A, **119** (2015) 12797 – 12804.

Book Chapter

1. D. McGloin, C. McDonald and Y. Belotti "Colloidal interactions with optical fields: optical tweezers" in A. Fernandez-Nieves and A. M. Puertas (eds.) *Fluids, colloids and soft materials: an introduction to soft matter physics.* Hoboken, New Jersey: John Wiley & Sons, Inc., (2016) 111 – 130.

Chapter 1

Introduction to Optical Trapping

Throughout time, man has had a constant fascination with light. Historically shrouded in mystery and religion, most notably with the worship of "solar deities" by the ancient Egyptians, light has since "come out of the shadows" through the pioneering work of such people as Newton, Maxwell and Einstein. While this work has given a rigorous, scientific description of light, it would not be true to say that light is yet fully understood: controversies still abound regarding the interpretation of light [1] and many surprising properties of light are still being discovered [2].

Without this continued interest in light, many areas of research would have become dull and stagnant. The resolution of the humble microscope, for example, has improved from allowing us to observe the minute details on an insect, to providing insight in to the workings of the world on the micron-scale. This insight has led to the well known discovery, and further explanation of, Brownian motion. However, Brownian motion presents a significant problem in microscopy: how can one effectively study particles on a microscale if the particle in question is moving in a random fashion? Matters become worse still when the small depth of field and field of view of the high magnification microscope systems required are considered. Objects under study have a natural tendency to move, or sink or float within the sample,

making them difficult to study even briefly, never mind over significant time periods. With further advances in microscope resolution and the advent of nano-scale, super resolution fluorescence microscopy [3], particle localisation becomes much more of an issue.

Localisation allows for ease of interrogation, it enables repeatability to become a trivial part of experimental design, and offers the ability to disturb and probe particles in a controlled manner. Therefore, a suite of tools which allow for localisation on a microscale have been developed. Tools such as micromanipulators [4, 5], electrostatic traps [6, 7], dielectrophoretic traps [8, 9], microfluidic confinement [10, 11], acoustic manipulation [12, 13], magnetic tweezers [14, 15] and optical tweezers [16, 17] have all been developed, each with their own advantages and disadvantages and provide their own distinct approach to the problem of localisation. It is the latter of these tools, optical tweezers, which will form the focus of this thesis.

1.1 Other micromanipulation methods

Before focussing on optical tweezers, it is worth discussing some of the other prominent techniques that have been developed for micromanipulation and localisation, and highlighting their strengths and weaknesses when compared to optical trapping.

1.1.1 Physical probes

It could be argued that the most straightforward and intuitive of these techniques is through the use of a micromanipulator. Here, the sample in question is physically held by, for example, a micropipette, and moved through the use of a motorised stage, which could be performed by using stepper motors or piezoelectrics, or even a combination of the two to provide a long-range course adjust and a smaller range of fine positioning. In order to localise the particle of interest with a micropipette, one simply aspirates the sample

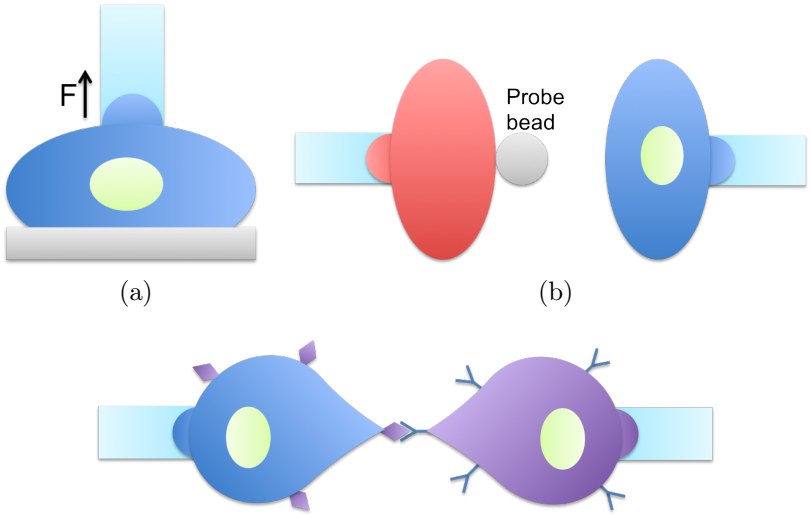

Figure 1.1: Micropipette adhesion assay probing (a) cell - surface, (b) cell - bead and (c) cell - cell interaction.

and holds the object of interest in the entrance to the pipette via the applied suction force. Micropipette aspiration is a widely used, direct force probing, technique for the measurement of the mechanical properties of single cells and has been used to probe the adhesion strength between cells and flat surfaces [18–20], figure 1.1(a), cells and beads [5, 21, 22], figure 1.1(b), and cells and other cells [23, 24], figure 1.1(c). In the case of the cell - surface and cell - bead interactions, the surface or bead are coated with the molecule under investigation. The force to be quantified can then be found by increasing the separation distance between the pipette holding the cell and adherent object and, if need be, increasing the applied aspiration force, until the bond breaks.

As illustrated by figure 1.1(b), when performing adhesion measurements between a cell and a coated bead, it is often advantageous to have a probe bead attached to the apex of an aspirated red blood cell, which acts as a picoforce transducer, in a technique known as biomembrane force probe

[24]. Essentially, the aspirated red blood cell is modelled as a soft spring that is holding the coated bead, similar to optical tweezers, see section 2.3 and chapter 5. By monitoring the deformation of the red blood cell as the pipettes are separated, one can calculate the force required to rupture the molecular bond formed between the cell in question and the coated bead. This technique has been used successfully to probe the energy landscape of receptor-ligand bonds [4] and to study the induction of T cell signalling [5]. However, it has been shown that there can be a discrepancy in measured values, especially with regards to cell elasticity, when using a micropipette based approach. This has been attributed to modification of the membrane associated proteins due to their inability to follow the membrane into the aspirating pipette and, therefore, accumulate at the entrance to the pipette [25, 26], a situation that would not occur with an optical tweezers based approach.

An extension of micromanipulators would be atomic force microscopes (AFM) which, although originally developed for imaging purposes, have proven their ability as a force measuring tool, notably in the life sciences [14, 27]. An AFM consists of a very sharp tip at the end of a cantilever, the back of which is illuminated by a laser that reflects onto a quadrant photodiode, as illustrated by figure 1.2. Piezoelectric elements are used to scan the tip in x and y with displacements of the tip in the z-axis, caused by the surface, translated into a change in position of the laser on the photodiode. By doing so, it is possible to acquire sub-molecular resolution images [28,29]. However, by functionalising the AFM tip and moving along the z-axis, it is possible to probe the binding force between a surface and the funtionalised tip and to record force-versus-extension curves [14]. Upon forming some form of bond between the surface and the tip, e.g. via a cell or single molecule, the AFM cantilever is moved away from the surface. Therefore, the cantilever will begin to bend, with its deflection recorded as a deflection in the illuminating laser, until the bond between tip and surface breaks, thus

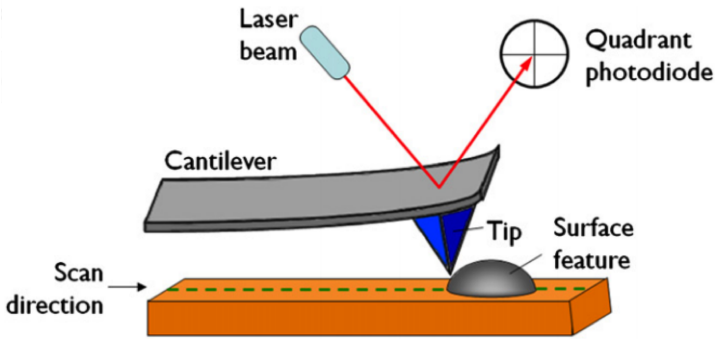

Figure 1.2: Illustration of an AFM system. Figure reproduced from [35].

giving a force measurement. In this way, the binding force of a single cell to coated surfaces has been investigated, with single molecule unbinding events measured [27, 30–32]. Additionally, the unfolding of single proteins has been investigated [33–35] by attaching one end of the protein to a surface and "picking up" the other end with the AFM tip before moving the tip away from the surface. The reverse of this procedure can also provide some valuable information: by pushing the AFM tip, often with an attached bead, into the surface, such as the surface of a cell, elasticity can be quantified [36].

Common to micromanipulator-style methods is that they require a mechanical probe to physically interact with the sample, thus limiting their useful force range to, for the AFM, greater than 10 pN, much higher than the subpiconewton force range accessible with optical tweezers [14]. Additionally, AFM is limited to force measurements only along one axis, which may not be the preferred axis to separate the objects under study. However, these methods are not without merit as they are able to exert much higher forces than optical tweezers, with similar spatial and temporal resolution [14].

It should be noted that while optical tweezers have the impressive ability and dexterity to manipulate objects on the nano-scale, the physical probe based technique Scanning Tunnelling Microscopy far outstrips them, with its unparalleled ability to manipulate individual atoms and create structures

than can confine electrons [37], a feat yet to be rivalled by optical manipulation.

1.1.2 Dielectrophoretic traps

Dielectrophoretic traps remove the physical connection to the sample by trapping polarisable particles in a nonuniform electric field [8, 9]. However, they require the prior fabrication of the electrodes used to generate the electric field, thus preventing them from being dynamically changed. That said, it is possible to scale the electrode arrays and create thousands of trap locations, as demonstrated by Gray *et al.* and their microelectrode array which trapped approximately $20,000$ cells in a 1 cm^2 grid, with single cell resolution [38]. Additionally, an interesting feature of dielectrophoretic traps is that they can be made size selective [39], a property not achievable with standard Gaussian beam optical tweezers but which requires sophisticated beam shaping techniques [40].

In order to circumvent the fixed trap constraint, light induced dielectrophoresis has been exploited to develop optoelectronic tweezers. Here, an electric potential is generated between two walls of the sample cell, one of which is a photovoltaic, optically addressable element. Illumination of the photoconductive plate, therefore, generates a non-uniform electric field, which traps and manipulates particles through the interaction with the induced dipole moments in both the particle and the surrounding medium [41]. The illuminating light will appear to repel the particle if the particle is less polarisable than its surroundings, as would be the case for a polystyrene bead in water, illustrated by figure 1.3 [41]. As such, light "walls" are required in order to confine the particle and, therefore, could benefit from the conically refracted beam generated in chapter 3, with the Lloyd/Poggendorff rings forming the "walls".

The photoconductive plate used in optoelectronic tweezers is typically fabricated from amorphous silicon for a number of reasons: it has a high

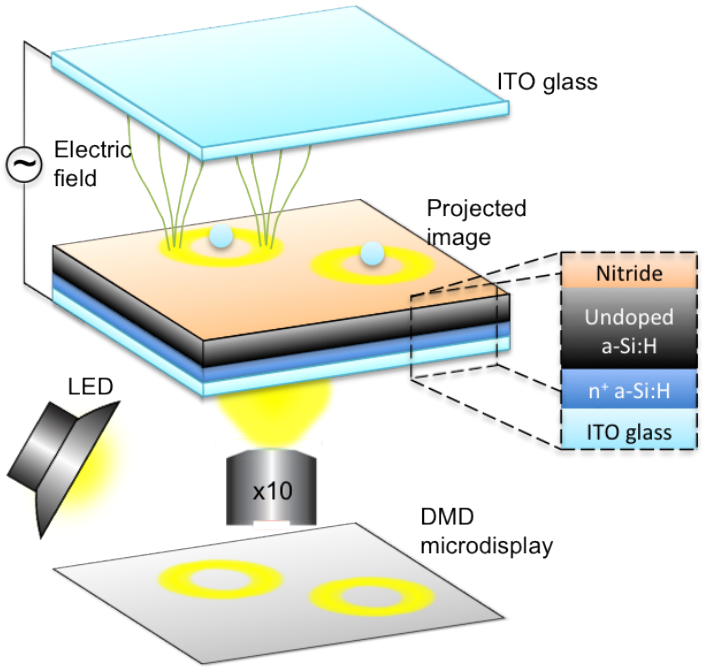

Figure 1.3: Illustration of experimental system for, and internal structure of, optoelectronic tweezers. Light from a light emitting diode (LED) is projected onto a photoconductive amorphous silicon (a-Si:H) electrode via a digital micromirror device (DMD) and microscope objective. The electric field is generated through the application of an a.c. bias between the electrodes. ITO, indium tin oxide. Image adapted from [41]

conductivity when illuminated, a high resistance when not illuminated, and it is cheap and easy to produce [41]. However, due to the finite photoconductivity of amorphous silicon, optoelectronic tweezers are unable to function in cell culture medium, or other high-conductivity media, thus rendering them unable to manipulate cells in physiologically relevant environments [42, 43]. By replacing the amorphous silicon plate with a phototransistor array, photoconductivity can be increased by over 500 times that of their amorphous silicon counterparts [43]. Through the use of this iteration of optoelectronic tweezers, trapping and manipulation of living cells in Phosphate Buffered Saline and Dulbecco's Modified Eagle's Medium has been demonstrated [43].

Optoelectronic tweezers can generate similar trapping forces to optical tweezers but at significantly less optical power, thus reducing the risk of photodamage to, and heating of, the sample [41]. Additionally, optoelectronic tweezers can manipulate large arrays of particles, and can be dynamically changed with something as simple as a data projector, providing a straightforward approach to multiplexing experiments [44–48]. However, unlike optical tweezers, optoelectronic tweezers cannot trap in three dimensions or be used to measure forces acting on the nanometre scale [49], so the work presented in chapter 5 would not be possible with such a device.

1.1.3 Magnetic tweezers

By using a pair of permanent magnets placed above the sample stage of a microscope one can construct a rudimentary set of magnetic tweezers, capable of not only trapping a paramagnetic particle in three dimensions but also rotating the particle [14]. Indeed, only a single magnet is required to apply a pulling force, i.e. towards the magnet, on a magnetic particle. Conceptually, magnetic tweezers are similar to optical tweezers, in so far as the particle in an applied field, in this case a magnetic field, experiences a force that is proportional to the gradient of the square of the field [14]. It follows that by creating steeper field gradients, one can generate higher forces, a

concept discussed for optical tweezers in chapter 2. Through the use of sharp electromagnetic tips or small permanent magnets, forces larger than 200 pN have been applied to micron-scale particles [50, 51]. Indeed, applied forces can be further increased by turning to electromagnetic tweezers, with applied forces of over 1 nN reported [14]. Unfortunately, forces which are based upon permanent magnets, while ideal for constant force experiments, cannot manipulate magnetic particles in three dimensions, thus lacking the dexterity optical tweezers offer. Electromagnetic tweezers can provide 3D control of a particle, but they require custom-made pole pieces and complex feedback control [14].

A consequence of the steep gradient used to generate these high forces is that the force falls off rapidly with distance from the magnet. Therefore, particles must remain close to the magnet in order to benefit from the high forces generated. Magnetic field strength can be increased through the use of larger magnets, however this results in a shallower field gradient which can vary on the order of millimetres. This variation is over a much larger length scale than the allowed movement of a tethered bead (on the order of microns) [15]. Consequently, the applied magnetic force can be assumed to be constant over a wide number of tethered beads, allowing for multiplexing of experiments [52]. Additionally, the ease with which particles can be rotated leads magnetic tweezers to naturally lend themselves to experiments involving the coiling and uncoiling of DNA [53, 54].

However, the type of particle that magnetic tweezers can manipulate is limited to paramagnetic particles and detection bandwidth and sensitivity is limited by the camera based detection used, which hinders the the direct measurement of very small or very fast bead displacements [14].

1.1.4 Acoustic manipulation

Optical tweezers are incredibly adept at the manipulation of micron sized particles, however, they begin to struggle with particle sizes above approx.

10 μm. Acoustic traps are able to manipulate much larger particles and exert much higher forces (nanonewtons) than their optical counterparts [55]. Additionally, acoustic manipulation lends itself to multiplexed force measurements, with force-extension measurements on thousands of biomolecules at once having been reported [13].

Particles within an ultrasonic field will experience a force acting upon them, with this force being predominantly higher in an ultrasonic standing wave than in a progressive wave [56, 57]. An ultrasonic standing wave trap can be created by placing an ultrasonic transducer and a reflective boundary on either side of a sample cell containing particles in a fluid, as illustrated by figure 1.4, and driving the transducer at a resonant frequency of the cavity, typically on the order of MHz [57]. In general, particles will migrate towards pressure nodes, figure 1.4(b), within the cavity due to axial radiation forces [57], although the inverse is true if the particle exhibits a negative acoustic contrast factor, as would be the case for a gas bubble in water [56,58]. Particles will then collect at certain points within the nodal planes due to weaker lateral radiation forces and secondary radiation forces due to particle-particle interaction [57]. The primary force acting on the particle scales as the cube of its radius, thus diminishing rapidly to forces comparable with optical manipulation forces, when particle size is reduced to sizes more in-line with optical trapping experiments, i.e. a few microns, [58]. It follows, therefore, that the larger forces achievable with acoustic manipulation can only be realised for larger particles. As particle sizes increase, so too does the force, in a rapid fashion, allowing for the trapping and manipulation of particle sizes unachievable with optical tweezers. Unfortunately, as size increases, so does particle mass, thus making larger particles more susceptible to sedimentation as they are at the mercy of their buoyancy in the surrounding fluid [58].

Although the ultrasonic standing waves described above do not lend themselves naturally to 3D manipulation, due to lack of lateral control of the standing wave, it is possible to exploit the differences in acoustic contrast,

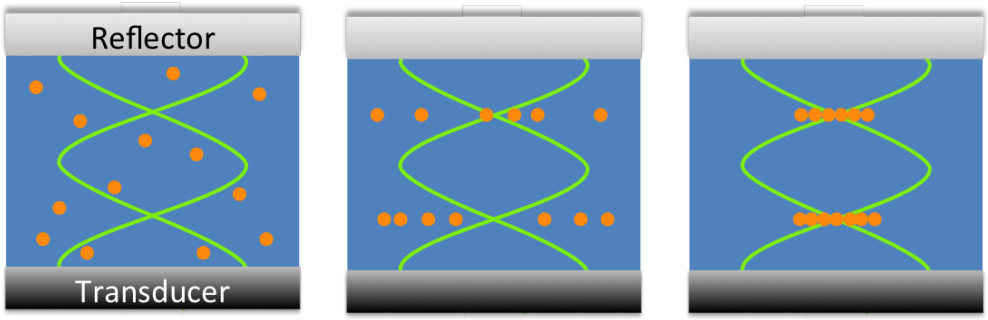

(a) (b) (c)

Figure 1.4: Ultrasonic standing wave trap showing movement of particles over time. (a) An ultrasonic standing wave is created by driving the transducer at the resonant frequency of the cavity. (b) The previously randomly distributed particles within the field move to pressure nodes, due to axial radiation forces, before (c) aggregating within the trapping planes due to lateral radiation and secondary forces. Image adapted from [57].

coupled with a flowing medium, to great effect. Termed acoustophoresis, literally meaning "migration with sound", it is possible to separate mixed samples by flowing them through acoustic standing waves, which has been demonstrated to be almost 100% efficient by Petersson *et al.* for the separation of lipids from red blood cells [59]. This technique has been built upon and cell and particle sorting, and particle sizing have since been demonstrated [58].

Lateral control of particles has been demonstrated through the use of an array based transducer [60], with the generation of the standing wave created by a subset of array elements and progressive shifting of the active elements in order to shift the standing wave location. Two dimensional control can be achieved by using a pair of matched transducers with a third levitating transducer [61]. In this case, one transducer levitates the particles axially, while the two matched transducers face each other and allow for manipulation of the trap location by tuning the relative phase of the two signals [61]. While the array based technique was able to move particles over 3 mm [60],

the latter technique achieved displacements of only 140 μm [61]. It should be noted that although displacements achievable with optical tweezers pale in comparison to the quoted figures, the fidelity of movement by acoustic methods is far outstripped by optical methods. Furthermore, acoustic waves have a much greater penetration depth in fluids and biological materials than light, leading acoustic trapping to be thought of as a complimentary, rather than competing, form of manipulation.

1.2 Optical tweezers

Following what was initially a "back of the envelope calculation" [62], and the publication of three seminal papers throughout the 1970s and 1980s [16, 63, 64], Arthur Ashkin not only created a new field of optical manipulation but gave the scientific community a new tool with which to examine the microscopic world. It was with the demonstration of the *single beam gradient force trap* by Ashkin *et al.* [16] that the field of optical trapping was firmly established and changed from a scientific curiosity to a useful tool. This new precision technique would go on to impact a myriad of sciences, spanning biological, chemical and physical, and encourage developments in related areas of research, such as optical beam shaping.

Around two decades after the first publication concerning optical manipulation, the field has begun revisiting the early experiments of Ashkin in the form of optical guiding [65], dual beam traps [66] and the manipulation of objects in air [67]. The work which is presented in this thesis contains elements of three of the four experiments first published by Ashkin, namely optical guiding, optical levitation and the gradient force trap, and so an understanding of the early experiments is not only historically interesting but serves as a foundation for the following chapters. To date, several thorough reviews of optical trapping exist in the literature [17, 62, 68–72], therefore an introduction, rather than an in-depth analysis, is presented.

1.2.1 Radiation pressure

Although considered to be the father of optical manipulation, Ashkin was not the first to observe the radiation pressure of light, nor is it a recent discovery. Radiation pressure of light was first proposed almost 400 years before Ashkin by Johannes Kepler. During his observations of planetary motion, for which he is best known, Kepler noted that the tail of a comet always points away from the sun. Kepler hypothesised that this "solar repulsion of comet tails [was] because of mechanical light force" [73] and went on to propose harnessing this force in order to sail from the Earth to the Moon on light itself [74]. The former was placed on a solid scientific foundation in 1873, with a rigorous mathematical description by James Clerk Maxwell [75], while the latter remained the stuff of science fiction until the demonstration of solar sails by the Japan Aerospace Exploration Agency and their IKAROS spacecraft [76]. Experimental validation of radiation pressure was provided at the turn of the twentieth century by Pyotr Lebedev [77], followed closely by Nichols and Hull later that same year [78], but received little attention in the following decades, possibly due to the complex experimental systems required, poor light sources available and difficulty in decoupling thermal forces caused by the light and radiation pressure forces from the light. It should be noted that Nichols and Hull made extensive mathematical errors when interpreting their results, giving values which deviated from Maxwell's theory by only 1% rather than the 10% discrepancy in results once the mistakes were corrected [79]. Radiation pressure of light was, therefore, resigned to a scientific curiosity rather than a technologically relevant tool.

However, armed with a microscope, the recently invented laser and a knowledge of the quantum nature of light [80], Ashkin revisited the question of radiation pressure of light. By considering interaction of light with a totally reflecting mirror, Ashkin realised that the photons striking the mirror must undergo a change in momentum. Through the conservation of momentum, there must be a transfer of momentum between the light and the mirror.

This results in the light imparting a small force on the mirror. While these femtonewton forces are negligible on large mirrors under everyday situations, Ashkin realised its potential if one was to focus the light on to a sufficiently small object. Assuming a perfectly reflecting 1 μm particle, with a density of 1 gcm^{-3}, Ashkin calculated that 1 W of 1 μm wavelength light, focussed to a spot size of approximately one wavelength, should accelerate the particle by 10^6 times the acceleration of gravity [62]. Even with the large approximations made, this should provide readily observable effects, so he tried a simple experiment to look for particle motion by radiation pressure.

1.2.2 Optical guiding and the first radiation pressure trap

Using just a few milliwatts of power and a weakly focussed Gaussian laser beam, Ashkin performed his first radiation pressure experiments in late 1969 [63]. As predicted, particles were guided, when illuminated, in the direction of propagation of the laser. This *scattering force*, as Ashkin named it, accelerated latex spheres across a glass cell until they became trapped against the glass at the opposite side, figure 1.5a. If the laser was blocked, the particles would wander off due to Brownian motion. Unexpectedly, however, if particles were illuminated off centre, they would be drawn into the high intensity region of the beam and accelerated in the direction of laser propagation. Named the *gradient force*, it would go on to form the basis of modern optical tweezers [62, 63].

Building on this optical guiding experiment, and his discovery of the two forces, Ashkin added a second, counter-propagating, laser to his system, figure 1.5b, therefore creating the first stable, three dimensional trap for neutral particles [63]. A latex sphere was drawn in to one laser beam, via the gradient force, and accelerated towards the other laser beam until an equilibrium position between the scattering force of each laser was reached. Any displacement of the sphere from this equilibrium position would generate

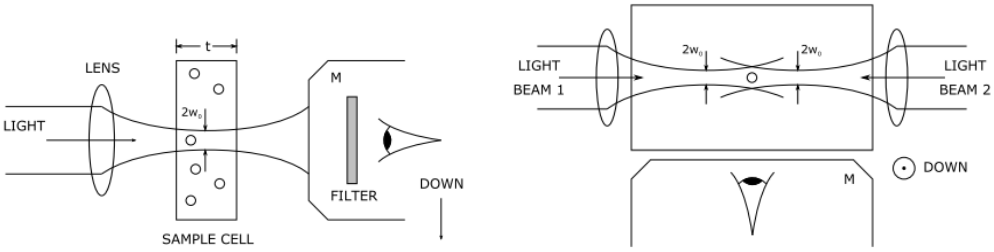

(a) (b)

Figure 1.5: Experimental system used by Ashkin for the first demonstration of acceleration of free particles by radiation pressure from a laser. Figure adapted from [63]

a restoring force, bringing the particle back to the trap position.

1.2.3 Optical levitation

Exploitation of the scattering force led Ashkin to the first demonstration of a single beam optical trap, termed the *optical levitation trap* in 1971 [64]. This trap consisted of a single optical beam, pointed vertically upwards, and trapped particles by balancing the scattering force against gravity acting on the particle, thus meaning that the trap was not purely optical. Equilibrium can be achieved because the scattering force decreases with distance from the focus of the beam, while the gradient force provides lateral confinement. The trapped particle will be accelerated upwards by the scattering force until a point is reached where the scattering force is equal and opposite to the gravitational force acting on the particle. By increasing the power in the trapping beam, the scattering force is increased and the height of the particle above the focus can be increased, allowing for experiments requiring particle guiding [81], until it eventually escapes. Owing to the delicate balance between optical power and gravity, these traps can often be quite unstable. Despite this instability, optically levitated objects are well suited for experiments that test our understanding of quantum limited measurements as they are

essentially free of suspension thermal noise due to their lack of mechanical supports [82–84].

1.2.4 Single beam gradient trap

Ashkin and colleagues then turned their attention to the gradient force produced by the laser light and, in 1986, demonstrated the *single beam gradient force trap*, which became widely known as *optical tweezers* [16]. By using a very tightly focussed laser beam, a strong optical gradient, and hence a strong gradient force, can be produced. If the beam is focussed tightly enough, generally by using a high (>1) numerical aperture microscope objective [17,85,86], the gradient force can overcome the scattering force, which is trying to push the particle from the trap, allowing for stable trapping in all three dimensions. Particles, therefore, are trapped in both the transverse (i.e. perpendicular to beam propagation) and longitudinal (i.e. along the beam propagation direction) planes. In order to help with this, optical tweezers are often designed with an inverted microscope design, utilising gravity to help counteract the scattering force. However, somewhat counter intuitively, the beam can point downwards and the particle will still be trapped, due to the magnitude of the gradient force. Nevertheless, work by Harris and McConnell have shown that, through exploiting temperature gradients as well as optical gradients, it is possible to optically trap cells with microscope objectives that have a numerical aperture as low as 0.4 [87].

Unlike the levitation trap, gradient based optical tweezers are not limited by gravity and can, therefore, impart much higher optical forces to the trapped particle before it escapes. This has led to optical tweezers dominating over their levitation counterparts when it comes to quantitative or precision based measurements.

1.2.5 Conservative vs non-conservative forces

There is a fundamental difference between the gradient and radiation forces and it is to do with the origin of each force. The scattering force arises from the transfer of momentum from the electric field to the particle due scattering and absorption by the illuminated particle [49]. Thus the scattering force can be described as being a non-conservative force as it is not possible to describe the scattering force through the use of potential energy wells. Therefore, the work done by the force in moving a particle between two points depends upon the path which is taken [88, 89]. The gradient force, however, can be described by a potential well and the work done by the force on the particle is independent of the path taken between two points [49, 89]. Therefore, the gradient force is a conservative force. How each of these forces arise will be discussed in more detail in chapter 2.1.

The difference between the conservative and non-conservative forces can be illustrated by comparing Ashkin's optical levitation experiments with his demonstration of the single beam gradient trap, described above. With optical levitation, in order to move the particle one simply increases the power in the trapping beam, thus pushing the particle away from the source while balancing against gravity, hence non-conservative [90]. However, in order to move the particle in the single beam gradient trap, which relies upon conservative forces, one must mechanically move the potential well created. Essentially, conservative forces generally allow you to trap a particle, while non-conservative forces would generally be used to propel a particle.

While the conservative force offers accurate positioning and larger forces, as demonstrated by chapter 5, non-conservative forces are not without their own appeal. For example, as demonstrated in the latter half of chapter 3, non-conservative forces allow for particle guiding over tens of microns simply by varying the power of the incident beam. Additionally, as non-conservative forces do not require the creation of a tightly focussed trapping spot, the optical levitation demonstrated in chapter 6 is achievable.

However, it should be noted that the idea of non-conservative and conservative forces does not only apply to optical tweezers but can be used when discussing other forms of micromanipulation. For example, the acoustic standing wave discussed above, section 1.1.4, traps particles in potential minima and hence exploits conservative forces. However, just as with optics (see the later half of chapter 3) acoustic manipulation also allows for the demonstration of non-conservative forces. This is most notable when discussing tractor beams, which, by definition, relies upon non-conservative forces to attract an object towards the source [89]. For example, a 2012 paper by Ruffner and Grier claimed to show an optical conveyor, generated by coherently superimposing coaxial Bessel beams and changing their relative phase in order to move trapped particles [91]. However, this was not a true tractor beam as the optical conveyor had intensity maxima which trapped the particles. Therefore, the particles were moved by moving the location of the intensity maxima, thus not acting as a true tractor beam. However, in 2014, Démoré *et al.* showed that it was possible to generate a true tractor beam, i.e. one which cannot be described by local potential minima and hence uses non-conservative forces, through the use of acoustic manipulation [92]. In the case of the tractor beam, it is a negative non-conservative force that is demonstrated as the particle is attracted towards the source [92]. However, positive non-conservative forces are also readily demonstrated, such as through the transfer of orbital angular momentum, also demonstrated by Démoré *et al. [93].*

While it is clear that non-conservative forces allow for the propulsion of particles, it is the conservative forces which are required for quantitative force measurements. This has allowed optical tweezers to develop into hi-tech, precision, force measuring tools, as discussed in the next section.

1.3 Cutting edge systems

1.3.1 As a tool in life sciences

Photonics and the life sciences have always had a close working relationship. For example, the earliest known published image taken with an optical microscope, a tool that has become ubiquitous in modern research labs, was that of Francesco Stelluti's bees [94]. Through their combination with optical tweezers, high end systems that give us the opportunity to study and probe life on a cellular, and sub-cellular, platform have been developed.

Optical tweezers can be used to exert piconewton forces and measure nanometre displacements, which are ideal force and positioning regimes with which to study biological systems. Significant studies into molecular motors [68, 95], cell membrane mechanics [26, 96] and DNA elasticity [97, 98] have been made possible due to the creation of optical traps. Through very little modification, a standard laboratory microscope can be transformed in to a tool which allows us to not only image but also manipulate biological samples in a sterile, non-contact manner. A entire "optical toolbox" has been created: biological samples can be moved, cut [99], fused [100, 101], rotated [102], stretched [96] and heated [103]. The refractive index [104] and elasticity [26] of cells can be probed in vitro, while neural circuit activity [105] and red blood cell flow in capillaries [106] have been studied in vivo.

1.3.2 Measuring forces

Having the ability to manipulate and examine microscopic objects is only half the battle - deforming an object by exerting a force is somewhat redundant if the applied force cannot be measured. Optical tweezers have come into their own as a quantitative tool. One of the main reasons that optical traps have found so many applications in the life sciences is that the force regime in which they operate is ideally suited for grabbing and manipulating soft

biological materials [14, 17, 72, 107]. However, the force measuring ability of optical tweezers have been exploited in a myriad of other fields, allowing for: the determination of a medium's viscosity [108]; the direct measurement of critical Casimir forces [109]; quantification of the colloidal attraction in a temperature gradient [110]; and an estimation of the interfacial tension of emulsion droplets through controlled deformation [111].

At the core of many of these techniques is an understanding of Brownian motion, an understanding which, over 100 years since Einstein's seminal paper on the subject [112], is still not complete [113]. Through quantitative measurements of force and displacement of trapped objects [114], made possible by three dimension position detection [115] (via a high-speed camera [116] or position sensitive photodiode [117]) coupled with a calibration of the trapping forces, optical tweezers can be used to study Brownian motion [118, 119] and try to provide solutions to some of these unanswered questions.

1.3.3 Beam shaping techniques

A traditional, standard, optical tweezers system relies on the focussing of a single beam of light, with a Gaussian intensity profile, through a high numerical aperture (NA) lens. However, the limits of what can be achieved by a single Gaussian trap are quickly reached. Recently, variations on single beam optical traps, based on beam shaping techniques, have appeared, further exploiting light's ability to exert force on an object. Bessel beams, a class of "non-diffracting" beams, have been used to guide particles over long distances [120] and to form an optical conveyor belt [91]. Laguerre-Gaussian (LG) beams have been created and used to induce spin in absorbing particles [121], due to the orbital angular momentum carried by the helical wave-front of the beam, while controlled rotation of particles was demonstrated through the interference of an LG beam with a plane wave [122]. Conically refracted beams have found use as "optical vaults" [123], to shield a

trapped particle from untrapped objects, and also have the impressive ability to trap, simultaneously, both high and low refractive index particles [124]. Indeed, many other beams that are solutions to the wave equation, and therefore propagate through space by imaging themselves, have their own distinct set of advantages and disadvantages in relation to optical tweezers [47, 125–129].

There are numerous techniques that are used for beam shaping and they are, broadly speaking, categorised into three groups depending upon the approach. Beam shaping methods utilise amplitude-only modulation, phase-only modulation or complex modulation of the beam - the latter alters both the phase and the amplitude of the light. Phase-only modulation, the more efficient of the three methods to implement dynamically, is generally the more popular option in the optical manipulation community as the power reaching the sample plane is often of great concern. Computer generated holograms have been used to create multi-beam traps [130], allowing for the manipulation of particles, in real time, in three dimensions, while acousto-optic deflectors utilise their high speed to time share the beam between multiple traps [131]. However, there has been a recent resurgence in interest in more passive beam shaping techniques, such as with a diffractive optical element (DOE) or a biaxial crystal, and its application in optical manipulation due to the high optical efficiency, low cost and comparative ease of implementation [123, 124, 132–136].

1.4 Outline of thesis

This thesis contains an investigation into the applications of optical tweezers, from characterising the optically trapping properties of a shaped beam through to the simplification of control and use of the system. Although each chapter will focus on a different application, the foundation of this thesis is firmly set in the theory, design and quantification of a basic optical

tweezers system. Therefore, chapter 2 will provide an introduction to the theory governing optical trapping, while also highlighting design and calibration considerations and techniques that can be exploited to change single Gaussian beams into more complex patterns.

Chapter 3 demonstrates the beam shaping discussed in the previous chapter through the creation of, and subsequent characterisation of, conical refraction optical tweezer. A discussion on the optical properties of crystals is provided, as it is through the use of a biaxial crystal that a conically refracted beam can be generated. After investigating the beam shape, it is shown, through the study of the trap's stiffness, that three distinct optical trapping regimes exist in a conical refraction optical tweezers system.

Having discussed static beam shaping, chapter 4 introduces dynamic beam shaping and shows that it can be used to simplify complex systems by providing an intuitive human-computer interface. As optical tweezers continue their spread from the optics lab and find more and more uses as tools in other areas of research, there is a pressing need for simplified user interfaces to allow for their use by "non-expert" users.

Optical tweezers really came in to their own as a quantitative tool in the life sciences, exerting and measuring forces on biological specimens. Chapter 5 continues this investigation in a similar vein through a study of the adhesion properties of primary murine effector T cells. By studying the force required to rupture integrin-ligand pairs from healthy, wild type mice and mice with a mutated gene, crucial information regarding Leukocyte Adhesion Deficiency can be obtained. Here, the force measuring techniques outlined in chapter 3 are extended to allow for the measurement of the piconewton forces applied when rupturing integrin-ligand bonds under static conditions, while the dynamic beam shaping discussed in chapter 4 is exploited to develop a system which aims to measure these rupture forces under shear flow.

The simplification of optical tweezers, as a whole, is needed for resource-limited settings as high-end systems also come with an associated high cost.

This can prevent their use in resource-limited or pedagogical settings, where laboratory grade equipment is required but the funding is unavailable. Chapter 6, therefore, presents a low-cost optical tweezers system based on simple microfabricated components coupled to a smartphone for imaging. By re-purposing equipment that is often found, discarded, in the laboratory, the trapping and imaging lenses of optical tweezers can be made, while their extension into the life sciences can be achieved through the adaptive use of bubble wrap.

Chapter 2

Theoretical and Experimental Considerations

"Optical tweezers" or "optical trapping" refers to using the intense optical field generated by an strongly focussed laser beam to hold and manipulate a microscopic particle in all three dimensions. It is the interaction between the particle and the strong optical gradient that generates an optically induced force. How the interaction between light and particle generates a force, and how this interaction is achieved, is the bedrock of optical trapping and many excellent reviews exist in the literature on these subjects [17, 69–72, 107]. A rigorous description of how the forces arise in optical tweezers is complex and only a general understanding, and appreciation, of the principles governing optical trapping is required for the work presented in this thesis. This chapter, therefore, provides a background for the reader, presenting a general introduction to how such trapping forces arise, outlined in section 2.1; what considerations must be made in the design of a trapping system, which is discussed in section 2.2; while section 2.3 deals with how such forces are measured.

2.1 Optical manipulation

Traditionally, optical trapping forces are divided into two distinct components: the scattering force, which pushes the particle in the direction of laser propagation, and the gradient force, which pulls the particle into high intensity regions [86]. A thorough mathematical description of the origin of these forces can be obtained by turning to electromagnetic scattering theory and performing a complete wave-optical modelling of the particle-light interaction [49]. However, particle size dependent approximations allow for substantial simplifications to the optical force calculations. The theoretical approximations of how these forces arise depends upon the size of the particle relative to the wavelength of the trapping light, the three trapping regimes are summarised in 2.1. Two distinct regimes are easily defined: a ray optics description is sufficient for the geometrical optics regime, where the particle radius is much larger than the wavelength of trapping light, $r \gg \lambda$, while the Rayleigh regime describes particles with a radius that is much smaller than the trapping light's wavelength, $r \ll \lambda$, as point dipoles. These approximations are not only useful for providing an intuitive description of optical trapping but also lend themselves to substantially simpler calculations which, as illustrated by figure 2.2, agree closely to the more intensive Mie theory, when considered within their appropriate size regimes.

A third, intermediate, trapping regime exists in the grey area between the previous two regimes, where particles have a radius that is approximately that of the trapping wavelength, $r \simeq \lambda$. As reflected in figure 2.2, the approximations mentioned above are no longer valid in this regime and one must turn to electromagnetic scattering theory in order to calculate the forces acting on the particle.

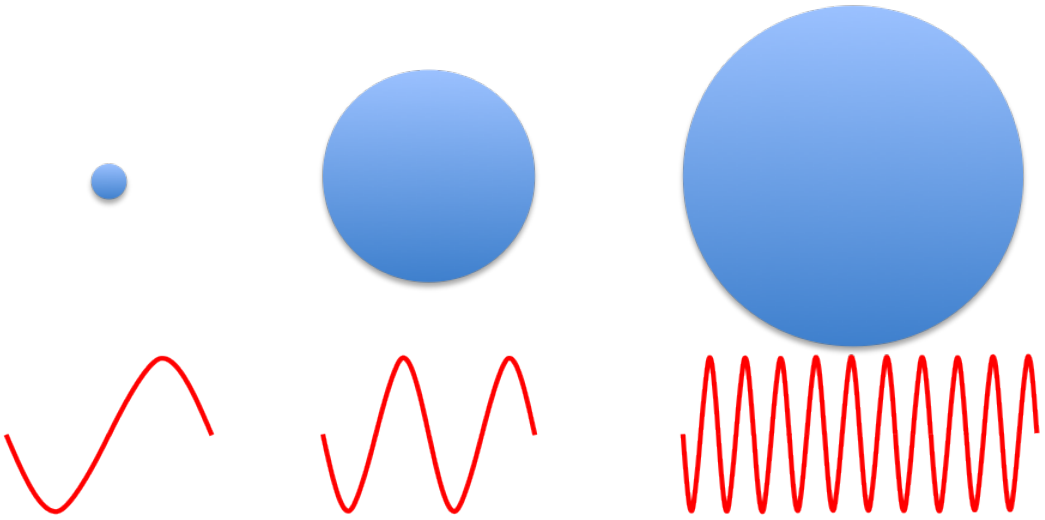

Figure 2.1: Illustration showing the three optical trapping regimes: (left) Rayleigh regime, $r \ll \lambda$. (centre) intermediate regime, $r \simeq \lambda$. (right) geometrical optics regime, $r \gg \lambda$. Image adapted from [137].

2.1.1 Geometrical optics regime

In the ray optics regime, the particle that is being trapped is much larger than the wavelength of the trapping light, $r \gg \lambda$. The wave, as a whole, has an effect on the particle and the scattering becomes independent of wavelength. Therefore, geometrical optics can be used to calculate the optical forces acting on the particle [86].

A simple model of a small dielectric sphere, with refractive index n_p, suspended in a medium with refractive index n_m, such that $n_p > n_m$, illuminated by a tightly focussed Gaussian laser beam, is sufficient to describe the trapping forces in the geometrical optics regime. The Gaussian beam can be approximated as a bundle of rays, with each ray weighted according to its intensity and carrying a momentum that is proportional to its intensity and the refractive index in which it is travelling. As dictated by Newton's third law, any change in the momentum of the rays of light, caused by interaction with the particle, requires an equal but opposite change in the momentum

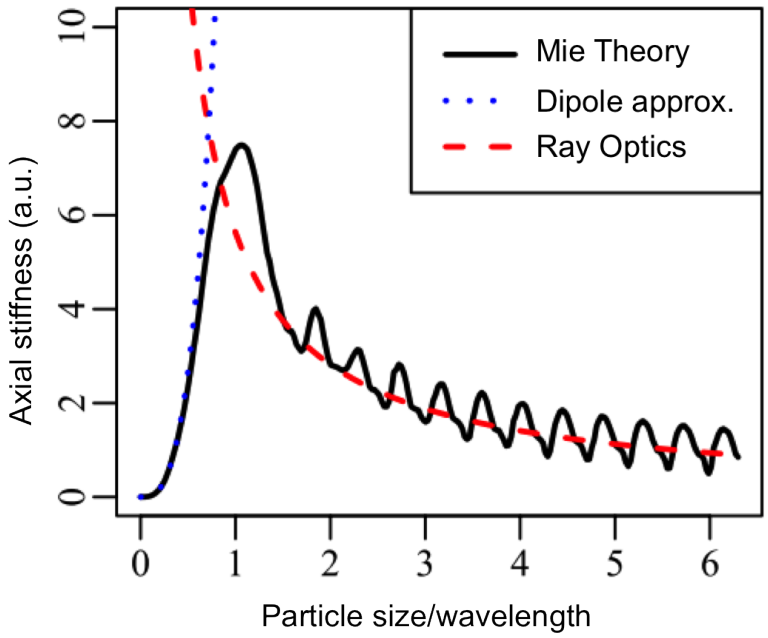

Figure 2.2: Comparison of the theoretical axial stiffness of an optical trap calculated using ray optics (red dashed line), the dipole approximation (blue dotted line) and Lorentz-Mie theory (solid black line). Note that while Lorentz-Mie theory is valid for the whole range, the two approximations only agree closely within their respective size regimes ($r \gg \lambda$ for ray optics and $r \ll \lambda$ for the dipole approximation). Image adapted from [72].

of the particle. This gives rise to a force acting on the particle. Some of the incident light will be reflected by the surface of the particle, according to the Fresnel equations [138] , producing a *scattering force* that acts in the direction of laser propagation.

Owing to its higher refractive index, upon illumination the particle will act as a small lens, causing incident light to be refracted according to Snell's law [138]. The transverse trapping plane is illustrated in figure 2.3a and shows that stronger, more intense, rays in the centre of the beam will experience a bigger momentum change than the weaker, less intense, rays at the edges of the beam when refracted by an off axis particle. Thus, the particle will experience a strong net force, termed the *gradient force*, that acts towards the more intense region of the beam, where the forces will balance and the particle will be stably trapped in the transverse plane. Axial trapping, figure 2.3b, can be achieved through the realisation of a strong axial intensity gradient obtained by tightly focussing the beam with a high numerical aperture (NA) objective lens [85]. If the particle is located above the beam focus, it will refract the light in a more upward direction. By "pushing the light up", the sphere is "pushed down" by the light. If, however, the particle is located below the beam focus, the rays of light are refracted with a more oblique angle, pulling the particle upwards. Consequently, the particle is drawn towards the focus of the objective.

The scattering and gradient forces, however, are often competing against each other: one pushing the particle in the direction of propagation of the beam, while the other draws the particle back towards the focus. Therefore, it is of vital importance that high NA optics are used to generate an axial intensity gradient that is large enough to overcome the scattering force and the pull of gravity [85]. Optical tweezers are often designed in an inverted microscope fashion, exploiting gravity and using it to help balance against the scattering force. However, this is not a necessity, as the gradient force that can be generated with modern high NA objectives is sufficiently large enough

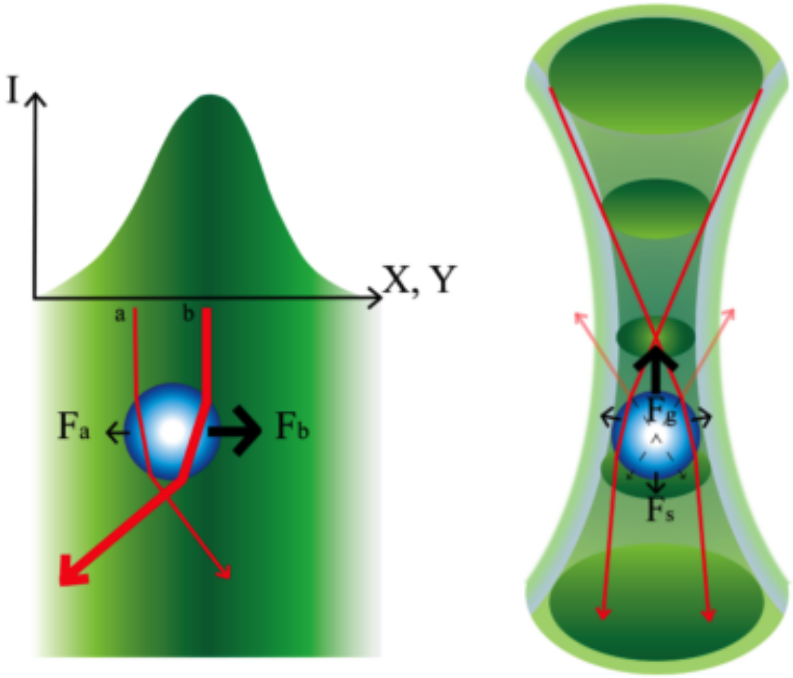

(a) (b)

Figure 2.3: (a) In the transverse plane, conservation of momentum gives rise to a transverse gradient force, which draws the particle towards the most intense portion of the beam. The more intense rays at the centre of the Gaussian beam undergo a bigger momentum change than the weaker, less intense rays. Therefore, a net force is generated that pulls the particle towards the most intense region of the beam (i.e. $F_b > F_a$). (b) An axial gradient force, F_g, is generated by the de/focussing of the light by the particle, drawing the particle towards the geometrical focus of the beam. However, the scattering force, F_s, acts against this axial gradient force, often leading to a trap centre downstream of the geometrical focus of the beam, and so F_g must exceed F_s, and the force of gravity, to form a stable trap. Image adapted from [139].

to allow for the counter intuitive set-up where the beam points downwards and the particle will still trap.

It is possible to perform a more quantitative analysis of axial trapping in the geometrical optics regime through consideration of the Fresnel reflection and transmission coefficients [86]. Here, the scattering force acting on a sphere, trapped with power P, can be described by

$$F_s = \frac{n_m P}{c}\left(1 + R\cos 2\theta + \frac{T^2\left[\cos\left(2\theta - 2\phi\right) + R\cos 2\theta\right]}{1 + R^2 + 2R\cos 2\phi}\right) \tag{2.1}$$

and the gradient force by

$$F_g = \frac{n_m P}{c}\left(R\sin 2\theta + \frac{T^2\left[\sin\left(2\theta - 2\phi\right) + R\sin 2\theta\right]}{1 + R^2 + 2R\sin 2\phi}\right) \tag{2.2}$$

where F_s is the scattering force, F_g is the gradient force, θ is the angle of incidence, ϕ the angle of refraction and R and T are, respectively, the Fresnel reflection and transmission coefficients, as illustrated by figure 2.4. The total force on the particle is given as the sum of these two forces, which is equal to

$$F = Q\frac{n_m P}{c} \tag{2.3}$$

where Q is a dimensionless measure of the trapping efficiency [86].

Equations 2.1 and 2.2 highlight the need for high NA focussing optics, as they describe the dependence of stable axial trapping upon the angles of incidence and refraction. The equations show that, in order to achieve a large resultant force in the axial direction, a large angle of incidence is required, illustrated in figure 2.5 [85]. Additionally, the equations show that the axial trapping force is independent of trapped particle radius. However, an upper limit on trapped particle size is imposed by gravity, and the laser power, as the weight of the particle will scale proportionately to the cube of its radius.

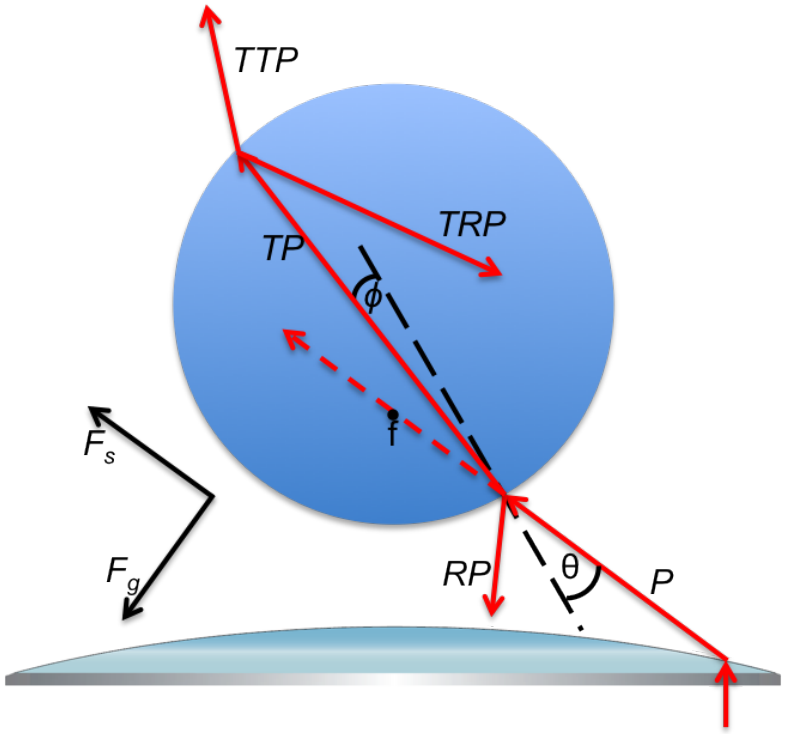

Figure 2.4: Geometrical optics illustration of a single ray when trapping a sphere in a single, Gaussian beam tweezers with an inverted microscope design, with scattering and gradient forces F_s and F_g. The black dashed line denotes a surface normal, f is the focal point, θ is the angle of incidence and ϕ is the angle of refraction. R and T are, respectively, the Fresnel reflection and transmission coefficients, which give rise to reflected and refracted rays of power RP, TP, TRP, TTP, etc. Image adapted from [107].

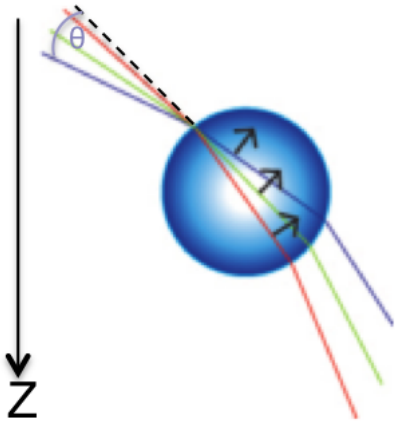

Figure 2.5: Aggressively focussed rays of light, i.e. light with the largest angle of incidence, contribute the greatest vertical component of the resulting axial gradient force (represented by the black arrows). Hence the need for high NA focussing optics, in order to achieve the required tightly focussed trapping beams. Image adapted from [139]

2.1.2 Rayleigh regime

In order for a particle to be considered as falling within the Rayleigh regime, the radius of the particle must be much smaller than the wavelength of the trapping light, $r \ll \lambda$. In this case, only a small portion of the light interacts with the particle, therefore a ray optics description is inappropriate. A more accurate approach to calculating the trapping forces acting on the particle is through the *dipole approximation*: upon illumination, the electric field component of the electromagnetic wave will induce a polarisation in the atoms of the particle, thus generating an electric dipole moment. Therefore, the trapped particle can be considered as a point dipole in an inhomogeneous electromagnetic field. A corollary of this approximation is that the total force acting on the particle can be separated in to the scattering and gradient forces [16].

The scattering force, which is proportional to the dissipative, or imagin-

ary, part of the complex polarisability [140], is due to the absorption and re-radiation of this light by the dipole [17], giving rise to a force which acts in the direction of propagation of the light, counteracting the gradient force. It can be described by

$$F_s = \frac{I_0}{c}\frac{128\pi^5 r^6}{3\lambda^4}\left(\frac{m^2-1}{m^2+2}\right)^2 n_m \tag{2.4}$$

where I_0 is the intensity of the incident light and $m = {}^{n_p}/_{n_m}$, also known as the effective refractive index of the particle [16].

The gradient force, which is proportional to the dispersive part, i.e. the real part, of the complex polarisability [140], can be considered by assuming that the particle and light form a closed system. In order to minimise the energy of the whole system, the polarised particle will be drawn to an area of high intensity, which is the local minimum in potential energy, due to a Lorentz force. The gradient force is given by

$$F_g = -\frac{n_m}{2}\alpha\nabla\mathbf{E}^2 = -\frac{n_m^3 r^3}{2}\left(\frac{m^2-1}{m^2+2}\right)\nabla\mathbf{E}^2 \tag{2.5}$$

where α is the polarisability of the particle and $\mathbf{E}$ is the electric field vector [16]. It follows, therefore, that a strong electric field gradient is required to generate this force, a gradient such as that of a tightly focussed laser, figure 2.6(a). The particle will then be trapped at the focus of the light. For a tightly focussed Gaussian beam, once the scattering force is also considered, the trap centre will actually be slightly behind the laser focus, figure 2.6(c).

However, if the Gaussian trapping beam was to be only weakly focussed, which is the case when working with low NA focussing optics, it is possible for the magnitude of scattering force to be larger than that of the gradient force. For illustrative purposes, this situation can be though of as akin to figure 2.6(b). In this instance, it is still possible to confine particles in two dimensions by balancing the scattering force with another force, such as

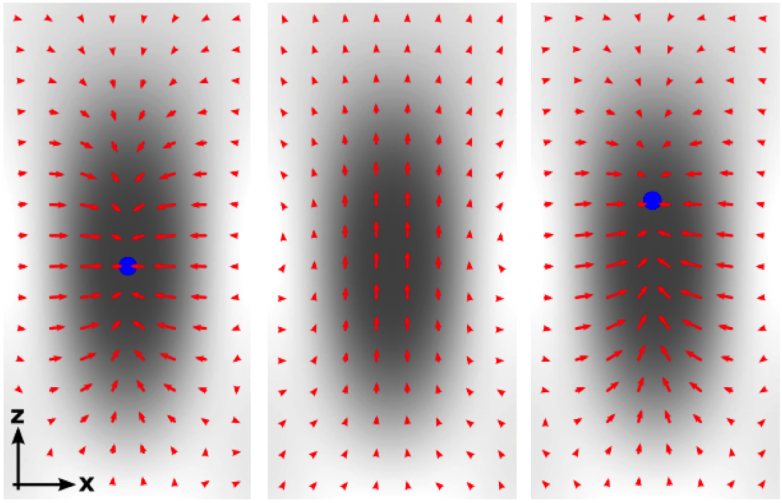

Figure 2.6: An illustration of the forces acting on a point dipole in a laser focus, for a beam propagating in z. The arrows represent (a) the gradient force, (b) the scattering force and (c) the sum of the two forces. The zero point, of the forces, hence the trap centre, are represented by blue circles. Note, the magnitude of the scattering force in (b) has been doubled for clarity. Image adapted from [72].

gravity, producing an optical levitation trap, as outlined in section 1.2.3.

The scattering force decreases much more rapidly than the gradient force, with decreasing particle radius. Therefore, materials that are highly scattering but also highly polarisable, such as gold, can be trapped when much smaller length scales are employed. This is due to the polarisability of gold experiencing a resonance when the dielectric function of gold, which changes as a function of wavelength, becomes negative and twice the value of the dielectric constant of the surrounding medium [49]. Hence the ability of optical tweezers to trap gold nanoparticles [141]. Indeed, there are many interesting implications when the ratio of these two forces is considered. Firstly, the ratio

$$\frac{F_g}{F_s} = \frac{3\sqrt{3}}{64\pi^2} \frac{n_m^2}{\left(\frac{m^2-1}{m^2+2}\right)} \frac{\lambda^5}{r^3\omega_0} \tag{2.6}$$

where ω_0 is the size of the Gaussian beam waist, must be greater than one for stable optical trapping of the particle to occur [16]. A situation, which the ratio suggests, is achievable independently of laser intensity. However, this is untrue as real world considerations, such as Brownian motion [112], are unaccounted for. The ratio also states that longer wavelengths and smaller beam waists will produce more robust traps. While the latter can be achieved through the use of higher and higher NA focussing optics, to produce smaller and smaller trapping volumes, the former proves untrue. The smallest resolvable spot, with diameter d, achievable for light, with a wavelength λ, by a lens with a given NA is described by

$$d = \frac{1.22\lambda}{2N.A.} \tag{2.7}$$

which shows that longer wavelengths cannot be focussed as tightly as shorter wavelengths.

2.1.3 Intermediate regime

When the particle is neither much bigger nor much smaller than the wavelength of the trapping light, $r \simeq \lambda$, neither of the above approximations are valid. While both the geometrical optics and Rayleigh regimes have an intuitive description of the physics governing optical trapping, no such description exists for particles which fall into this intermediate regime. In order to obtain quantitative results, it is necessary to implement complex electromagnetic scattering theory [85, 142, 143]. This is somewhat unfortunate, as there are a significant number of experimental studies that must work in this regime, including much of the work contained within this thesis.

For a homogeneous, spherical particle, one can turn to Mie theory to calculate the scattering of a linearly polarised plane wave. As the illuminating light is focussed through a lens in optical trapping, decomposition of the trapping field into plane waves, using the angular spectrum representation

[49, 144], allows for the calculation of the trapping force.

An extension to Mie scattering, known as generalised Lorenz-Mie theory, attempts to describe the scattering of a transversely localised beam, e.g. a laser, by a small particle and is required for the calculation of forces in optical tweezers [145]. In order to calculate the scattering by a particle, the exact fields of the illuminating beam must be known. However, the exact fields of a beam which satisfies both the wave equation and Maxwell's equations are only known, in closed form, for a plane wave [145]. Therefore, this approach expresses the incident and scattered fields in terms of vector spherical wavefunctions [146].

Calculations using Lorenz-Mie theory are computationally intensive and a number of approaches have been developed, such as finite-difference, time-domain modelling, which calculates the electromagnetic field at each point of a finite mesh [143, 147], or the T-matrix method, which describes the transformation of the light by the trapped particle in terms of a transfer matrix [146, 148].

Recently, there has been an increasing number of open source computer programs that allow for the calculation of forces within this regime. Notably, the Optical Tweezers Computational Toolbox [146] developed by Nieminen *et al.,* which provides both a Lorenz-Mie and a sophisticated T-matrix approach to the calculation of forces in a wide variety of optical trapping situations. Although it has been shown that the exact calculation of the trapping force within the intermediate regime can often require a subtle approach [149], for many situations a ray optics approach will provide adequate results, and computational toolboxes for these situations are also available [150].

2.2 Experimental systems

In order to generate the forces outlined above, regardless of what force regime trapping will occur in, an optical trapping system must first be con-

structed. Advanced optical engineering skills and an in-depth knowledge of optical physics is not required to set up a system and begin taking fairly sophisticated results. In fact, optical tweezers are relatively straightforward to design and build, a simplicity that has contributed to their wide adoption as a powerful tool. State-of-the-art systems could be equipped with more stable trapping sources and optomechanical equipment, or have higher precision nano-positioning stages. However, low-cost systems capable of molecular motor measurements have been assembled for under $15,000 [151], excluding the optical table, while demonstration systems for undergraduate laboratories have been built for only $6,500 [152]. Increasingly, control and analysis software for these systems is being made freely available online [153–157], therefore, after a modest investment into a system, a non-expert user could quickly set up a sophisticated system, one capable of research grade measurements. Indeed, chapter 6, shows that this initial investment could, in some cases, be on the order of pennies.

2.2.1 Design considerations

When constructing a set of optical tweezers, there are a number of different factors that must first be considered. Prime among them is the nature of the experiment, as this will dictate the complexity, or indeed the simplicity, of the system, possibly requiring the acquisition of specialised, application specific, optics. Are there wavelength constraints imposed by the sample under study? Must there be control of trap position and, if so, how precise should this control be? Will force measuring techniques be employed and, if so, how stable must the system be in order to avoid unwanted noise in the measurements? Each of these questions must be answered and will be determined by the nature of the experiment. Indeed, several optical tweezers systems were constructed for the work presented in this thesis, each with a specific experiment in mind, and are discussed at the beginning of the relevant experimental section. However, regardless of the complexity of the

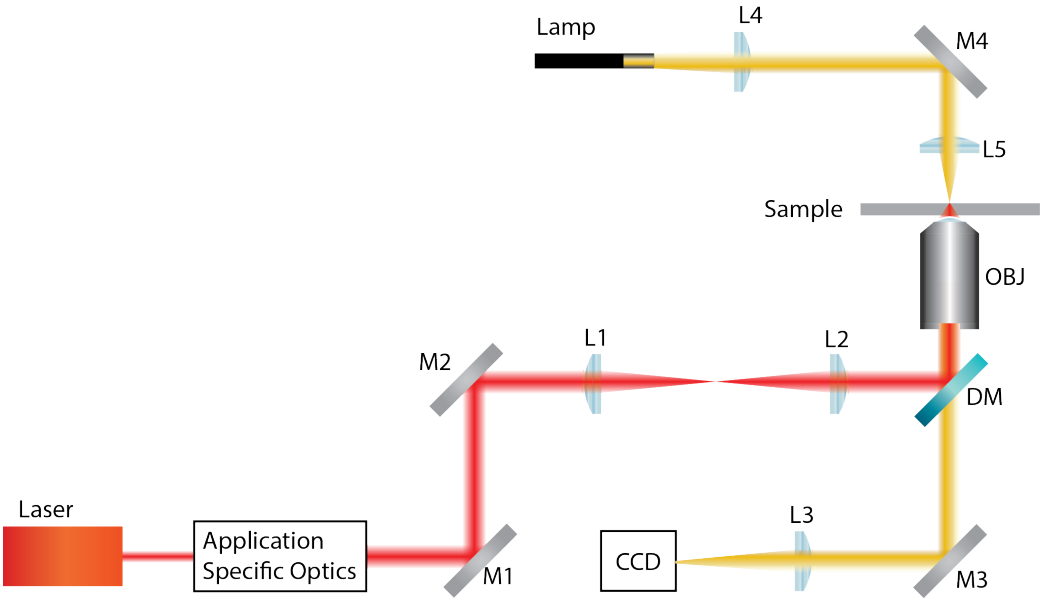

Figure 2.7: A basic optical tweezers system. After passing through any application specific optics, the laser is steered by mirrors M1 and M2, which act as the steering mirrors, through the beam steering lens relay system, formed by lenses L1 and L2, and is reflected into the microscope objective (OBJ) by the dichroic mirror (DM), which forms an optical trap in the sample. Lenses L3, L4 and L5 combine with the microscope objective and mirrors M3 and M4 to form the illumination, and therefore imaging, path. This will image the sample on to the CCD camera.

system, the core of it will, more often than not, be designed around a basic optical tweezers system, shown in figure 2.7, the construction and primary design considerations of which are discussed here.

A basic optical trapping system consists of eight main components: a trapping laser, a high NA microscope objective, an illumination source, a camera, a dichroic mirror, steering mirrors, a beam steering lens relay system and a sample of interest. The exact specifications of each of these components can vary greatly with application, and even with available lab space and budget, and many review articles have been written on the constrains imposed by different applications [17,69,71,72,74,107,156,158–160]. It is im-

portant, however, to understand the overall need for each of these eight components and how, through the correct combination, a stable optical tweezers can be assembled.

Trapping source

A good trapping laser will produce a collimated, monochromatic, coherent Gaussian beam, which allows the light to be focussed to a diffraction limited spot by the microscope objective. The output power of the laser is possibly the most obvious parameter to consider when selecting a trapping laser because the maximum trap stiffness and, therefore, force that can be attained will be determined by the laser power and the throughput of the optical system. In general, it's often advantageous to have a higher power laser than required: it's easier to attenuate the power in the system than it is to build a highly efficient system if trapping power is of concern. The beam quality factor, or M^2 factor, of a laser, together with the optical power, also plays a role in determining the radiance of the beam. The M^2 factor is, essentially, a measure of the deviation of the laser from a perfect, diffraction limited, Gaussian beam, which has an M^2 factor of 1 and focusses to a diffraction limited spot. The M^2 factor limits the minimum spot size that can be achieved by a focussing lens with a given numerical aperture [161]. The diffraction limited spot required for efficient optical trapping cannot, therefore, be achieved from a laser with a large M^2 factor without additional optics prior to the microscope objective.

Laser wavelength must also be considered as this will influence everything from the cost of the system, to the selection of optical components, to heating of the sample. Shorter wavelengths are best avoided if biological samples are to be investigated by the tweezers because they can prove harmful to the sample, especially when trapping cells directly. Longer, biosafe wavelengths, however, tend to have a higher extinction coefficient of water, thus leading to greater heating effects felt by the sample [72]. Possibly a less obvious con-

sideration, but a vital one nonetheless, is the stability of the laser. Pointing instabilities can lead to unwanted displacements of the optical trap in the trapping plane, while power fluctuations can lead to temporal variations in the trap stiffness [17].

High NA microscope objective

As previously outlined in section 2.1, a high NA microscope objective (NA > 1) is the most important element of an optical tweezers system as it is this that forms the trap. The transmission and NA of the objective will determine the efficiency with which input power is converted to trapping performance. A diffraction limited focal spot can be produced by expanding the trapping laser to slightly overfill the back aperture of the microscope objective, ensuring the full utilisation of the objective's NA, thus generating a high quality, three-dimensional optical trap. The maximum trapping depth within the sample will also be set by objective choice, as it will be set by the immersion medium and working distance of the objective. Spherical aberrations impede trapping performance and can arise due to the refractive index mismatch between the objective immersion medium and the trapping medium, with the magnitude of these detrimental effects increasing with focal depth [17]. Trapping at depths of over 20 μm can be improved through the use of water immersion objectives, as opposed to the more traditional oil immersion objectives, as they exhibit much lower spherical aberration [162]. Additionally, selection of a high quality microscope objective can help to limit spherical aberration as they are designed to correct this effect in a number of ways, e.g. multiple lens elements (i.e. lens doublets or triplets) or special lens-grinding techniques [138]. Owing to the variation of spherical aberration with wavelength, it is imperative to chose a microscope objective that has been corrected for, or as close to, the wavelength of the trapping laser [163]. Often, achromatic microscope objectives will only be corrected spherically for one or two wavelengths, while the highest quality planapochromatic objectives

are corrected for up to four wavelengths [164].

Dichroic mirror and illumination

The microscope objective, when combined with an illumination source and camera, also serves to image the sample in exactly the same manner as when used in a commercial microscope. However, this presents an issue as the imaging path and the laser path are merged as they travel through the objective and, therefore, must be separated afterwards. In order to achieve this, a dichroic mirror is placed before the microscope objective so that only the laser wavelength is reflected and the remaining illumination light is transmitted to the camera. The illumination source, and the way in which the sample is illuminated, is very important but also very flexible. Standard, white-light illumination is suitable for the majority of applications but other techniques, such as fluorescence imaging or stimulated emission depletion microscopy, can be combined with the tweezers to give a very powerful investigative tool. Unless otherwise stated, the optical trapping experiments presented in this thesis use Köhler illumination [165], illustrated in figure 2.8.

Köhler illumination is among the more popular illumination arrangements for white-light illumination due to its ease of construction and many advantages [166]. The lamp structure is imaged onto the condenser diaphragm via a 4f imaging system, while a second 4f system images the field diaphragm into the sample plane. This produces an even illumination of the sample, while also decoupling the image of the light source from the illumination, which allows for high sample contrast. By varying the field diaphragm, in order to only illuminate the region of interest, glare can be reduced, thus increasing image contrast. However, the condenser diaphragm, when adjusted, can alter both the contrast and resolution of the image. The correct balance between contrast and resolution must, therefore, be found in order to optimise the image quality.

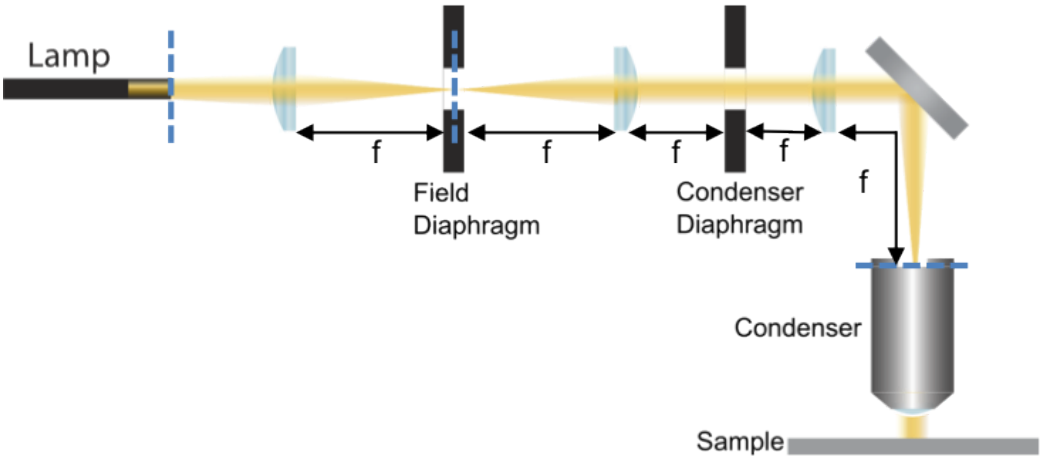

Figure 2.8: Köhler Illumination uses two 4f systems to decouple the illumination and imaging planes. The planes conjugate with the filament of the lamp are shown as blue dotted lines, with the ray paths shown in yellow. Note that an image of the lamp filament is not formed in the sample plane and that uniform illumination is produced instead. The field diaphragm can be used to control image contrast, while image contrast and resolution can be varied by adjusting the condenser diaphragm. Finding the correct balance between the two diaphragms can greatly improve image quality. Image adapted from [137, 139]

Beam steering lens relay system

In essence, that is all that is required to create an optical tweezing system. However, in terms of manoeuvrability, it still leaves a lot to be desired. The trap will remain stationary, with movement through the sample achieved by physically moving the sample. This is not always practical and it would be clearly advantageous to have some form of control over the optical trap position. Through the inclusion of steering mirrors, two dimensional control of a trapped object can be gained as they allow for the trap to be moved laterally in the focal plane of the objective. However, if the steering mirrors are placed directly behind the microscope objective, ray optics clearly shows that any tilt in the mirrors will cause the beam to shift from the back aperture of the objective. An asymmetric trap will then be formed, as any shift from the objective's centre will deform the focus, producing an asymmetric focal spot. It is possible to circumvent this problem by placing a 4f imaging system between the steering mirrors and the microscope objective, as illustrated by figure 2.9. Such a system is called 4f due to there being four focal lengths between the start and end of the system: one focal length from the mirror to the first lens, two focal lengths between the lenses, then one focal length to the back aperture of the microscope objective. The steering mirror and the back aperture of the microscope objective become conjugate planes through the inclusion of this beam steering lens relay system. A conjugate plane is defined as a plane where the intensity distribution is an image of the intensity distribution across a corresponding plane [144]. As the steering mirror and microscope objective back aperture are now conjugate, any angular displacement at the mirror has a corresponding angular displacement at the back aperture, with no lateral movement of the beam. This angular displacement is then translated by the objective, to the objective focus, as a lateral movement in the focal spot. Therefore, the optical trap can be steered in two dimensions without any degradation in trap performance.

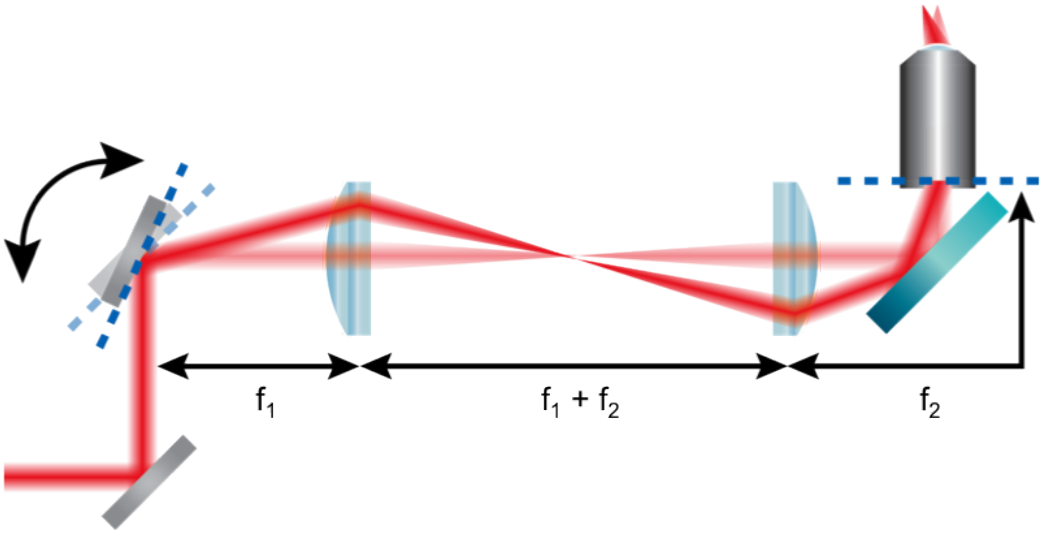

Figure 2.9: Beam steering lens relay system formed through the use of a 4f optical system, with the dotted lines denoting conjugate planes. Note that an angular deviation in the mirror causes an angular displacement at the back aperture of the microscope objective, which translates to a lateral movement of the beam focus, without misalignment. The original mirror and beam positions are included for reference but are less opaque for clarity.

Optomechanics

It should be noted, however, that while each of these components are of great importance in an optical tweezer system, even the highest quality optics will be of little use if not properly mounted. Due to the high magnification that optical tweezers operate with, precise measurements are at the mercy of drift and vibration. The majority of optical tweezers are custom designed breadboard-based systems or are integrated into commercial microscope systems, although there has been some work assessing the suitability of constructing optomechanics from LEGO [167]. Commercial microscope systems provide many advantages, such as high stability, especially of the microscope objective and sample, and familiarity of design. However, they are often not designed to be adaptable and easily converted to an optical trapping system. The increased stability offered could, in practise, be nullified due to convoluted designs which may be required in order to integrate the laser. Custom built systems offer flexibility, which can lead to a much simpler optical design and ease of alignment. However, care must be taken during construction to avoid mechanical resonances.

2.3 Force measuring techniques

It is easy to see how optical tweezers could have become relegated to a curiosity, allowing the user to pick up, move and look at different micron-scale objects, had it not been for their impressive ability to be used as a quantitative tool. In fact, due to their ability to exert and measure piconewton forces, optical tweezers have become an indispensable, quantitative tool in many labs.

At the heart of quantitative optical trapping is accurate position detection, as the majority of force measurements are made by indirectly measuring the position of the trapped object. Assuming that the position of the trapped object is not displaced from the trap centre by more than a few hundred nano-

metres, the potential energy of the sample follows a simple parabolic equation and the trap behaves harmonically. Therefore, the restoring force that pulls the particle back to the trap centre is linear with respect to displacement. As the particle is acting in a similar manner to an object on a spring, the restoring force, F, can be described by an optical equivalent to Hooke's law

$$F = -kx \tag{2.8}$$

where k is the trap stiffness, which is analogous to the spring constant and is essentially a measure of how well the particle is trapped, and x is the position of the trapped object relative to the trap centre, figure 2.10. Consequently, measuring the force acting on a trapped object is often split into two distinct steps: measuring the displacement of the trapped particle from the trap centre, i.e. determining x, and calibration of the optical trap in order to ascertain the trap stiffness, k.

Due to the importance of accurately measuring these two components, a smorgasbord of different techniques have been developed, improved and refined over the years. The two most prominent techniques are video based particle tracking and interferometric particle tracking.

2.3.1 Displacement measurement - QPD vs camera

Video based tracking

Measuring the displacement of the particle using video based methods is not only relatively straightforward but also very convenient as most optical trapping systems are already equipped with a camera to observe the sample. By calibrating the video picture against a known distance, such as a microscope graticule, the magnification of the imaging system can be determined and, therefore, particle tracking measurements can be given in absolute distance units. This calibration is independent of sample depth and remains linear over the field of view, typically tens of microns. Sub-pixel resolution is

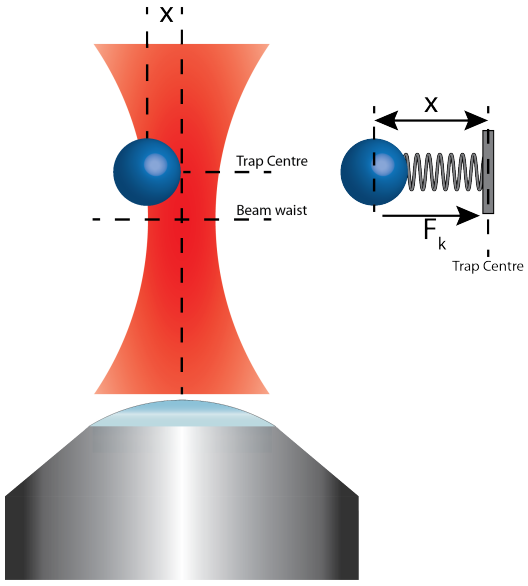

Figure 2.10: Enlarged view of a displaced bead in an optical trap. The laser is travelling up the page, with the trap location formed just downstream of the beam waist. The bead, displaced a distance x from the trap centre, will feel a restoring force, which increases linearly with respect to displacement, towards the trap centre. The bead, therefore, can be considered as a mass on a spring, with spring constant k.

achievable through tracking algorithms such as centre of mass tracking and there is a wide variety of programs, both commercial and open-source, which allow for this. This achievable resolution can correspond to displacement measurements of only a few nanometres, due to the high magnification used in optical tweezers, and, most importantly, can be extended to track multiple particles at the same time [72, 116].

However, video based techniques are not without their drawbacks. Although two dimensional particle tracking can be somewhat trivial, extending the technique into the third dimension can prove challenging. A variety of post-processing software packages have been developed in order to provide an estimation of the z-position of the trapped particle, with approaches ranging from the approximate to the empirical. Through monitoring the brightness of the centre of the trapped particle, an approximation of the z-position can be given [154], while a more pragmatic approach would be to compare the image of the trapped particle with previously taken images of the particle at known depths [168]. Three dimensional particle tracking can be improved through changes to the microscope imaging system in order to provide for stereoscopic imaging. Here, two images of the particle are produced and, through 2D tracking of each image, 3D positions can be determined. Particles have been tracked with nanometre accuracy, over an axial range of 10 μm, through the use of such systems [169].

High frame rate cameras are also required for video based particle tracking, with higher frame rates giving higher temporal resolution. Burst frame rates of tens of kilohertz are achievable but are limited by computer memory, leading to small sample times and presenting the additional issue of data management. The main limitation of video based techniques, however, is that it is restricted by the number of photons which can be recorded by the camera. High frame rates mean shorter exposure times, consequently requiring a higher level of illumination. Thus, an increase in frame rate is coupled to a loss in spatial resolution [17]. Furthermore, video based techniques are

less than ideal for measuring the position of the trapped object relative to the trap centre, which complicates force measurements.

Interferometric tracking

Interferometric particle tracking techniques, notably back-focal-plane interferometry (BFPI), tend to be more popular than their video based counterparts for particle tracking, due to their high temporal (kilohertz) and spatial (less than one nanometre) resolution and their ease of implementation [71]. In order to employ this technique, a position sensitive photodiode, typically a quadrant photodiode (QPD), is placed in a conjugate plane to the back aperture of the microscope's condenser lens. Having passed through the sample and been collected by the condenser lens, the light is imaged onto the QPD, which produces light intensity dependent voltage signals. The QPD is, essentially, four separate photodiodes, which share a common cathode, that each produce a voltage which is dependent on the intensity of their illumination. Through the correct combination of the four voltages produced, it is possible to calculate an x, y and z position of the trapped object [170]. Using the quadrant numbering system outlined in figure 2.11 and denoting their output voltages as V_1, V_2, V_3, and V_4, the x, y and z voltages are given as

$$V_x = \left[(V_1 + V_3) - (V_2 + V_4)\right] / V_z \tag{2.9}$$

$$V_y = \left[(V_1 + V_2) - (V_3 + V_4)\right] / V_z \tag{2.10}$$

$$V_z = V_1 + V_2 + V_3 + V_4 \tag{2.11}$$

By monitoring the change in the voltage signal, the change in the collected light can be measured and, therefore, the change in the particle position can be inferred.

The sensitivity, particularly in the axial direction, can be attributed to the fact that the light collected by the detector does not have a simple Gaussian

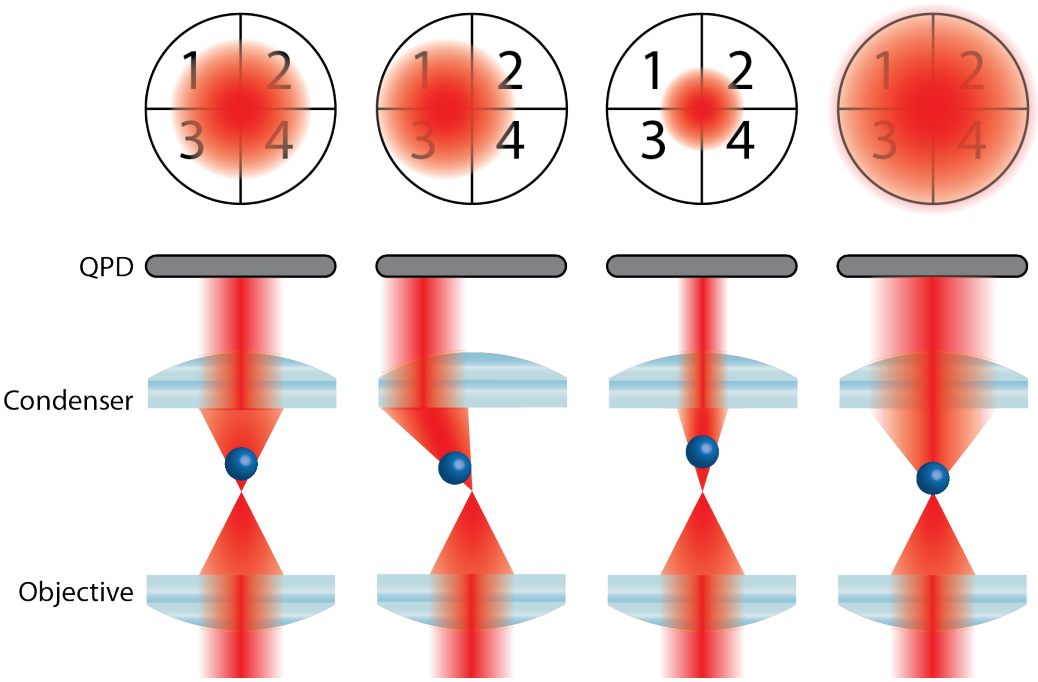

Figure 2.11: QPD placed in the back focal plane of the microscope condenser. Position information can be found by looking at the interplay of the voltages from the four quadrants. With a particle trapped in the optical tweezers, the QPD will, from left to right: see equal illumination on all four quadrants for a particle sitting in the centre of the trap; collect more light on one side of the detector than the other if the particle is displaced laterally from the trap; give an increased signal if the particle height increases above the trap centre, due to focussing of the light; reduce its voltage output if the particle decreases in height above the trap centre, due to an increase in the divergence of the light.

distribution. The detector actually sees an interference pattern, produced from light that travels through the sample and is scattered by the trapped object and light that remains unscattered. A Fourier transform of the field in the sample plane is formed at the back-focal-plane of the condenser, which offers some advantages in position detection. Notably, a phase shift in the field at the back-focal-plane is produced if there is a change in the object's position within the trap. Although this gives no information about the position of the trap within the sample, it does provide information regarding the relative displacement of the trapped object from the laser beam, which is precisely the information required for force measurements [71].

Although being straightforward to implement, BFPI systems present their own challenges: highly sensitive displacement measurements necessitate accurate alignment of the detector and careful calibration is essential to find the relationship between detector voltage and particle displacement. Calibration curves are often calculated by, first, fixing a latex or silica bead to a glass microscope slide. A piezoelectric stage is used to scan the bead back and forth, in a triangular wave fashion, through the trap centre, in order to produce a similar voltage calibration curve to that shown in figure 2.12. An approximately linear region lies between the maximum and minimum voltage values. By calculating the slope of this region, in volts/second, and combining with the known stage velocity, a calibration constant, β, can be calculated in volts/nm [171]. Calculation of the calibration curve is non-trivial and care must be taken to ensure that, while calibrating one axis, the signals from the other axes are minimised. The location of where the immobilised bead passes through the beam will alter the calibration constant. Scanning the bead slightly higher or lower than the trap centre will result in a different calibration constant and, therefore, incorrect positional information. Furthermore, detector response is a function of bead size, so the calibration procedure must be repeated and β calculated separately for objects of a different size.

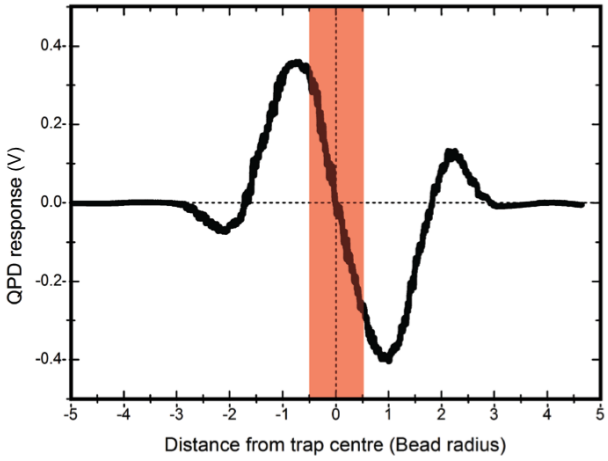

Figure 2.12: Typical shape for a QPD calibration curve showing QPD response, in arbitrary units, as a function of particle distance from the trap centre, in bead radii. From the slope of the linear region, shaded red, the calibration constant can be calculated.

A convenient, albeit indirect, method for detector calibration has been proposed by Allersma *et al.* [171]. Through studying the position fluctuations of an optically trapped particle, they developed a technique that calculates β for the detector to within 20% of the true value and avoids the issue of scanning a fixed bead through the trap centre. This method allows for a quick check of the system and can serve as a calibration method for when, either, precision is of no concern or labs cannot get access to the expensive piezoelectric stages required for the active calibration method.

2.3.2 Trap stiffness measurement

In order to measure a force with optical tweezers, the trap stiffness, k, must first be measured. Several methods have been developed to allow this, each with their relative advantages and disadvantages, but all follow the same,

basic, underlying principle: apply known forces to an object and determine their effect. Through knowing both the applied force and the resultant displacement, trap stiffness can be calculated. Although there are many approaches they can, in general, be classified into two main groups as defined by the origin of the applied, external force: hydrodynamic or thermal [71].

Hydrodynamic techniques

Hydrodynamic methods, such as the Stokes' Drag Force method, measure the displacement of the particle from the trap centre as a function of applied drag force. The drag force on a sphere of radius r is given as

$$F_{Stokes} = -6\pi\eta r v \tag{2.12}$$

when moving at a relative velocity v, through a liquid with dynamic viscosity η, and can be achieved through either movement of a motorised stage or flowing liquid through a microfluidic device. Care must be taken, however, if the latter technique is used as it is necessary to compensate for the parabolic flow profile of the liquid through the channel, as flow velocity will be strongly dependent on channel depth. Trap stiffness can be determined by measuring particle displacement from trap centre and combining equations 2.8 and 2.12. Albeit the most direct method of measuring the trap stiffness, the drag force technique is not as reliable as those that are based on analysis of the thermal motion of the particle.

Thermal techniques

Measuring the trap stiffness with thermal based techniques rely on the study of the Brownian motion of the trapped particle and, therefore, do not require the application of an external force *per se*. A number of methods exist for the analysis of thermal motion, each with their own relative advantages and disadvantages. For example, the equipartition method [172], will give

a fast estimation of the trap stiffness, whereas the power spectrum analysis method [170], will give the most accurate and reliable trap stiffness measurement [71]. An overview of some of the prevailing methods is provided below. Common to all techniques, however, is the requirement of a detector with a sufficiently high bandwidth in order to record the Brownian motion of the trapped particle. Although possible with video based particle tracking, the previously mentioned BFPI (section 2.3.1) excels for this technique. Bandwidths of up to 1 MHz [173] have been reported for QPD based systems, making them ideally suited for the detailed study of Brownian dynamics.

Equipartition method - For a particle bound in a harmonic potential, such as a bead trapped by an optical tweezers, the equipartition theorem of energy is given as,

$$\frac{1}{2}k_BT = \frac{1}{2}k\left\langle x^2\right\rangle \tag{2.13}$$

where k_B is Boltzmann's constant, T is the temperature and $\langle x^2\rangle$ is the mean square displacement from the trap centre. Using a suitable position measuring technique to measure the particle position fluctuations, it is possible to determine the trap stiffness with no prior knowledge of the medium viscosity. However, it is necessary to accurately calibrate the detection system in order to provide accurate positions. Additionally, this approach is highly susceptible to noise, which will increase the average squared displacement.

Mean squared displacement analysis - Analysis of the mean squared displacement (MSD) of an optically trapped particle, which quantifies how the particle moves from its initial position, allows for a more precise characterisation of the optical trap than the equipartition method offers. For an optically trapped particle, trapped with a stiffness k, in a trap whose restoring force acts on a time scale of $\tau_{ot} = \gamma/k$, where $\gamma = 3\pi\eta d$, the theoretical MSD is

$$\text{MSD} = 2\frac{k_BT}{k}\left(1 - \exp\left(-\frac{|\tau|}{\tau_{ot}}\right)\right) \tag{2.14}$$

and, when plotted, can be separated into two distinct regions [49]. At short time scales ($\tau \ll \tau_{ot}$), the plot increases linearly, corresponding to free diffusion. However. at longer times scales ($\tau \gg \tau_{ot}$), the plot reaches a plateau due to the confinement of the particle within the trap [49].

Through acquisition of the particle positions as a function of time, one can calculate the particle's experimental MSD using

$$\mathrm{MSD} = \frac{1}{N}\sum_{n=1}^{N}\left(x_n\left(t\right) - x_n\left(0\right)\right)^2 \tag{2.15}$$

where N is the number of samples of the particle, $x_n\left(0\right) = x_0$ is the reference position of the particle (e.g. the trap centre), and $x_n\left(t\right)$is the particle's position at time t. Through fitting equation 2.15 to equation 2.14, one can determine the trap stiffness [49].

Autocorrelation analysis - Calculation of the position autocorrelation function of a trapped bead allows for an accurate determination of trap stiffness. As the typical relaxation time, τ_{ot}, for a bead to reach its equilibrium position in an optical trap is on the order of milliseconds, the position autocorrelation function can be written as [49, 174]

$$\left\langle x\left(0\right)x\left(t\right)\right\rangle = \frac{k_B T}{k}\exp\left(-\frac{t}{\tau_{ot}}\right). \tag{2.16}$$

The trap stiffness can then be determined by fitting the experimental autocorrelation function for the data, which is calculated as

$$\left\langle x\left(0\right)x\left(t\right)\right\rangle = \frac{1}{N}\sum_{n}^{N} x_n\left(t\right)x_n\left(0\right) \tag{2.17}$$

to equation 2.16 [49, 174].

Power spectrum analysis - The power spectrum method involves recording the relative displacement of the particle from the trap centre as a function of time, and is generally regarded as the most reliable method, hence its use in the following chapters. This data will have a Gaussian probability distribution in the time-domain, which is characteristic of the Brownian motion of a particle in a harmonic potential [170]. However, by computing the single-sided power spectrum of the position fluctuations, the characteristic shape of a Lorentzian function is obtained [71, 171], as shown in figure 2.13, and can be described by equation 2.18. For a particle with diameter d, the power spectrum, in units of distance^2/frequency is

$$S(f) = \frac{S_0 f_c^2}{f_c^2 + f^2} \tag{2.18}$$

where f is the frequency, $S_0 = 4\gamma k_B T/k^2$ is the zero-frequency intercept of $S(f)$, the corner frequency of the power spectrum is $f_c = k/2\pi\gamma$ and $\gamma = 3\pi\eta d$ is the Stokes' drag coefficient of the bead [171]. If the detector has been calibrated, power spectrum units are given as nm^2/Hz, while an uncalibrated power spectrum, often the case when BFPI is employed, has units of V^2/Hz.

Through fitting the Lorentzian function to the data, the corner frequency of the spectrum can be obtained and, therefore, the trap stiffness can be calculated. Furthermore, this can be obtained independent of detector calibration. If a calibration procedure has been carried out, then information about the viscous damping can be extracted and, given a known particle radius, the viscosity of the surrounding medium can be calculated. The corner frequency also serves to divide the Brownian motion into two distinct regimes. When $f \ll f_c$, the power spectrum exhibits a constant plateau, S_0, which reflects the confinement of the trapped particle. For $f \gg f_c$, the power spectrum falls off as $D/\pi^2 f^2$, where D is Einstein's diffusion coefficient. This is characteristic of free diffusion and can be attributed to the particle behaving

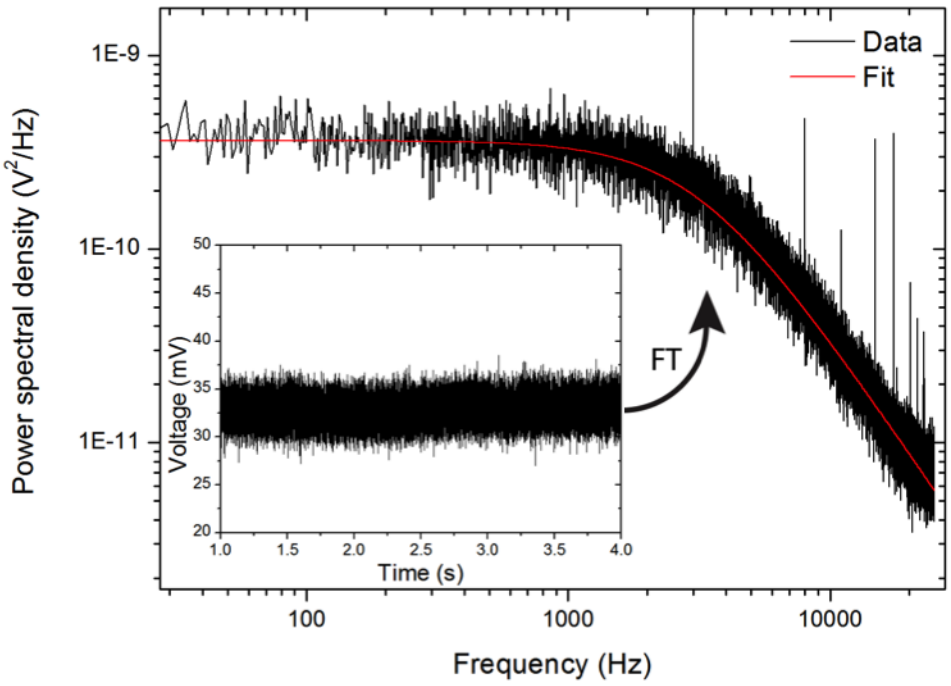

Figure 2.13: Power spectrum of a 1 μm silica bead trapped in water, obtained from the time dependent position fluctuations shown in the inset. Power spectrum taken from an uncalibrated QPD, hence units are in V^2/Hz rather than nm^2/Hz. Data, shown in black, shows that there is some high frequency noise present in the system. The fitted Lorentzian function, red line, gives a corner frequency of $\approx$ 3200Hz, which corresponds to a trap stiffness of $\approx$ 200pN/μm.

as if the trap does not exist at short observation times [71].

In order to achieve the high accuracy offered by the power spectrum method in determination of trap stiffness, a wide variety of different effects must be considered and accounted for. Hydrodynamic interactions between the particle and the microscope coverslip result in a trapping depth dependency of the force experienced by the particle, therefore Faxén's correction must be applied or an artificially inflated trap stiffness may be measured [162, 170]. The position detection system can also act as a low-pass filter and can, therefore, lead to an underestimate of the corner frequency of the power spectrum, thus giving a lower than expected trap stiffness. This filtering effect could be caused by inappropriate choice of detector material leading to parasitic filtering [71], for example, silicon is transparent to infrared light, therefore a detector constructed from indium gallium arsenide (InGaAs) would be preferential [170]. Fortunately, Berg-Sørensen and Flyvbjerg have carried out a comprehensive study of the data acquisition and accurate fitting of the Lorentzian function involved in power spectrum analysis of optical tweezers [170]. In this paper, they thoroughly analyse, far beyond the scope of this introduction, the theory which governs power spectral analysis, design constraints and undesirable effects that can arise. Additionally, the authors also developed an open source MATLAB program, which can perform much of the data analysis required for power spectrum analysis [175–177].

2.4 Beam shaping

As powerful and as useful as optical tweezers are, it is not difficult to imagine that the limits of what can be achieved with a single, Gaussian intensity, trap can be quickly reached. For example, section 2.1 discussed scenarios where the refractive index of the particle is higher than that of the surrounding medium. However, what if the reverse is true, such as in the case of a

bubble of gas in water, and, therefore, the particle is repelled by the optical trap [88,178]? If multiple particles need to be trapped simultaneously, would multiple trapping sources be required? The beam steering lens relay system allows the user to move a particle in 2D by tilting a mirror but does not allow for 3D movement nor accurate, reproducible, finite control of the particle by the user.

To circumvent these issues, the optical manipulation community has increasing turned to a variety of beam shaping techniques. Although shaping of other micromanipulation techniques, such as acoustic waves [93], is possible, the facile nature of optical beam shaping, and the versatility that can be gained through it, makes optical beam shaping a very powerful technique. Often defined by the method in which the technique shapes the beam, whether it alters the amplitude or phase of the light, or both in the case of complex modulation, the approach to beam shaping can focus on either static or dynamic processes.

2.4.1 Static beam shaping

In its simplest form, beam shaping could be considered as the splitting of a single beam into two by a beamsplitter, thus allowing for two particles to be trapped and the interaction between them probed in a controlled manner. Generated by the use of an axicon, a single Bessel beam (which is a non-diffracting, self-healing beam) can be used to trap multiple particles in spatially separated planes, at separations of a few millimetres [179]. Diffractive Optical Elements (DOEs) and spiral phase plates have been employed to generate multiple Laguerre-Gaussian (LG) beams, allowing for low index particles to be trapped in the hollow core of the beams or for orbital rotation of particles [180, 181].

Common to each of these techniques is the fact that the shape of the beam is not altered over time and, therefore, they are considered to be static beam shaping techniques. Although more complex examples were given,

the vast majority of optical elements, such as lenses and gratings, can be considered static beam shaping elements. Whether it be through retarding the phase of the wavefront or splitting a single wavefront into many, the way in which each technique shapes the beam will be unique to the element involved. However, as long as the shape of the beam changes through the interaction with the element, and does not continue to evolve over time, the element can be considered a static method of beam shaping.

Static methods are often the best choice for beam shaping, as, for a low cost, they offer simplicity and high optical efficiency. However, they are generally application specific and, although they add to the versatility of optical tweezers, they themselves are not very versatile.

2.4.2 Dynamic beam shaping

To be considered a dynamic method of beam shaping, the element in question must be able to change the shape of the beam, continuously, over time. Although these methods tend to be more expensive and more difficult to set up than their static counterparts, the advantages offered through these techniques vastly outweigh their drawbacks. The user is able to quickly test ideas and designs, changing, for example, from LG to Bessel beams or from 2 to 20 traps almost on a whim.

Albeit a loose definition of beam shaping, devices such as acousto-optical deflectors (AODs) [131, 182] or fast scanning mirrors [183] can be considered dynamic beam shaping techniques. Here, the beam is very quickly moved, in highly controllable fashion, and can shared between positions in the sample plane to create multiple traps. Provided the scanning of the beam is quick enough, particle diffusion can be ignored and the single beam can be considered as creating multiple optical traps, each one individually controllable in two dimensions.

Spatial light modulators

In order to achieve full 3D control over the beam shape it is usually beneficial to employ holographic beam shaping. Typically, a computer generated hologram is displayed on a spatial light modulator (SLM) and can interactively control the imposed phase of a beam. Incident beams can be converted into, among others, LG [184], Bessel [91] or Airy beams [185]; split into multiple diffractive orders to generate multiple trapping sites, each individually controllable; and have their phase profile changed in the axial direction so that they are brought to a focus without a physical optical element.

An SLM consists of an array of pixels, with each pixel consisting of a thin layer of liquid crystals sandwiched between a transparent reflective electrode, figure 2.14. Although the liquid crystals do not exhibit positional order, they do exhibit orientational order and will, over time, tend to align themselves along a specific vector. Upon application of a voltage to a pixel, the liquid crystals will rotate in order to minimise their electric energy. As the nematic crystals are birefringent, this rotation causes a change in the extraordinary refractive index of the pixel. However, the liquid crystals will also feel a restoring force due to the elasticity of the liquid crystal and so they will also try to minimise their elastic energy density. Therefore, the liquid crystals will only rotate until their electric and elastic energy densities reach equilibrium. Thus, tuneable, full phase modulation between 0 to 2π can be achieved in the region of each pixel. Light, whose polarisation is aligned with the extraordinary refractive index of the liquid crystal, will, therefore, experience a different phase delay depending upon the applied voltage to the pixel.

Shaping of the beam can be achieved in one of two ways. If the desired beam shape has a well known shape and an exact solution then the simple application of the phase function to the SLM will achieve the desired pattern. For example, in the case of optical tweezers, a single Gaussian spot can be easily controlled in all three dimensions by applying the phase function for a grating and lens to the SLM [186]. However, if more complex beam

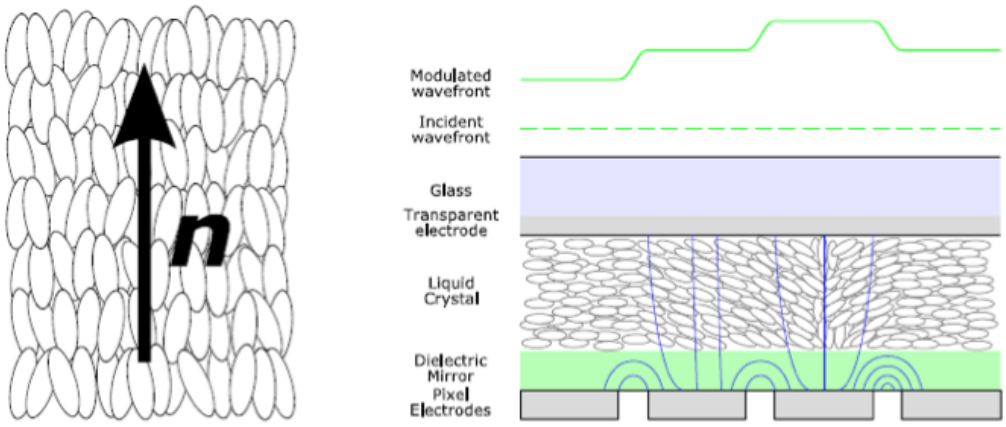

Figure 2.14: (left) liquid crystal molecules showing orientational, but not positional, order. (right) schematic of an SLM showing its effect on an incident wavefront . Figure from [137]

shapes are required then more complex solutions are required and it is often necessary to more to iterative algorithms, such as the Gerchberg-Saxton algorithms [187]. Although these algorithms are much more computationally intensive and often must be pre-calculated, they are generally more optically efficient and capable of generating hundreds of high-quality optical traps, each individually controllable and shapable [130]. With the advent of GPU driven graphics acceleration, such algorithms are becoming more practical as hologram generation can be achieved over 300 times faster than when calculated on a quad-core CPU [155].

If, however, speed is of concern, such as in the case of dynamically controlling trapped neutral atoms [188], liquid crystal based SLMs may prove to be too slow. Switching to a digital mirror device (DMD) may be necessary if high refresh rates are required, with DMD refresh rates of up to 50 kHz obtainable, significantly faster than the 100s of Hz that the best liquid crystal based devices offer [188]. A DMD consists of an array of individually addressable mirrors that can be switched between two tilt angles [144]. The device, therefore, reflects light into the desired optical path when the

mirror is "switched on", or dumps the power into a beam dump when the mirror is in the "off" position, thus allowing for the generation of arbitrary intensity distributions. This amplitude modulation, however, can lead to poor optical throughput of the system, as a portion of the light incident on the DMD will be dumped out of the system, with loses of up to half of the incident beam power having been reported [189, 190]. Simply increasing the power of the incident beam may not circumvent this problem as it can cause damage to the mirrors of the DMD [189]. This does not present an issue, however, if the application does not require high powers, which is often the case with optical trapping experiments or, more notably, in optoelectronic tweezers, where Chiou *et al.* demonstrated the creation of thousands of traps with an LED and a DMD [48]. Additionally, as the DMD is a mirror based device, it presents the opportunity to control multiple wavelengths simultaneously [130].

Incorporation of wavefront shaping into an optical trapping system, however, is far more powerful than just splitting and shaping the beam into multiple traps. Through the use of wavefront correction algorithms, aberrations in optical traps can be accounted and corrected for. By measuring the wavefront of a beam that has travelled through highly scattering or turbid media, and calculating and displaying an aberration of equal but opposite magnitude on the SLM, all aberrations along the optical train can be corrected for [191]. Essentially, a pre-aberration is applied to the plane waves incident on the SLM, so that the aberrations, which the beam will then encounter along the optical train, actually serve to correct the wavefront of the beam, thus allowing for a great increase in the quality of the trapping spot produced and moving the system closer to obtaining a diffraction limited spot. Higher trap stiffnesses could, therefore, be obtained at significantly lower powers, which would be beneficial when heating is of concern. For example, the *in vivo* trapping of red blood cells [106] would greatly benefit from employing such beam shaping techniques, allowing for the trapping of

cells in deeper tissue and at less damaging powers.

2.5 Conclusion

This chapter has described the main theoretical and experimental considerations that should be accounted for when designing and building an optical trapping system. Beam shaping methods have been introduced, which form the basis of chapters 3, 4 and 5. Additionally, force measuring techniques and methods for calibrating optical tweezers have been described, including the power spectrum method, which is used in chapters 3 and 5.

Chapter 3

Characterising Conical Refraction Optical Tweezers

3.1 Introduction to conical refraction

Traditionally, optical tweezers have been created by focussing a single beam of light, with a Gaussian intensity distribution, through a high numerical aperture (NA) lens [16], the theory of which has been outlined in the previous chapter. However, as is often the case, no one tool can perform all the tasks that are asked of it. In order to effectively study microscopic objects, much more than simply applying and measuring force is often required. More and more often, the optical micromanipulation community have turned to beam shaping techniques in order to produce a complementary suite of optical tools. Static kinoforms, which can modify the phase front of a beam in order to produce Laguerre-Gaussian (LG) beams, have been used to transfer orbital angular momentum to optically trapped particles [121]. With the advent of the spatial light modulator (SLM), dynamic holographic optical tweezers (HOTs) have been created [130]. Previously static kinoforms can be calculated, displayed and changed in real time and have brought an unprecedented flexibility to optical tweezers.

Beam shaping techniques, of course, have a significantly longer history than those developed for optical tweezers. One of the earliest manifestations of significant beam shaping is that of conical refraction. This phenomenon was first predicted by Sir William Hamilton in 1832 [192] and confirmed experimentally by Humphrey Lloyd two months later [193]. The success of this experiment greatly contributed to the general acceptance of the wave theory of light proposed by Fresnel [194] over the then dominant corpuscular theory.

In the two centuries that have passed since this first observation, a full explanation based on Maxwell's electromagnetic theory has emerged [195–197]. However, conical refraction is often called the "Forgotten Phenomenon" as there are surprisingly few experimental studies, possibly due to the difficulty in finding, or growing, high quality crystals of sufficient thickness. Indeed, a 2007 article by Berry and Jeffrey [197] reported only seven known experiments on conical refraction, including Lloyd's and the authors' own experiment. With the advent of improved crystal growth techniques, interest in conical refraction is growing, as high quality crystals become more readily obtainable. Described by Raman as "among the most beautiful and striking effects arising in crystal optics", studies into this long-known, fundamental optical effect are providing new insights to the structure of a conically refracted beam [198–200]. Additionally, the unique structure of such a beam has led to interesting practical applications in the field of optical manipulation [123, 124, 132–134].

However, although they were being used to form optical traps, the trapping properties of conically refracted beams had not been fully investigated. Therefore, the work presented in this chapter uses power spectral analysis to quantify the trapping abilities [170] of such beams (assuming the beam is approximated by a harmonic potential well) by calculating the trap stiffness of the three main parts of the beam: the upper and lower Raman spots and the Lloyd/Poggendorff rings.

3.2 Overview of the theory of conical refraction

The complexity of the physics involved prevents a simple explanation to be offered, while a full description of the theory governing the effect is far beyond the scope of this chapter. Therefore, a descriptive overview of how conical refraction occurs is offered, in order to provide an understanding of the work presented in this chapter, while an in depth analysis can be found in the literature [194–198, 201].

3.2.1 Optical classification of crystals

It is possible to place transparent crystals into one of three distinct groups based upon their optical properties: optically isotropic, uniaxial or biaxial [138, 195].

Optically isotropic crystals

The simplest case to consider is that of crystals which belong to the cubic crystal system, figure 3.1(a), such as sodium chloride. These crystals have a relatively simple and highly symmetric atomic arrangement [202]. If a point source of light was embedded within an such a crystal, it would propagate uniformly in all directions as a spherical wave [138]. There would be no preferred direction of propagation, just as with an amorphous solid, and the light will encounter only a single refractive index, hence optically isotropic.

Uniaxial crystals

A crystal with an asymmetric structure, such as in the case of hexagonal, tetragonal or trigonal systems, figures 3.1(b) - (d) [202], will have an anisotropy in the binding force of the electrons to the atoms, which will present as an anisotropy in the refractive index [138, 202]. Assuming that the binding force is governed only by the atomic separation in the crystal, a simple example

would be linearly polarised light travelling along the x-axis of a tetragonal system, as defined in figure 3.1. When the electric field lies along the y-axis, the light would experience one refractive index. However, by rotating the electric field to lie along the z-axis, the light would experience a second refractive index [138]. A crystal of this sort would cause an unpolarised beam of light incident on the crystal to split in two, producing double refraction, an effect known as birefringence.

In the these systems, there will be a direction in which the atoms are arranged symmetrically. This direction is termed the optic axis, as light propagating along this axis will experience a single refractive index regardless of polarisation and so does not produce birefringence. Hexagonal, tetragonal or trigonal systems have only one such direction, so only one optic axis, hence uniaxial [138].

Biaxial crystals

The remaining crystallographic systems, orthorhombic. monoclinic and triclinic, figures 3.1(e) - (g), will exhibit three different refractive indices and two optic axes (hence, biaxial). These crystals will also exhibit double refraction, but propagation of light along the optic axis is substantially different from the uniaxial case [203], as discussed below. It is such a crystal that is required for conical refraction.

3.2.2 Conical refraction

The realisation of conical refraction requires an appropriate biaxial crystal, such as aragonite or $KGd(WO_4)_2$, of sufficient length, which has been cut so that one of its optic axes lies perpendicular to the polished, parallel surfaces of the crystal, figure 3.2 [203]. As predicted by Hamilton, a beam travelling along the optic axis in a biaxial crystal will propagate conically inside the crystal and emerge as a conically refracted beam [203]. This unusual beam

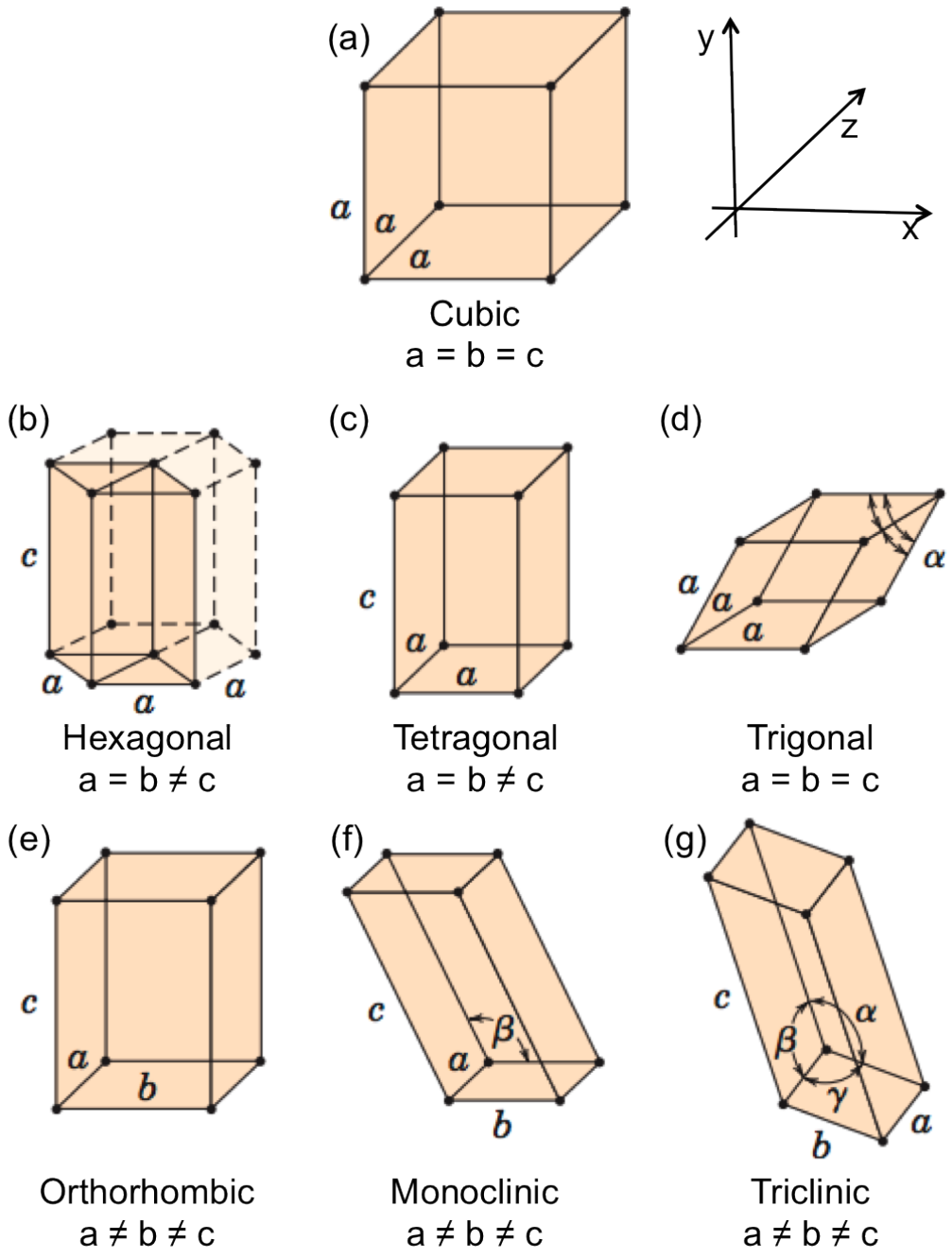

Figure 3.1: The seven crystal systems. (a) cubic crystal, which is optically isotropic. Uniaxial crystals consist of (b) hexagonal, (c) tetragonal or (d) trigonal systems. Biaxial crystals consist of (e) orthorhombic, (f) monoclinic or (g) triclinic systems. [138, 195]. Axial lengths are denoted as a, b and c, with interaxial angles represented by α, β and γ. Image adapted from [202].

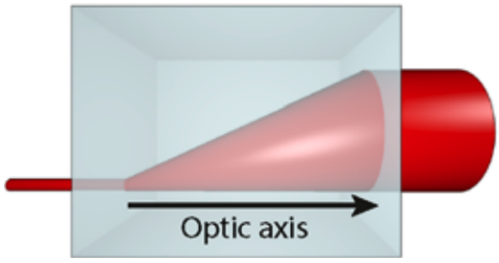

Figure 3.2: Illustration of conical refraction in a crystal. Here, the incident beam is coherent and circularly polarised, and the crystal is cut so that one of its optic axes is perpendicular to the polished, parallel surfaces of the slab. Image reproduced from [203].

shape is due to the shape of the wave surface along the optic axis.

By plotting all possible end points for all propagation directions within a crystal, with lengths corresponding to phase velocities, one is able to generate a wave surface diagram [204]. In the case of a biaxial crystal, the wave surface diagram will consist of two shells, one a sphere (a circle in the two dimensional depiction) and one an ellipse, as shown in figure 3.3. These two shells intersect one another at four points, figure 3.3(b), with the two optic axes of the crystal, defined by the red arrows in figure 3.3(b), joining the origin with these points [195]. At each intersecting point, the surface takes the form of a double cone, as can be seen in figure 3.3(d).

Hamilton noticed that due to the double cone shape at the point of intersection, the normals to the surfaces are not defined, so there are infinitely many normals [197]. Indeed, the normals to the wave surface define the ray cone, as shown in figure 3.4. This cone structure can be explained as follows. As light, with wavevector direction $\mathbf{k}$ and displacement vector $\mathbf{D}$, propagates along an optic axis and passes through the double cone, the electric field vector $\mathbf{E}$ can be in the same plane as $\mathbf{D}$ and $\mathbf{k}$, but tilted with respect to $\mathbf{D}$. Perpendicular to $\mathbf{E}$ is the Poynting vector, $\mathbf{S}$, which determines the direction of the rays. As the light is travelling along the optic axis, the displacement vector can lie in any direction, therefore the electric field, and hence Poynt-

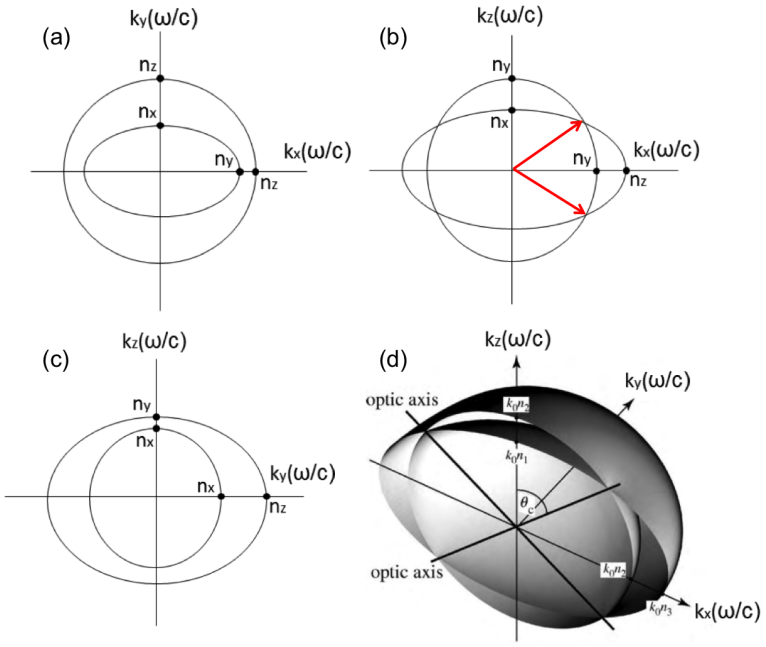

Figure 3.3: (a) - (c) Two dimensional wave surface diagrams, in the (a) xy, (b) xz and (c) zy planes, for a biaxial crystal. (b) shows the intersections between the two surfaces, which causes conical refraction. The red arrows denote the two optic axes. (d) Three dimensional representation of the wave surface. Images adapted from [197, 204].

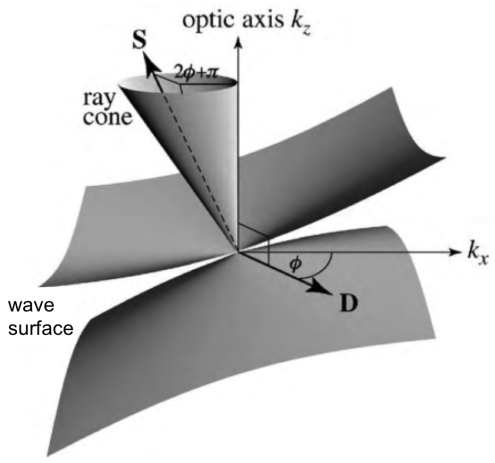

Figure 3.4: Ray cone defined by the normals to the wave surface, generated at the points of intersection of the wave surface. Image from [197].

ing vector, can also lie in any direction. As the displacement vector rotates through its allowed directions, in the plane transverse to **k**, **E** and **S** will also rotate and, as they are tilted at an angle, they will trace out a cone, with the rays travelling along the cone traced out by the Poynting vector, as illustrated by figure 3.4 [195,197,203,204]. This hollow cone will then refract into a hollow cylinder outside of the crystal, as illustrated by figure 3.2.

In practice, however, the ring that is produced is in fact, two closely spaced rings surrounding a dark ring. This can be attributed to off-axis light, i.e. light which is slightly offset from the optic axis, producing rings which are slightly offset from the ring itself. Only a very small amount of light will fall exactly along the optic axis, which is why the ring appears dark when compared with the brighter, offset rings [197].

The radius of the rings produced is proportional to the length of the crystal and, in order to be seen, must be larger than the width of the incident beam [197]. This typically leads to crystal lengths of up to tens of millimetres, which can make finding pure enough crystals of sufficient length somewhat challenging.

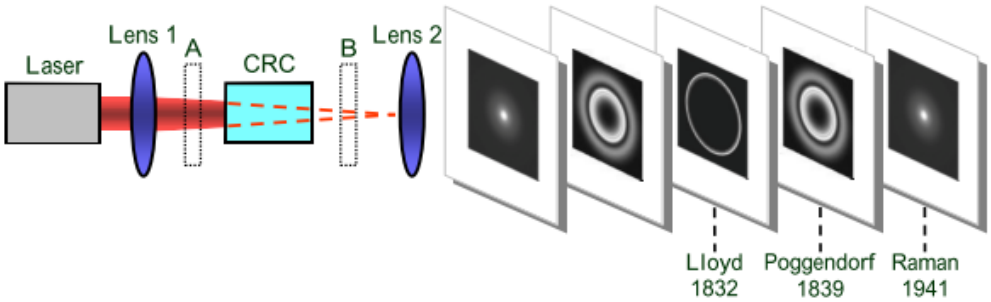

Figure 3.5: Basic structure of a conically refracted beam, which is symmetric around the Lloyd ring plane. Image reproduced from McDougall *et al* [124]

A basic outline of the conical refraction beam structure is shown in figure 3.5 and consists of three main parts: the Lloyd/Poggendorff rings and the upper and lower Raman spots, which are more akin to rods of light than spots [198]. The polarisation distribution in the rings of the conically refracted beam is of interest, as any given point on the rings is linearly polarised, and it undergoes a 180° rotation as the observation point moves around a complete circle of the rings [194]. The phase of the electric field also undergoes a rotation of 180° in a full circle around the rings, thus preventing a discontinuity in the electric field. The implication of this is that any two points opposite one another have orthogonal polarisations. It therefore follows that circularly polarised light is required in order to generate a fully conically refracted beam, as information from all electric field components is necessary. If the beam incident on the crystal is linearly polarised, there would be a missing section in the Lloyd/Poggendorff rings and the intensity would change along the ring, figure 3.6. The missing segment is located parallel to the input polarisation and, had the incident beam contained the corresponding electric field component, would have a polarisation perpendicular to that of the incident beam [197].

The polarisation state of the Raman spots is substantially more complex due to the presence of polarisation singularities and their dependence on in-

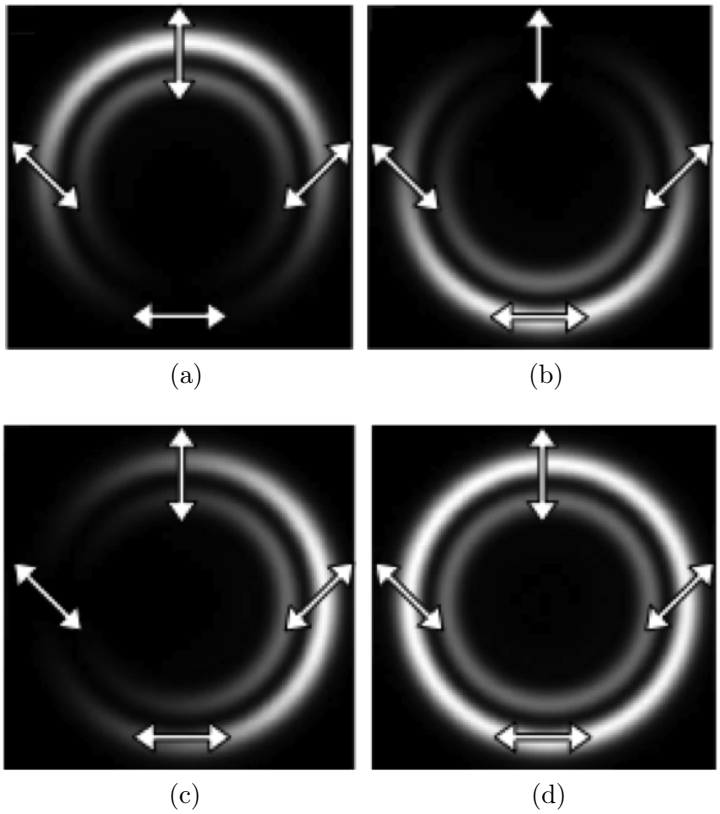

Figure 3.6: Simulation of the intensity and polarisation distributions for a conically refracted beam. Figures show Lloyd/Poggendorff rings generated when incident light is (a) vertically, (b) horizontally, (c) diagonally and (d) circularly polarised. Image adapted from [194].

put polarisation. For example, Turpin *et al.* found that for right handed circularly polarised incident light, the upper Raman spot consisted of alternating annular regions of right handed and left handed circularly polarised states, separated by circles of linearly polarised singularities [205]. For linearly polarised incident light, the authors showed that the field of the Raman spot is broken by polarisation singularities manifesting as a line of null-intensity that connects two orthogonal, linearly polarised points [205].

3.3 Experimental system

The conical refraction optical trap was generated with a 12 mm long biaxial crystal of $KGd(WO_4)_2$ and a 1 W (maximum output) 1070 nm fibre laser (Model PYL-1-1064-LP, IPG Photonics) as the trapping source. The facet of the crystal was orientated perpendicular to the beam propagation axis, with the beam focussed to a point beyond the crystal. The experimental system is shown in figure 3.7. Removable half-wave and quarter-wave plates were included before the biaxial crystal in order to facilitate switching between linear and circular input polarisation to the crystal. The main optics of the system were placed in a straight line (the optics focussing the laser through the crystal and the imaging optics, up to the dichroic beamsplitter) in order to avoid any unwanted polarisation effects that lead to a nonuniform ring pattern [124]. A Nikon 0.9 NA 50x oil immersion objective was used to focus the conical beam and form the optical trap, while a Nikon 1.25 NA 100x oil immersion objective was used to image the sample onto the CCD camera and to image the beam onto a quadrant photodiode (QPD). Although inverted microscopes are more common in optical trapping, chapter 1.2.4, the imaging path of the system was based upon an upright microscope, with the sample illuminated from below and imaged from above, as previous work [124] has shown differences in beam spot appearance when imaged in transmission and reflection mode. As shown in figure 3.8, due to the polarisation sensitive op-

tics used in the set-up, depolarisation issues cause differing intensity patterns when imaging the conical trap from below.

A 10 mm diameter, silicon QPD was used in back-focal-plane interferometry (BFPI) mode, chapter 2.3.1, [17] and was connected to custom built transimpedance amplifiers, which were in turn connected to a National Instruments SCB-68A connector block. An in-house LabVIEW program was used to analyse the signals collected by the National Instruments PCI-6250 data acquisition (DAQ) card. Mounting the imaging and QPD systems on individual xyz-translation stages enabled axial scanning of the focussed beam, thus allowing for the full beam profile to be imaged by the CCD camera and the QPD to be realigned to the new position.

3.4 Beam shape characterisation using beam profiler

In order to ensure that a fully conically refracted beam was generated in the trapping plane, an initial investigation of beam shape was performed. A beam profiler was placed in a conjugate plane to the CCD camera and the beam was scanned axially by moving the translation stage. The imaging system was moved in 0.25 μm steps, while sequential images of the beam from the beam profiler were saved and used to generate a full 3D scan of the conically refracted beam. An example of the z-cross section of a circularly polarised beam, under high NA focussing, with and without a trapped bead, is shown in figure 3.9.

If the beam incident on the crystal is linearly polarised, a section of the Lloyd/Poggendorff rings will be missing. As shown in the inset of figure 3.7, there will also be an intensity change along the ring, which, it should be noted, agrees with the simulation by Berry and Jeffrey [197] that is shown in figure 3.6. This "gap" in the rings, located parallel to the input polarisation, would have had polarisation that was perpendicular to the input polarisation,

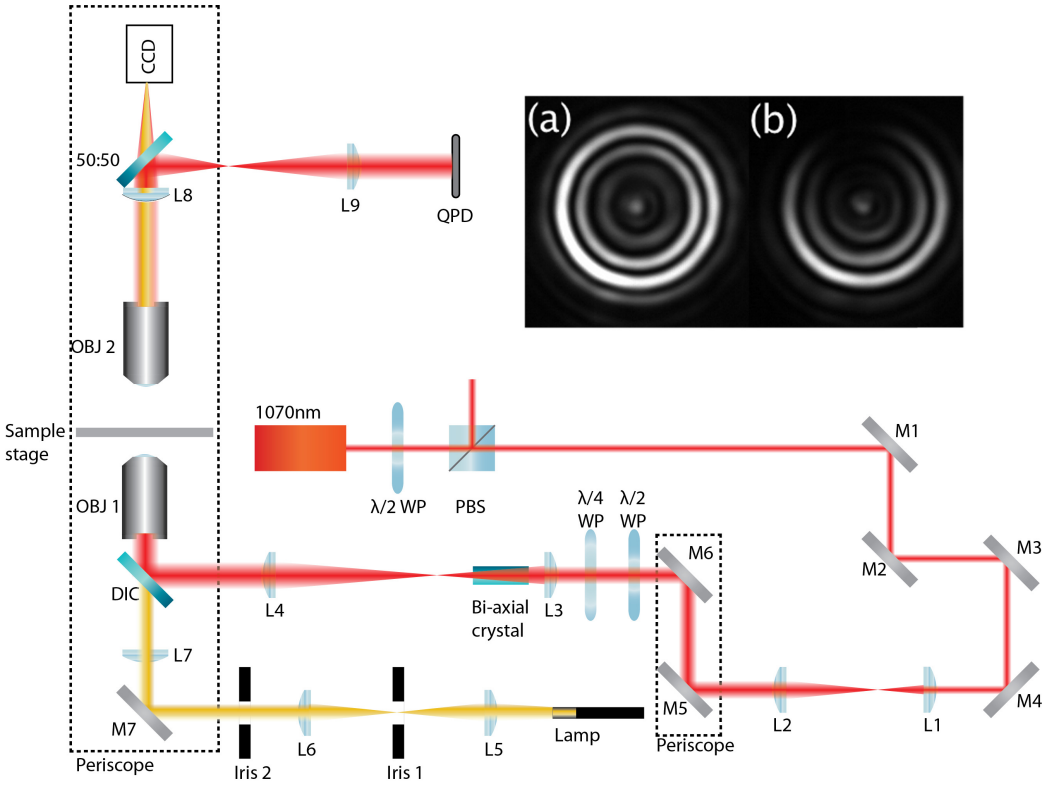

Figure 3.7: Experimental system used for conical refraction optical tweezers. OBJ 1, Nikon 0.9 NA 50x oil immersion objective; OBJ 2, Nikon 1.25 NA 100x oil immersion objective; PBS, polarising beam splitting cube; $\lambda/2$ WP, half-wave plate; $\lambda/4$ WP, quarter-wave plate; DIC, dichroic mirror; L#, lens; M#, mirror. Not shown: sample stage was positioned on a Newport xyz-translation stage; OBJ2, L8, L9, 50:50 splitter and CCD camera were positioned on a second Newport xyz-translation stage; QPD was positioned on a third Newport xyz-translation stage. Inset shows Lloyd/Poggendorff rings generated with (a) circular and (b) linear incident beam polarisations. Out of focus light is visible within (and surrounding) the Lloyd/Poggendorff rings due to the depth of field of the imaging system.

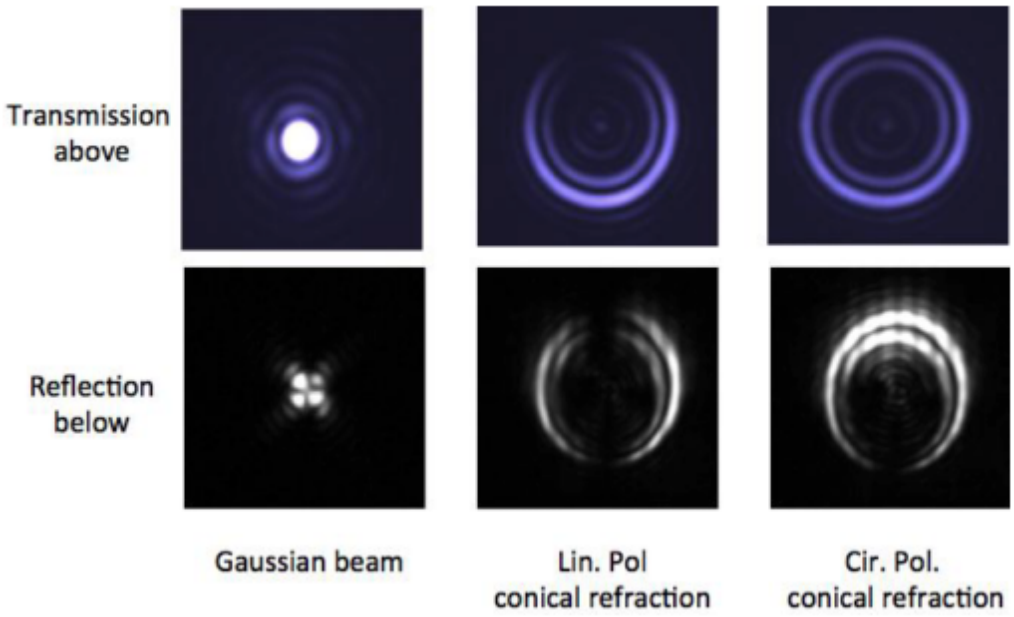

Figure 3.8: Differing intensity patterns in beam spot when imaged in transmission (above) and reflection (below). Images reproduced from McDougall *et al* [124].

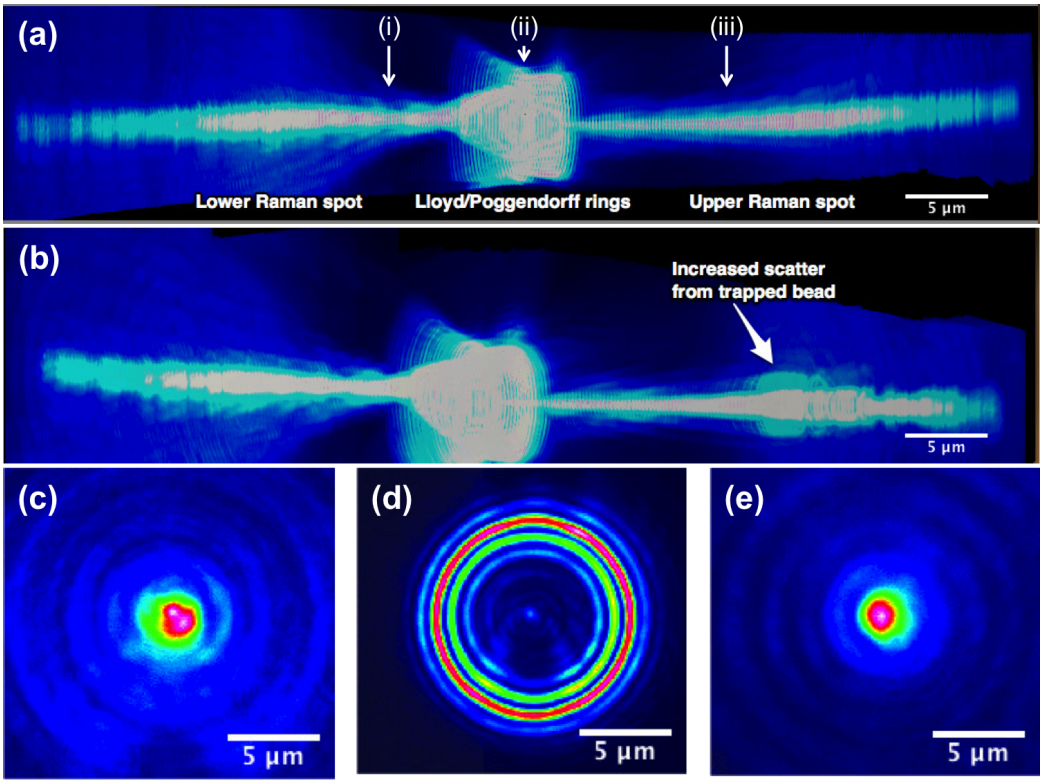

Figure 3.9: Circularly polarised, conically refracted beam, propagating from left to right, ≈ 75.5 µm long, focussed with a 0.9 NA oil immersion objective. (a) Empty trap, three main parts of the beam are labelled. (b) 2.56 µm bead in upper Raman spot, identifiable by increased scatter. The slight asymmetry in the images is due to the projection method used. Cross sections of an empty trap are shown for (c) the lower Raman spot, (d) the Lloyd/Poggendorff rings and (e) the upper Raman spot. The planes of the conically refracted beam where (c) - (e) were recorded are denoted, respectively, by (i) - (iii) on (a)

had the incident beam contained the corresponding electric field component [197]. In this case, trapped particles would move up the intensity gradient and come to rest opposite the missing section of the beam, where the intensity is highest.

3.5 Trap stiffness measurements

In order to quantify the trapping ability of a conically refracted beam, the trap stiffness as a function of input polarisation and trap location was calculated. Silica beads, 2.56 μm and 5.2 μm in diameter, were trapped with various trap powers in all three locations of the conically refracted beam, which was generated with both linear and circular input polarisations. 5.2 μm beads were chosen as they are comparable in size to the radius of the Lloyd/Poggendorff rings (approx 5.3 μm), with 2.56 μm beads approximately comparable in size to the 3.1 μm diameter lower Raman spot. The trap stiffness was calculated for each condition, the results of which are presented in figure 3.10, and investigated as a function of trap location and trap power. All of the following reported powers were measured in the trapping plane.

To perform a trap stiffness measurement, a particle was trapped and the camera moved to bring the trapped bead into focus. The particle was then released and the QPD aligned to the empty trap, so that all four quadrants produced the same voltage, thus giving a zero-signal for each of the three dimensions. The particle was then trapped again and the QPD sampled, in 4 second windows, at a rate of 50 kHz. The 4 s sample period is chosen in an effort to minimise drift in the system. For example, it is easy to imagine that the thermal fluctuations of the bead will drift around a fixed origin over the 20 s sampling time. However, there would be periods of time over which the drift from a local origin is negligible, illustrated by figure 3.11. Therefore, the data should be binned into these "windows" where there is negligible drift from the local origin yet contain enough data to obtain an accurate result

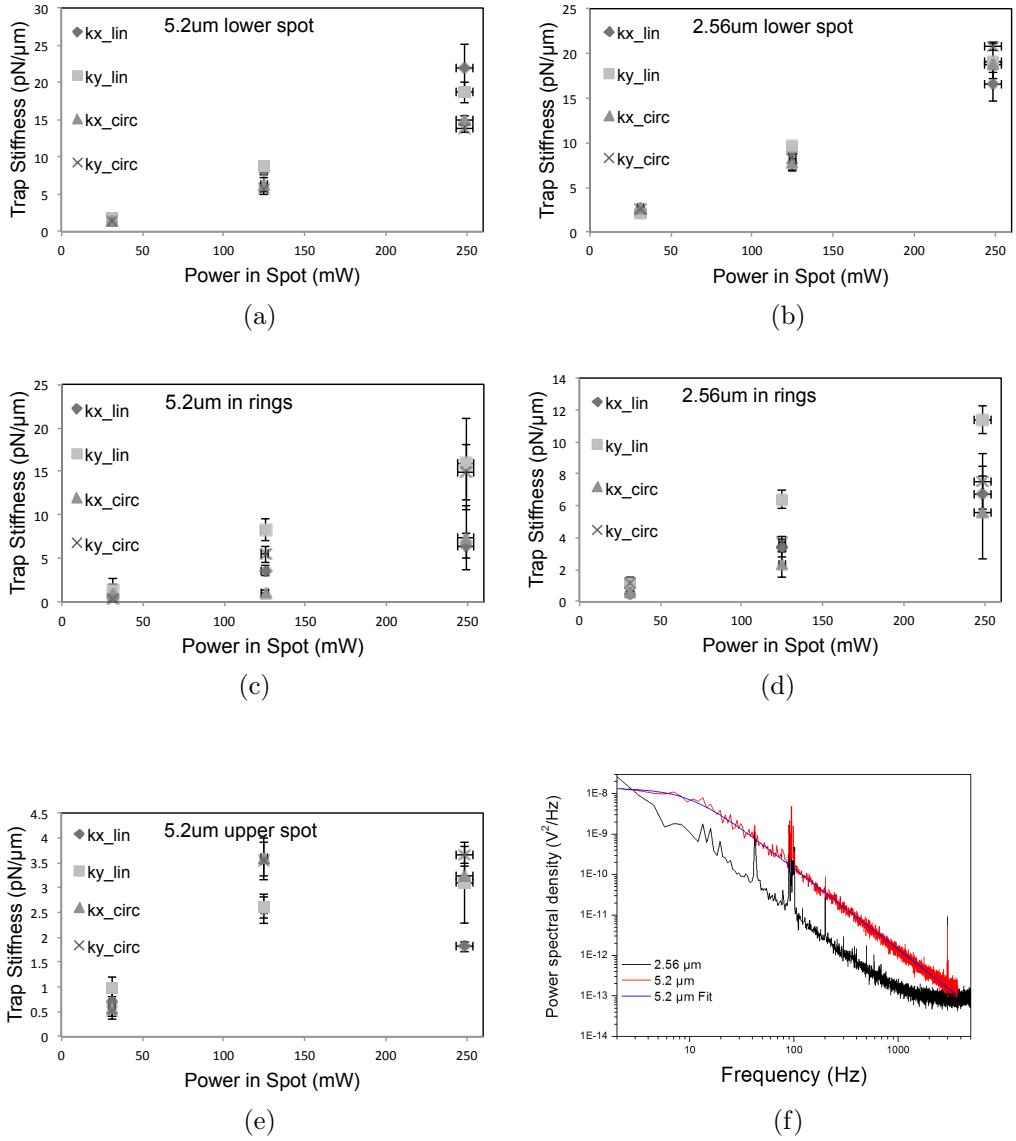

Figure 3.10: Trap stiffness as a function of trap power for: (a) 5.2 μm and (b) 2.56 μm beads trapped in lower Raman spot; (c) 5.2 μm and (d) 2.56 μm beads trapped in Lloyd/Poggendorff rings; and (e) 5.2 μm bead trapped in the upper Raman spot. kx_circ, ky_circ, kx_lin and ky_lin denote the trap stiffness in x and y directions for circular and linear input polarisations. (f) power spectrum for a 2.56 μm bead trapped in the upper Raman spot, shown in black. For comparison, the averaged data of a 5.2 μm bead trapped in the upper Raman spot (red trace), and its corresponding fit (blue trace), are shown.

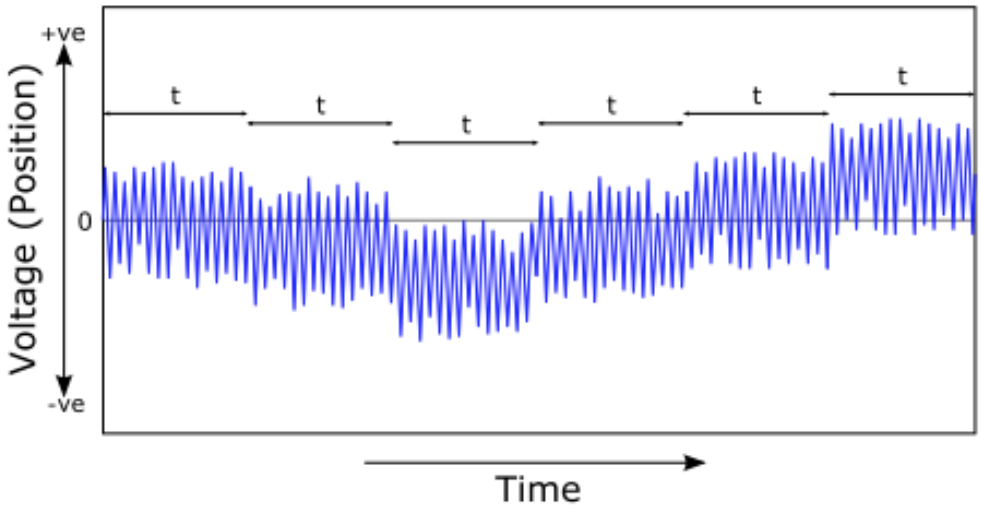

Figure 3.11: Illustration of voltage vs time output from a QPD. Note that although there is significant drift around the fixed origin throughout the sampling time, there is very little drift in each sample "window", t. Image adapted from [137]

once all periods have been averaged. The best way to determine the length of the sample period is through Allan variance [206].

Power spectra were calculated from the average signal of five of these windows and the trap stiffness in x and y, k_x and k_y respectively, was determined from the average corner frequency of 10 power spectra [170]. This was achieved by importing the time domain x and y position data into a second LabVIEW program. The power spectrum analysis program would calculate a single-sided power spectrum for each period of time-domain data before averaging all of them to give the final set of data. The obtained, Fourier transformed, data is exponentially distributed [170] and the analysis software performs a non linear least squares fitting of the Lorentzian [137], which requires a Gaussian distribution of the data. Therefore, the data must be binned into predetermined frequency windows by replacing the frequency range with the average frequency over the bin and the power value with their

mean and associated standard deviation [137]

The QPD detects the change in the z position of the trapped particle by summing over all four quadrants. The spot on the QPD will change size due to the change of relative phase between incoming and scattered waves, caused by the Gouy phase shift intrinsic to focussed beams [49]. The amount of light collected by a high numerical aperture lens, as is the case with this experimental set-up, will not differ greatly from the total amount of incoming light, thus rendering the QPD fairly insensitive to particle fluctuations in the axial direction. It is for this reason that only k_x and k_y are determined.

Trap stiffness as a function of trap location

The highest trap stiffness for the beam was found, for both polarisations and both particle sizes, in the lower Raman spot, represented by figures 3.10(a) and 3.10(b). Both bead sizes trapped at the top of the lower Raman spot, before it evolves into the ring planes. A slight focussing of the beam at this point is observable in figure 3.9(a), indicating that there could be a peak in the gradient force here and, therefore, increased trapping performance. Indeed, the small error bars in both graphs also suggest that, for both particle sizes and both input polarisations, a stable 3D trap is formed. Trapping a 5.2 μm particle at the top of the lower Raman spot with (125 ± 2) mW, and linearly polarised light incident on the crystal, gives a trap stiffness of (8.2 ± 0.7) pN/μm (figure 3.10(a)). As discussed in subsection 3.5.1, the achievable trap stiffness for the same particle under similar conditions, but trapped with a Gaussian shaped trap, is significantly higher, with an average trap stiffness of (49 ± 13) pN/μm.

Both bead sizes can be trapped in the Lloyd/Poggendorff rings, but at the expense of a lower trap stiffnesses than that of the lower Raman spot (figures 3.10(c) and 3.10(d)). However, this decrease in trapping performance is compensated for by the gain of rotational control of the particles. By rotating the waveplates, it is possible to rotate the trapped particles around

the circumference of the rings [124, 132]. This occurs as, upon rotation, the beam incident on the crystal will no longer be perfectly circularly polarised, so the intensity of the Lloyd/Poggendorff rings will not be uniform and "hot spots", or regions of higher intensity, will appear. An extreme example of this is when linearly polarised light is incident on the crystal and a section of the rings is missing [197]. Trapped particles will therefore move up the intensity gradient and come to rest where the intensity is highest. By rotating the waveplates, one can rotate where the "hot spots" form and, hence, rotate the particles.

A very small trap stiffness was found for 5.2 μm particles trapped in the upper Raman spot, shown in figure 3.10(e), indicating levitation rather than gradient trapping. However, calculated power spectra for 2.56 μm beads in the upper Raman spot, figure 3.10(f), display the same characteristic shape as power spectra for an empty trap [170], despite there being a particle present. These smaller particles may rise and sink with laser power fluctuations, while the larger beads appear more stable in the upper Raman spot. The power spectrum in figure 3.10(f) falls off as $D/\pi^2 f^2$, where D is the diffusion coefficient for a particle in water [170], which is characteristic of free diffusion. The particle, therefore, is moving as if the trap did not exist and is free to diffuse over a relatively large volume, in comparison to particle diameter, which indicates that it's experiencing an approximately flat trapping potential. Owing to the converging and diverging nature of the focussing envelope of the beam, there is a diverging beam at the top of the upper Raman spot, so it can be inferred that there is a lower potential gradient.

Trap stiffness as a function of trap power

In order to further quantify the trapping properties of a conically refracted beam, trap stiffness was investigated as a function of trap power. The trap stiffness of the lower Raman spot was found, as expected, to increase linearly with increasing power, shown in figures 3.10(a) and 3.10(b). This held

for both particle sizes trapped with both polarisation states, further demonstrating that a true 3D gradient force trap is formed at the top of the lower Raman spot.

The same linearly increasing trend was also observed for the particles that were trapped in the Lloyd/Poggendorff rings. However, as shown in figures 3.10(c) and 3.10(d), when the particle is trapped with linear input polarisation there is an asymmetry in the x and y trap stiffnesses, k_x and k_y, which becomes more pronounced with increasing trap power. This asymmetric trap stiffness could be attributed to the changing intensity gradient in the rings, caused by the "missing" polarisation contribution from the incident beam.

Figure 3.10(e) clearly shows that there is a small, albeit significant, change in the trap stiffness, with increasing power, of a 5.2 μm bead trapped in the upper Raman spot. Additionally, there was no change in the power spectra for the 2.56 μm beads in the upper Raman spot with increasing trap power. The power spectra for a trapped 2.56 μm bead still had the characteristic shape of free diffusion even at the highest trapping power used, (249 ± 5) mW, when a traditional Gaussian trap would have had its highest trap stiffness. This provides further indication that levitation is occurring in the upper Raman spot, as opposed to gradient trapping.

3.5.1 Levitation investigation

To verify that beads were levitating in the upper Raman spot, bead position was investigated as a function of power. Beads were trapped in the upper Raman spot and brought into focus on the CCD camera. The trap power was varied from (2.61 ± 0.10) mW to (363 ± 5) mW and, at each new power, the imaging system was moved to bring the bead back in to focus on the camera. The increase in height above the Lloyd/Poggendorff rings, as a function of increasing power, for a 5.2 μm bead is shown in figure 3.12. This is characteristic of optical levitation and, when combined with the weak trap stiffnesses shown in figure 3.10(e) and the power spectrum shown in figure

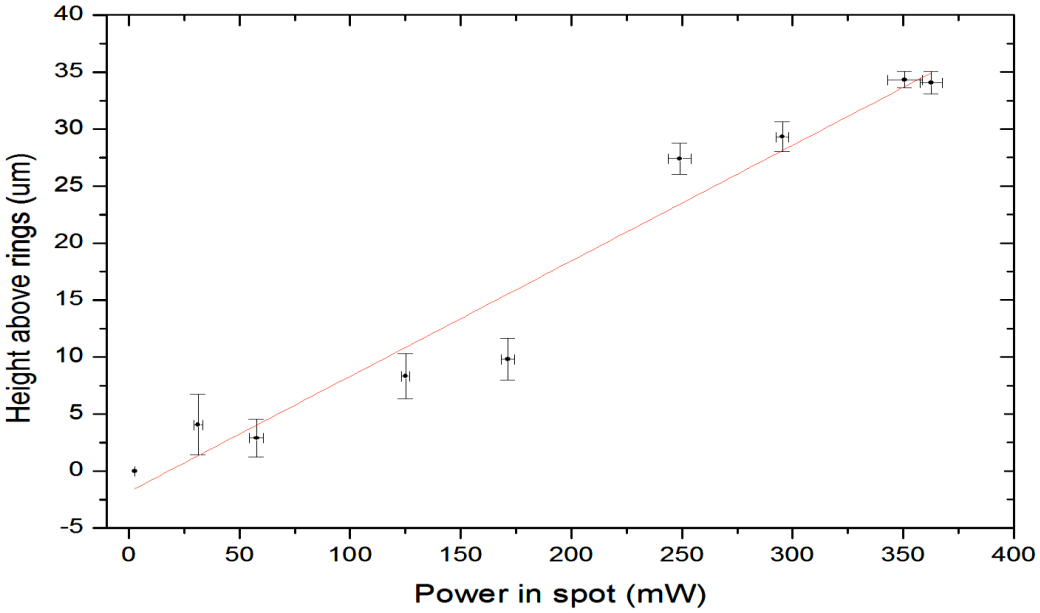

Figure 3.12: The height of a 5.2 μm bead above the Lloyd/Poggendorff ring plane as a function of trap power.

3.10(f), can be taken as proof that optical levitation, rather than optical gradient trapping, is occurring in the upper Raman spot. Increasing trap power produced no observable change in axial position of the bead in neither the lower Raman spot nor the Lloyd/Poggendorff rings, further indicating that there must be a 3D gradient force present in these locations.

To verify that the observed levitation was not due to the comparatively low NA of the trapping objective, the Nikon 0.9 NA 50x oil immersion objective was used on a traditional, Gaussian beam, optical trapping system. There was no change in the axial position of the bead as a function of power, indicating that 3D gradient trapping was occurring. A measure of the trap stiffness of the system was performed by calculating the power spectra for a 5.2 μm bead trapped with (137 ± 6) mW of power in the Gaussian beam, an example of the obtained power spectra is shown in figure 3.13. An average trap stiffness of (49 ± 13) pN/μm was determined, which, when combined

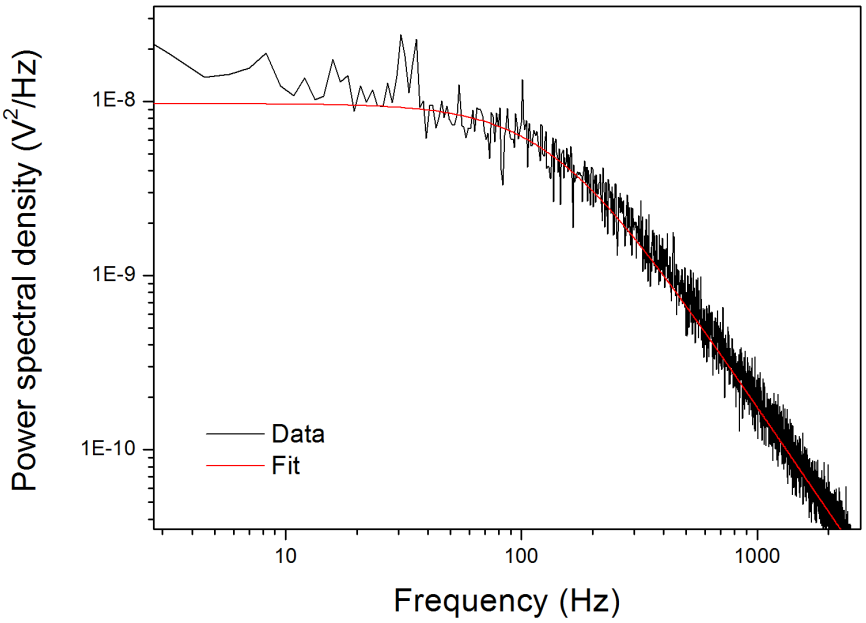

Figure 3.13: An example power spectrum obtained for a 5.2 μm bead trapped with (137 ± 6) mW in a Gaussian trap. The Lorentzian function (red trace) fitted to the averaged data (black trace) gives a corner frequency of ≈ 135 Hz, which corresponds to a trap stiffness of ≈ 42 pN/μm.

with particle position being independent of trap power, shows that it is possible to achieve 3D gradient trapping with a 0.9 NA objective. Therefore, the observed levitation is due to the conically refracted beam and not the low NA objective.

In an effort to extend the trapping limit of the upper Raman spot, the conical trap was generated with a 1.25 NA oil objective. However, the conical pattern that was produced was too compact to trap, separately, in all three components of the beam.

3.6 Conclusion and future work

Through the use of power spectrum analysis the trapping properties of a conically refracted beam, in each of the three trapping regimes of the beam, have been quantified. The trap stiffnesses of 5.2 μm and 2.56 μm beads were calculated, at three different powers, when trapping in the upper and lower Raman spots, and the Lloyd/Poggendorff rings. It has been demonstrated that the good trapping ability of the lower Raman spot allows it to function as a conventional, gradient force, optical trap, due to its comparatively high trap stiffness, which increased linearly with increasing trap power. The trap stiffness decreases, relative to the lower Raman spot, but remains sufficient to trap a particle in three dimensions when trapping in the Lloyd/Poggendorff rings. However, this loss of trap stiffness is offset against the gain of rotational control of the particles in this plane. Again, trap stiffness was shown to increase linearly as a function of trap power, as expected. Finally, it was shown that optical levitation occurs in the upper Raman spot, with particle height above the Lloyd/Poggendorff rings increasing as a function of trap power. A quantification of the distance of particle guiding as a function of power was provided, with particle guiding distances of approx. 35 μm achievable. Applications which require trapping, rotation and guiding could, therefore, be achieved through the use of a conically refracted beam. Thus negating the need for complex beam shaping techniques using, for example, spatial light modulators.

Recent work studying the impact of azimuthally and radially polarised light [200], as well as the effect of phase structured beams [207–209], on the shape of the conically refracted beam has highlighted the importance of polarisation and beam shape in conical diffraction. The trapping properties of such beams remains unexplored and could warrant further investigation. The study of photophoretic manipulation could benefit from conically refracted beams, as confinement of light absorbing particles would be possible in the dark regions of the beam, enclosed by the Lloyd/Poggendorff rings [210].

Additionally, applications which exploit the hollow cone at the centre of the beam could be found in the field of 3D stimulated emission depletion (STED) microscopy [3].

Chapter 4

HoloHands: Games Console Interface for Controlling Holographic Optical Manipulation

4.1 The need for control

The previous chapter highlighted the power of optical tweezers when combined with beam shaping and perfectly illustrated the multifaceted nature of this technique. Indeed, it is the versatility of optical tweezers that makes them ideally suited for the use and development by a wide range of non-expert users. This is observable in the growing number of commercial optical trapping systems from companies such as Thorlabs, JPK and Elliot Scientific, as well as the development of optical tweezers attachments for commercial microscopes, such as from Impetux, to transform commercial trapping systems into quantitative, force measuring, optical tweezers.

The methods by which optical tweezers are typically controlled, via beam steering mirrors, acousto-optical deflectors (AODs) or by spatial light modulators (SLMs), lend themselves naturally to computer control. In turn, this allows for the development of flexible human-computer interfaces. The de-

velopment of user-friendly control techniques has risen due to the growing acceptance of the idea that optical tweezers are a useful, quantitative tool for research. These techniques are generally aimed at enabling the "non-expert user", which is usually a misnomer, to control sophisticated systems in a straightforward way. In its simplest form, this would consist of a "point and click" design: the user sets trap location by using the mouse button to click the live video, displayed on the computer monitor, in the region where they want the trap created. However, by turning to the computer and video games industry, much more exciting forms of control can be developed.

The development and refinement of interface systems for intuitive control of virtual worlds has been a large area of research within the computing industry. Consequently, modern games controllers are packed with cutting edge technology and high-end components, and are available at a low cost due to the massive demand. Building on the hard work of the industry, and exploiting the high-end devices that it has created, intuitive control systems for optical traps can be developed. Users are now able to, essentially, "feel" their microscopic sample due to interfaces that provide force feedback [211, 212]. Touchscreen systems have enabled independent, but simultaneous, control of multiple traps by multiple users [213]. The multitouch ability of Apple's iPad has allowed for the development of interfaces that can control multiple traps in two dimensions, with the "pinch" gesture used to move particles in the third dimension [214]. Finger tip tracking has been implemented to create a "microhand", with each finger tip corresponding to a trapped bead, which can be used to manipulate objects that may not optically trap for any number of reasons [215]. There has been a shift, in recent years, in the gaming industry to interfaces where the user is the "controller" and optical tweezers have followed suit, with the development of optical tweezers systems that are controlled with a Microsoft Kinect [216–218], which forms the basis of this chapter.

While such interfaces are not crucial for optical tweezers, an effective

interface is generally viewed as being vital to the wider acceptance of a device. However, optical tweezers are already finding widespread acceptance and use by researchers in other scientific disciplines. While an argument can be made that non-expert users would rather have the system tucked, neatly, inside a sealed box and not have to realign lenses and mirrors on a daily basis, this is often not the case in many of the interdisciplinary fields in which the modern academic now works. Non-expert users will often work alongside optical physicists or engineers as part of their group, or can become experts themselves. Therefore, the development of such control techniques, while being of some technical interest, may not be of much practical use for the research lab. At least, not until touch screen tablet technology is more heavily incorporated with commercial optical instruments, which, with the release of iPad controlled optical tweezers by Boulder Nonlinear Systems, may be a development that will happen in the near future.

The use of whole-body tracking systems, such as the Kinect-based system presented in this chapter, is therefore, conceivably, of limited cutting edge scientific interest. However, as it is based on high volume, commercial technology it is low cost and, with Microsoft's release of a software development kit (SDK) for the Kinect, it is relatively straightforward to program using tools such as Visual Studio. With the proliferation of optical trapping systems and beam manipulation techniques in undergraduate teaching laboratories, the Kinect offers a low cost and intuitive interface to control much higher-end, and therefore expensive, equipment. Thus allowing for the development of a range of interdisciplinary skills for student learning and engagement. Additionally, Kinect controlled optical tweezers could be deployed in science centres and exhibitions, as well as as in other forms of public engagement activities.

The work presented in this chapter describes a holographic optical tweezers (HOT) experiment that is controlled by gestures, which are detected by a Microsoft Kinect and interpreted by a custom written program called Holo-

Hands. A demonstration of both single and multiple particle manipulation by the HoloHands program is provided, illustrating some of the basic functionality of the device and discussing the limitations and possible extensions to the work. The Stokes' drag technique is employed to calibrate the optical tweezer and a comparison is drawn between calibration through gesture based control and automated calibration, where the controller is not a hand waving about in mid-air.

4.2 Experimental system

A standard HOT setup was constructed, shown in figure 4.1, to be configured for Microsoft Kinect control. A 10 W (maximum output) 1070 nm fibre laser (Model YLR-10-1070-LP, IPG Photonics) was used as the trapping source. The 2.5 mm diameter beam was expanded to slightly overfill a Holoeye PLUTO SLM, designed for use at around 1064 nm. Both the Kinect and SLM were connected to a Windows 7 based PC, with 8 GB of RAM and a 3.40 GHz Intel Xeon E31270 processor, which was also used for the development and running of the HoloHands program.

Initially, program development work, performed by M. McPherson, used the C# wrapper for the OpenNI libraries as, at the time, Microsoft had not released their official SDK for Kinect for Windows. Following the subsequent release of this SDK during the early stages of development, the decision was made to switch to this implementation. This allowed for more straightforward coding and provided better documented library functions. However, owing to the full development system now in use, it was observed that programs were a little more sluggish in execution, which may require careful consideration with regards to the specific application in mind. This difference in speed and efficiency was not quantified - Microsoft's SDK was straightforward to use and achieved the required performance, therefore the results presented in this chapter made use of this implementation of the code.

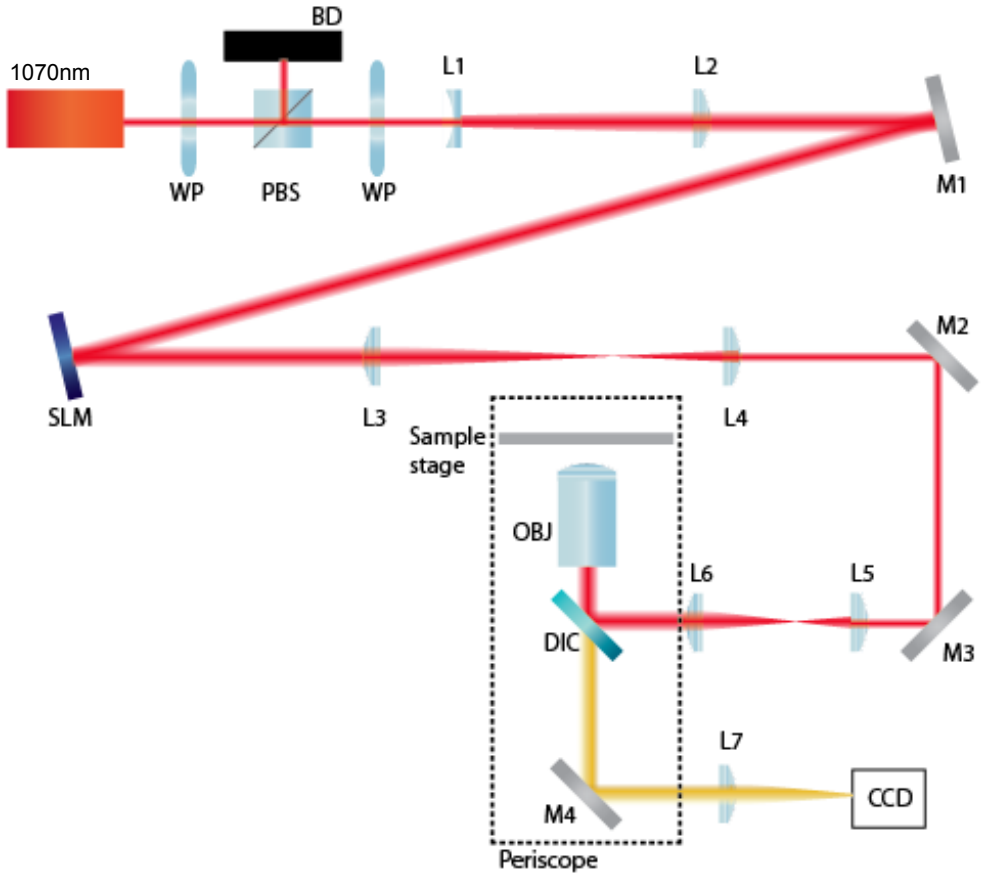

Figure 4.1: Kinect controlled holographic optical tweezers setup. The SLM is connected to the Kinect. OBJ, Nikon 1.25 NA 100x oil immersion objective; DIC, dichroic mirror; WP, waveplate; PBS, polarising beam splitting cube; BD, beam dump; L#, lens; M#, mirror. Not shown here: Kohler illumination; a zero-order beam block placed between L3 and L4; and a Newport xyz-translation stage used to hold the custom made sample holder.

The HoloHands program, figure 4.2(a), tracks the users hands and gives control of the HOT to the user through a series of pre-programmed hand gestures. Waving a free hand back and forth will create a new, active, trapping spot, which can be moved by that hand. Another wave of the hand controlling the active trapping spot will delete the spot. Trapping spots can be locked in place via a "clicking" gesture - moving the trap controlling hand away from, and back towards, the body will "put down" the translating spot. Control of the locked trap can be regained by hovering a hand above above the stationary spot. More complex control can be achieved through building upon this basic functionality and these simple gestures, such as multiple hand tracking and multi-spot manipulation. These functions are demonstrated in the HoloHands video, available online at https://youtu.be/I2iU90EiEis. Each detected hand gesture is translated into a kinoform, a phase-only hologram, by the HoloHands control program.

A simple gratings and lenses [186] algorithm was chosen as the basis for hologram generation. However, when implemented across a 1080×1080 pixel hologram, the program would lag and hang during execution. An increase in program speed and response was achieved by employing a tiling strategy, making use of four tiles. Here, rather than generating a single 1080×1080 pixel hologram, a 540×540 pixel hologram was calculated and repeated four times, i.e. the larger hologram consists of four tiles of the smaller hologram [219], as illustrated by figure 4.2(b). Further optimisation of hologram calculation and display should increase program efficiency and speed, thus achieving a smoother response.

4.3 Results and discussion

Although the Kinect provides for a more intuitive control of a HOT system, the interface is not the most practical for day-to-day work. For example, after even a short period of time, use of the arms to position the optical trap

Figure 4.2: Example of the HoloHands program. (a) The user is able to view themselves on the video display from Kinect camera. The red spot on the video display corresponds to the position of the trapping spot, which, depending on program configuration, can be controlled by hand tracking or automation of the SLM. (b) Red spot location is translated into a grating kinoform, which would be displayed on the SLM to move the trapping spot and, ultimately, a trapped particle. Note the four tiles used to create the tiled hologram.

becomes tiring. Sufficiently eliminating stray motions, which can be detected by the Kinect, can prove to be troublesome. Additionally, although tiling of the kinoform increased program response, there remained a noticeable lag when initiating certain functions, such as creation of a trapping spot. While it is true that these concerns could be improved upon through better hardware or software implementation, it does pose limitations for quantitative work.

The basic functionality of the Kinect control system is shown in figures 4.3 - 4.5. The user is able to view themselves in the top right hand corner of the computer monitor, with light grey spots highlighting hand tracking and red spots representing trapping spots. Having initiated a "wave" gesture to create a trapping spot, a single 4.32 μm silica bead has been trapped by the user's left hand in figure 4.3. A light grey spot on the user's right hand shows that it is also being tracked but the lack of a red spot shows that a second trapping spot has not been generated, hence the untrapped second bead. As shown in figure 4.4, a second trapping spot can be created and used to trap the other bead by initiating a second "wave" gesture, with the right hand this time. Note that a "clicking" gesture has been performed to lock the first particle in position, indicated by the stationary red spot, hence a stationary trap, and the reappearance of a light grey spot over the tracked left hand. Multi-spot movement can be achieved, as demonstrated by figure 4.5, where two particles orbit one another. An example of the aforementioned latency in the program is also highlighted in figure 4.5, with the hand tracker lagging behind the hand movements.

Further improvements to program speed were achieved over time via the introduction of threading into the program and executing different threads for different sections of the program, such as the generation of the final hologram. It was found that using the GetPixel and SetPixel methods (which first retrieve and then set the red, green and blue values for an individual pixel in the kinoform before moving to the next pixel, and so on until every pixel has been addressed individually) to manipulate the bitmaps used to hold

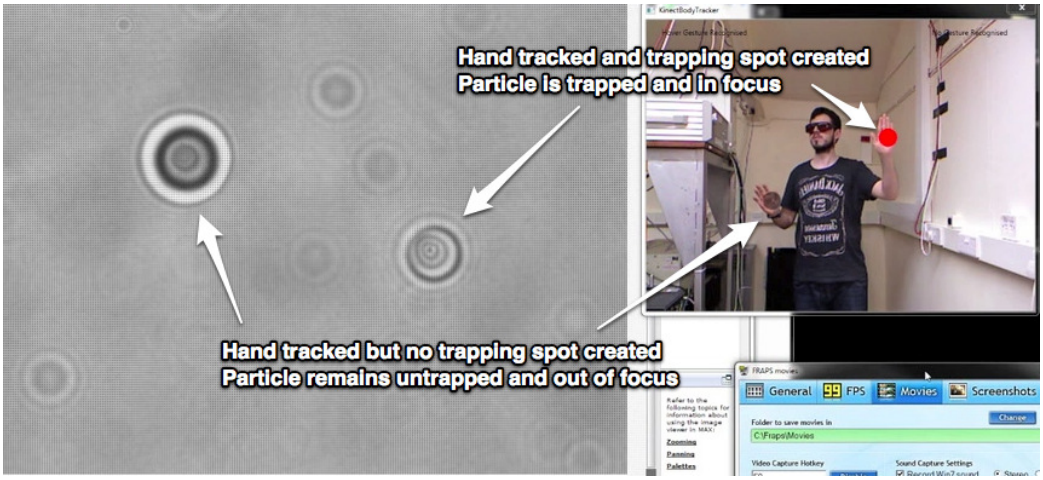

Figure 4.3: Screenshot of Kinect controlled HOT, via the HoloHands program. The user is able to monitor themselves on the right hand side of the screen while simultaneously viewing the microscope view in the left hand side of the screen. Here, a tracked hand is shown to move a single spot, with the trapped 4.32 μm particle in focus while the untrapped 4.32 μm particle remains out of focus.

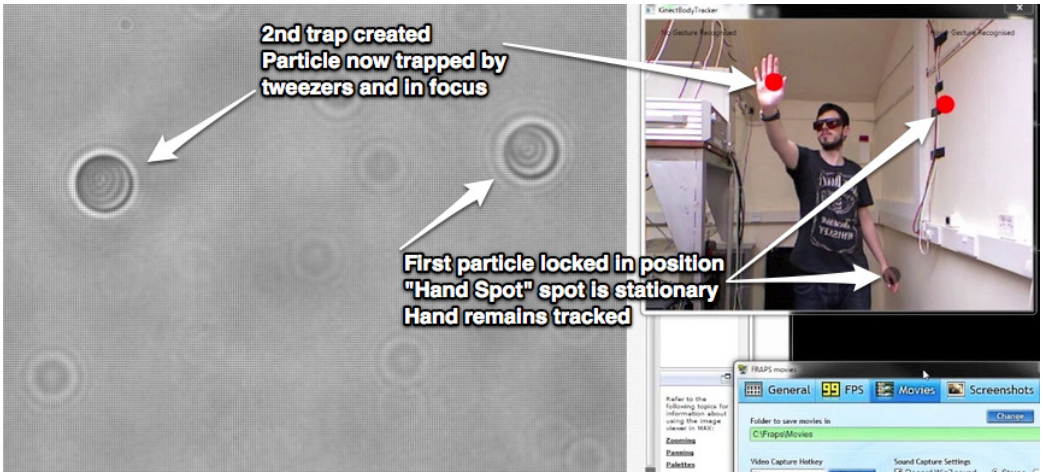

Figure 4.4: Screenshot of Kinect controlled HOT, via the HoloHands program. Two trapped 4.32 μm particles. The left "hand" particle is locked in place while the user controls the right "hand" particle via the Kinect.

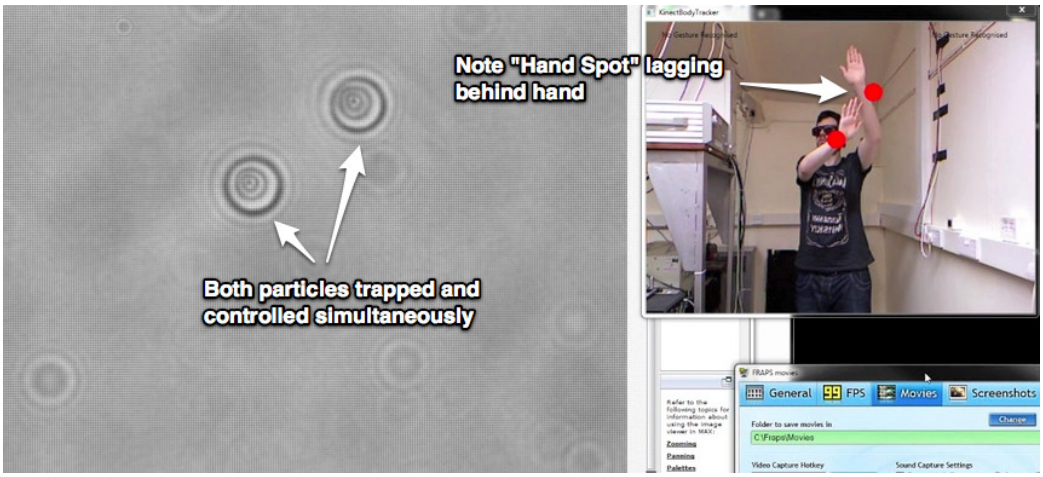

Figure 4.5: Screenshot of Kinect controlled HOT, via the HoloHands program. Kinect control of two trapped 4.32 μm particles. The lag in movement of the trapping spot, compared to the movement of the users hand, is highlighted by the spot near the user's left hand.

and combine kinoforms proved to be a bottleneck in the program. Changing to a LockBits method (which locks a bitmap into memory and allows for large scale changes) to manipulate byte arrays provided a six-times speed increase in kinoform calculation. Yet more significant speed gains could be achieved through further optimisation of the calculation algorithm or moving to a solution based on GPU programming.

4.3.1 Efficiency measurements

In an effort to examine the ability of the Kinect control system to work as a more robust research grade instrument, a simple measure of the transverse Q value [86] of the trapping spot was made. Trapping efficiency of the system was determined by employing the Stokes' drag technique and equations 2.3 and 2.12. In order to determine the effect of user interaction, two implementations were compared. Initially, the HoloHands program was used to generate a trapping spot that was automatically scanned across the experimental field

of view. The automated spot was then replaced by one that was controlled via hand gestures. For both cases, 4.32 μm silica beads were trapped with 55 mW of laser power (measured in the trapping spot) and the speed at which the particle fell out of the trap was measured. The speed of the particle was measured by moving the particle from the top to the bottom of the experimental field of view (either automatically or by hand control), with a routine added to the HoloHands program to measure the time taken for the particle to move between two points. Under these conditions, automatic movement yielded a Q value of 0.0079 ± 0.0002, while a measured Q value of 0.0045 ± 0.0002 was obtained for hand control movement. It was experimentally verified that the trapping spot's intensity did not differ significantly across the experimental field of view and the minimum trapping power for the system was found to be 1 mW. The reduction in Q value between the two cases was unexpected as the same trapping spot was moved in the same direction for each instance of control. The difficulty in keeping hand gestures smooth and at a constant velocity for the full experimental run was often difficult to achieve and could, therefore, account for the drop in Q value.

To gain a better understanding of, and quantify, the smoothness of the hand movements, ImageJ software [220] was used to perform particle tracking on a number of videos, with the resulting displacement versus time graphs for three different hand movement videos shown in figure 4.6(a) - (c). For each video, the trapped particle, the red dot produced by the HoloHands program, and the user's hand were tracked. A close correlation between all three components is shown in figure 4.6(b) - in this case, the hand movement was sufficiently smooth to produce an approximately straight line, with both the red spot and particle following closely. However, this is not the case in figure 4.6(a): although the hand movement is relatively smooth, the red dot occasionally lags behind the hand movement and has to "catch up" with the tracked hand via large jumps. Approximately 0.5 s later, the large jumps of the red dot are translated to jumps in particle position, highlighting the

previously mentioned lag-time in the system. This is more evident in figure 4.6(c), where the hand movement is the least smooth of the three cases. It is unmistakable in this experimental run that the Kinect tracking, i.e. the red dot, can often experience a large lag-time and then, in a fraction of a second, jump position to catch up with the tracked hand. When translated to a kinoform, this results in the particle experiencing jumps of up to 6 μm in as little as 0.034 s. This could have contributed to the unexpected drop in transverse Q value, as the average speed for each experimental run was used in the calculation, neglecting any instantaneous jump that the particle may have experienced during the measurement.

These lags and jumps can serve as good indicators of where delays between user movement and trap response can occur. For the experimental run shown in figure 4.6(b), average dwell times of (0.182 ± 0.012) s for hand movement, (0.209 ± 0.019) s for red dot movement and (0.166 ± 0.016) s for particle movement can be measured. Owing to the small, and comparable, delays, the jumps in movement produced by the program are sufficiently small to give an approximately smooth tracking event. An average jump in hand displacement of (5.7 ± 0.5) pixels gives a corresponding average red dot jump of (6.2 ± 1.6) pixels, resulting in sub-micron average particle jumps of (0.75 ± 0.19) μm. As illustrated by figure 4.6(d), the automatically moved spot produces a much smoother trace. Here, the average dwell times for the red dot and particle movement are, respectively, (0.100 ± 0.012) s and (0.060 ± 0.007) s, which translate to much smaller average jumps of (3.1 ± 0.4) pixels for the red dot and (0.36 ± 0.04) μm for the trapped particle. These smaller jumps in particle position show that the automatic movement is much smoother than the hand control movement, thus attributing to the higher Q value for the automatic movement.

Average particle jumps of (1.5 ± 0.3) μm can be measured for the movement shown in figure 4.6(a), due to the large jumps in hand and red dot movement of, respectively, (10.6 ± 1.3) pixels and (15 ± 3) pixels. These

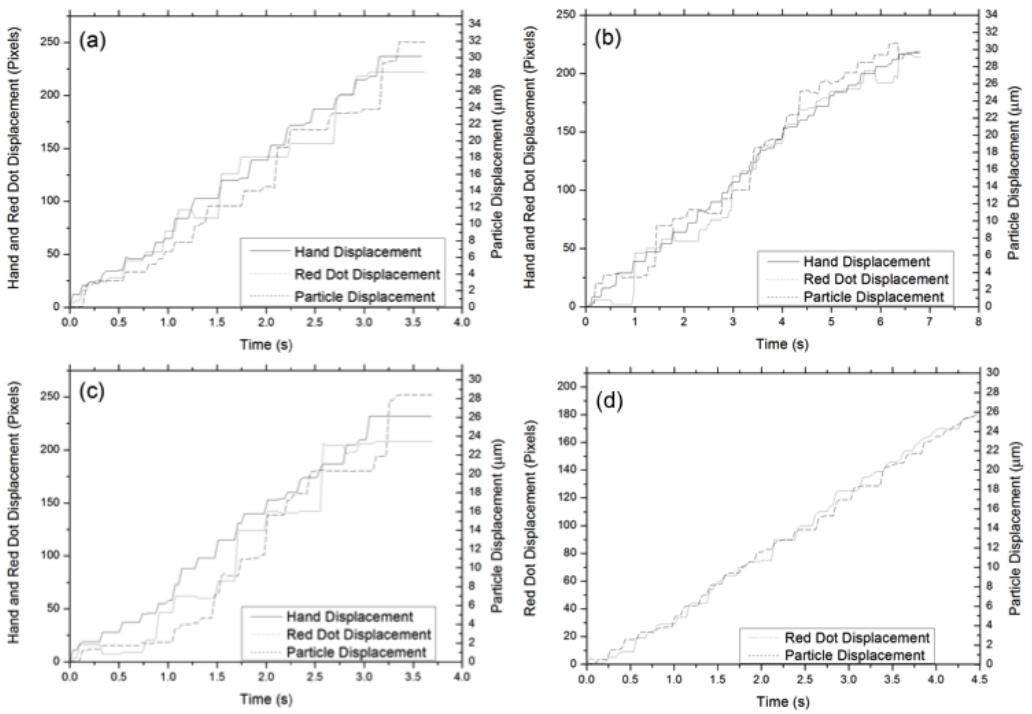

Figure 4.6: (a) - (c) Displacement vs. time graphs for three separate tracking events with hand control movement. In each graph the trapped particle, the red Kinect tracking dot and the user's hand were tracked. (d) Displacement vs. time graph generated by tracking an automatically moved trapped particle and red dot.

large jumps could be attributed to the large variation in dwell times for the three tracked components. Although the average hand displacement dwell time of (0.16 ± 0.02) s is lower than that for figure 4.6(b), there is a noticeably longer average delay in red spot displacement of (0.24 ± 0.04) s. The difference in dwell time for the faster hand movement shown in figure 4.6(a) further highlights the computational lag that can be experienced by the program, possibly contributing to the reduction in Q value.

However, it should be noted that figures 4.6(a) and (c), which show the largest lag-times and jumps in position, correspond to a particle with a velocity of approximately twice that of the particle represented in figure 4.6(b). This provides further indication of the difficulty in performing quantitative measurements with the HoloHands program. Nevertheless, qualitative measurements and trial experiments can easily be performed, while non-expert users would certainly be able to use the intuitive HoloHands interface to control a HOT system.

4.4 Conclusion and future work

The Microsoft Kinect based interface allows for intuitive control of a set of holographic optical tweezers. The versatile system clearly shows the straightforward techniques required for a basic research grade optical trapping system but, without some extra sensitivity or smoothing function to buffer the tracking and particle motion, it lacks the ability to perform quantitative measurements. This is reflected by the system's low Q values of 0.0079 ± 0.0002 for automatic movement and 0.0045 ± 0.0002 for hand movement. The surprising drop in Q value was explained through tracking the movement of the user's hand, the HoloHands generated tracking spot and the trapped particle. It was shown that the trapped particle can lag up to 0.5 s behind the movement of the HoloHands' tracking spot, which in turn can lag behind the user's hand. This resulted in particle jumps of, at times, over 1.5 μm,

thus reducing the system's measured trapping efficiency. While this means that it is challenging for use in precision work, it is not inconceivable that such a system could find use in school or science centre demonstrations.

Although the work presented here makes use of an SLM, the HoloHands program could easily be configured to interface with an AOD or any other computer-based tweezers control systems. As image size did not scale with the size of the person tracked, sensitivity proved to be an issue in the experiments. As such, a person with a larger arm span could move particles further and with greater precision. A form of calibration based on the skeleton detection algorithm could be used to resolve this issue.

The skeleton detection routine would, on occasion, cause the HoloHands program to find and attempt to track inanimate objects present in the scene. Subsequently, a set of co-ordinates could be generated for non-existent hand positions. Future iterations of the HoloHands program would incorporate a secondary "control mechanism", which would require formal activation for a second person entering the scene.

Improvements to gesture detection would prevent similar gestures being confused, thus allowing for the straightforward incorporation of a greater number of gestures. Therefore, gestures that would create more complex beam shapes, such as Laguerre-Gaussian or Bessel beams, could be added to the program. Employing more sophisticated, non-iterative methods of hologram generation, such as random mask encoding of Fourier components [221], could prove beneficial in the efficient calculation of these more complex kinoforms, rather than the simple gratings and lenses algorithm [186] currently used.

High precision work could, in time, be carried out with newer technology coming to the market. The Leap Motion, which alleged, at the time of its release, to be 200 times more accurate than other motion detecting devices and able to track movements as small as 10 μm [222], has since been shown to overcome some of the issues with the HoloHands program [223]. Addi-

tionally, Microsoft have since released an improved “Kinect for Xbox One”, which features, among other improvements, a full HD time of flight camera, compared with the VGA resolution of the Kinect used with the HoloHands program, and increased data processing. Thus, the newer “Kinect for Xbox One” has three times the fidelity and greater accuracy, which would aid with quantitative measurements in optical trapping.

The Kinect itself, however, when coupled with the SDK, offers a cheap computer control for a variety of experimental systems. The type of experiment outlined in this chapter would make an ideal undergraduate project, where the aim would be to develop interdisciplinary skills or partake in interdisciplinary team-working with students from across traditional academic subject areas.

Chapter 5

Examining the Effect of Kindlin-3 Binding Site Mutation on LFA-1 - ICAM-1 Bonds

5.1 Introduction to biological manipulation

Moving on from a discussion of a possible user interface for non-expert users in an interdisciplinary environment, this chapter highlights typical measurements that may be encountered in such environments and illustrates how they can be performed when optical tweezers are exploited as a quantitative tool. Optical traps were originally designed, and reportedly first used, as an atom trap [62, 224]. However, spurred on by a difficult day in the lab, improperly stored containers of the Tobacco mosaic virus (TMV) and a ham sandwich of questionable integrity [62], Ashkin and Dziedzic showed that it was possible to optically trap viruses and bacteria [225]. Although not reported until a year after the seminal paper on atom trapping [224], this work represented the first report of optical manipulation of living cells [225, 226]. Two years later, Ashkin and Dziedzic showed that optical tweezers could be used to apply forces inside living cells and exploit this ability to develop a tool

to study the mechanical properties of a cell's cytoplasm [227]. When these three papers [225–227] are considered together, they mark the beginning of a new field of optical trapping in biology.

From this early work, optical tweezers have become, arguably, one of the most powerful tools in the biophysical sciences. Combining optical tweezers with optical scissors (a technique employing laser-based ablation through pulsed lasers) allowed Berns *et al.* to manipulate chromosomes during cell division [228]. A single kinesin molecule was directly observed by Svoboda *et al.* as moving along microtubules by taking 8 nm steps [68] through the use of optical tweezers. Since then, the spatial resolution of optical tweezers has improved to a point where it is now possible to resolve the 3.4 Å steps taken by single molecules of RNA polymerase as they move along DNA, from one base pair to the next, transcribing the genetic code [229].

Surprising discoveries that call into question established biological theory have been possible through the adoption of optical tweezers by the life sciences. By using a Köhler illumination arrangement, section 2.2.1, to illuminate the sample with a heating laser, and combining this with optical tweezers and a flow chamber, de Lorenzo *et al.* showed that, contrary to entropic models, the persistence length of single-stranded DNA (ssDNA) appears to increase with temperature [230].

The trend in microscopy based research is, often, to move to smaller and smaller length scales - clearly illustrated by the growing adoption of high resolution microscopy techniques, such as stimulated emission depletion (STED) microscopy and stochastic optical reconstruction microscopy (STORM), for single-molecule based research. However, the importance of cell-scale work cannot be overstated. While optical tweezers have become invaluable for single-molecule work, there has been a growing adoption of their use in single cell research. Although the forces expressed by cells on this scale can often exceed the maximum forces applicable by an optical trap, the high temporal and spatial resolution of optical tweezers have afforded sci-

entists to study the mechanical properties of the cell [96], particle transport by filopodia [231] and the forces present in cell migration [232, 233].

It is well established that chemical and electrical signals can influence the growth, development and function of a cell. Recently, there has been a growing interest on another stimulus that can influence cells: physical force. Notably, force plays a major role in integrin mediated cell adhesion - a process that is necessary for a healthy immune system. This chapter will focus on measuring the forces expressed by primary murine effector T cells and their integrin binding to ligand-coated silica beads. A comparison between the binding strength of cells found in a healthy and unhealthy immune system will be given in section 5.5 to highlight the importance of cell mechanotransduction as a therapeutic target [234–236]. Shear flow has previously been shown to increase activation in effector T cells [237] and adhesion assays under shear flow have been performed [27]. However, the binding force has not been quantitively measured. Therefore, a holographic optical tweezers (HOT) based system is presented in section 5.6, along with a proof of concept experiment, which shows that it would be possible to obtain this greatly desired information using optical trapping techniques.

5.2 Introduction to integrin-ligand binding

An effective immune system relies on the ability of immune cells, collectively termed leukocytes, to travel from one location in the body to another [238]. Their ability to penetrate into tissues and to make contact with other cells depends chiefly on β2 integrins, which are expressed exclusively in leukocytes [239]. β2 integrins mediate many important functions in the immune system, such as cell-cell and cell-extracellular matrix interactions, cell adhesion and signalling in immune cells [239]. Integrins are heterodimeric transmembrane receptors, each composed of non-covalently associated α and β chains [240], which have, very generally, large extracellular domains, single-

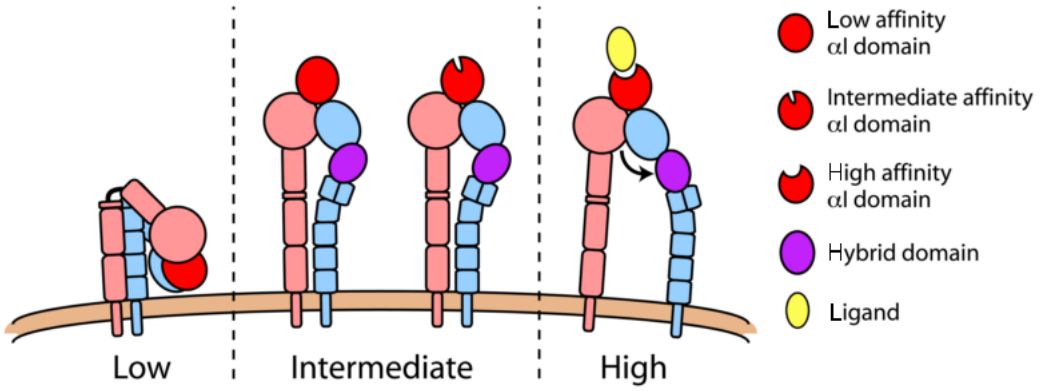

Figure 5.1: LFA-1 structure and conformations. Integrin function is structurally regulated and three distinct confirmations have been demonstrated [241]. Note the single-pass transmembrane segment for each domain (pink: α chain; blue: β chain), the large extracellular domain and short intracellular tail. Image adapted from [241].

pass transmembrane segments and short intracellular tails, figure 5.1 [241]. Activation of integrins by chemokines [242] or mechanical force [243] can cause them to "unfold" - the integrin can undergo a conformational change that increases their affinity for their ligand, figure 5.1 [241]. Additionally, two proteins, talin-1 and kindlin-3, are critical to integrin activation and have distinct roles in the induction of αLβ2 integrin conformational changes, figure 5.2 [241, 244]. The detailed structure and features of the various domains of β2 integrins have been reviewed in great detail elsewhere [245] and are beyond the scope of this introduction.

Of the 24 known integrin heterodimers, leukocytes express at least 12 of them, including four leukocyte specific β2 integrins (αLβ2, αMβ2, αXβ2 and αDβ2) with integrin function and ligand specificity conveyed by the differing α chain [238–240]. The αLβ2 integrin, commonly called lymphocyte function-associated antigen 1 (LFA-1), is the most abundant, and widespread in expression, of the four members of the β2 family [238, 239]. LFA-1 is expressed on all leukocytes and binds to members of the intercellular adhesion molecule

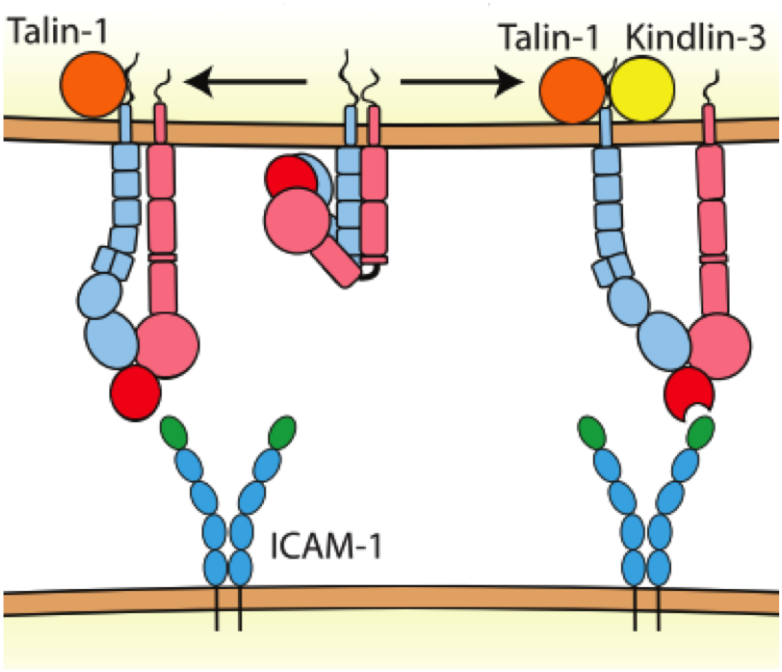

Figure 5.2: β2 integrin in its low affinity state (middle) unfolds to its intermediate state through the binding of talin-1 (left). However, it is not until kindlin-3 also binds to the cytoplasmic domain that the integrin becomes fully activated and moves to its high affinity state (right). Image adapted from [241].

(ICAM) family [239]. This integrin mediates the firm adhesion of leukocytes to the endothelial cells surrounding blood vessels and is necessary for leukocyte extravasation at inflammatory sites [246], without which there would be no "response" from either the innate or adaptive immune system [247]. The adhesion of effector T cells, which play a central role in cell-mediated immunity, to ICAM-1 is completely dependent on β2 integrins [27].

5.2.1 Leukocyte adhesion deficiency (LAD)

β2 integrins are important in the pathologies of several diseases and genetic syndromes, such as Leukocyte Adhesion Deficiency (LAD) [239]. Patients afflicted with LAD suffer from recurrent bacterial infections and, in severe cases, death will occur in early childhood if appropriate therapy, such as bone marrow transplantation, is not administrated [248]. LAD can be divided into three different subtypes, LAD-I-III, depending on the causative mutation [249], with types I and III the most common.

Patients who suffer from LAD-I have mutations which lead to a deficiency or absence of β2 integrin expression [239]. As these integrins are essential for leukocyte function, such as firm adhesion to the endothelium [250] and extravasation at inflammatory sites [246], patients suffer from recurrent bacterial and fungal infections, delayed wound healing and periodontitis [239]. LAD-III, a variant of LAD-I, causes patients to present with similar symptoms to patients with LAD-I but with the added complications of a Glanzmann-type bleeding disorder and, in some cases, osteopetrosis [239]. Mutations in kindlin-3 have been found to be the cause of LAD-III, thus preventing integrins to become fully activated, leading to deficiencies in T cell adhesion and homing [239, 244, 251]. Kindlin-3 and β2 integrin knock out mice, as expected, suffer from similar LAD symptoms, leading to recurrent infections or death, shortly after birth, from severe bleeding [239].

5.2.2 TTT/AAA β2 integrin knock in mouse model

Interaction of kindlin-3 with the β2 integrin in effector T cells is necessary for integrin-mediated adhesion to endothelial cells [244]. Through mutating the TTT motif in the β2 integrin cytoplasmic domain to AAA, Morrison *et al.* were able to generate a knock in (KI) mouse that appeared healthy while having similar neutrophils to those from LAD patients [251]. The term "knock in" in this instance refers to the fact that part of the gene has been selectively replaced by a mutated one, so that all of the protein in the cell is in the mutated form, i.e. the AAA motif has, figuratively, been "knocked in" to the integrin sequence.

Through this mutation, the integrin-kindlin-3 interaction was completely abolished, which resulted in impaired firm adhesion to ICAM-1, figure 5.2. The authors showed that LFA-1 expression, kindlin-3 and β2 integrin protein levels and β2 integrin mRNA levels were similar in WT and KI cells [251]. Essentially, Morrison *et al.* were able to create a mouse line which, for all intents and purposes, have similar biological mutations to patients who suffer from LAD-I and LAD-III, without displaying the same life threatening symptoms.

5.3 Cell and bead preparation

5.3.1 Effector T cell generation

To generate effector T cells, a type of white blood cell whose binding to ICAM-1 is completely dependent on β2 integrins [27], splenocytes were first extracted from either the wild type (WT) or TTT/AAA-β2-integrin knock-in (KI) mice. The spleen was collected and mashed through a $70 - 100$ μl cell strainer with the plunger from a 2 ml syringe and washed with 5 ml of RPMI medium. Cells were centrifuged at 1200 rpm for 5 minutes before being resuspended once the supernatant was discarded. In order to lyse the red

blood cells (RBCs) in the sample, 3 ml of Ammonium-Chloride-Potassium (ACK) lysing buffer was added to the resuspended cells for $2.5 - 3$ minutes. The reaction was stopped by adding 7 ml of RPMI medium to the cells, which were then centrifuged again at 1200 rpm for 5 minutes and the supernatant discarded.

The cells were cultured for 8 days in cell growth medium (RPMI−1640 plus 10% fetal bovine serum (FBS), 1% penicillin streptomycin (pen/strep) and 1% β-mercaptoethanol) and kept in a humidified atmosphere of 5% CO_2/95% air at 37 ºC. For the first 2 days of the culture, the splenocytes were activated with 0.5 μg/ml anti-CD3 (clone 2C11, from R&D Systems) together with 20 ng/ml IL-2 (R&D Systems) and grown in 6 ml of medium. Cells were washed free of the activating agent after 2 days by adding them to 44 ml of medium and centrifuging at 1200 rpm for 5 minutes, followed by discarding the supernatant. Following resuspension, the cells, now T blasts, were then maintained in 10 ml of cell medium plus 20 ng/ml IL-2 and used for experimental purposes on days $6 - 8$ of the culture, once the T blasts had fully differentiated into effector T cells. Throughout the culture, cells were passaged every ~ 2 days, as well as the day before use in an experiment, to $\sim 1 \times 10^6$ cells per ml.

5.3.2 ICAM-1 bead coating

Bonds to the effector T cells were formed by coating 2.56 μm diameter silica beads with 2 μg/ml ICAM-1. Larger diameter beads were found to be trapped with insufficient optical force to overcome the binding force between cell and bead, while smaller diameter beads tended to induce phagocytosis before an adhesion measurement could be made. Coating of the beads was achieved by first washing them, twice, in 1 ml phosphate-buffered saline (P.B.S.). This entails suspending the beads in P.B.S., followed by centrifuging at $13,000$ rpm for 1 minute and collecting the beads.

After washing, the beads were resuspended in 500 μl of P.B.S. with 2

μg/ml ICAM-1 and incubated, on rotation, at 4 ^{o}C for at least 1 hour. Beads were then collected, by centrifuging at 13,000 rpm for 1 minute, and washed three times in P.B.S., as before, to remove any excess ICAM-1 from the solution.

During bead coating, a second sample of uncoated silica beads was prepared by following the same procedures, however without the addition of ICAM-1 before incubation, in order to act as a control sample.

5.4 Experimental system

Initial experiments focussed on measuring the rupture force required to break an integrin-ligand bond under static conditions. In order to do so, a force measuring optical tweezers system, as shown in figure 5.3, was constructed. A 1.5 W (maximum output) 1064 nm diode-pumped solid-state laser (Model Ventus 1064, Laser Quantum) was expanded to overfill the back aperture of a Nikon 1.25 NA 100x oil immersion objective to form the optical trap in the sample plane. The optical trapping beam was imaged, via a Mitutoyo 0.55 NA 100x long working distance objective, onto a quadrant photodiode (QPD). The 2 mm diameter, indium gallium arsenide (InGaAs) QPD was used in back focal plane interferometry (BFPI) mode and was connected to custom built transimpedance amplifiers, which were in turn connected to a National Instruments SCB-68A connector block. Signals were collected via a National Instruments PCI-6250 data acquisition (DAQ) card and analysed using an in-house LabVIEW program.

For adhesion measurements under shear flow conditions, the experimental system prior to the trapping objective was altered and will be discussed in section 5.6.

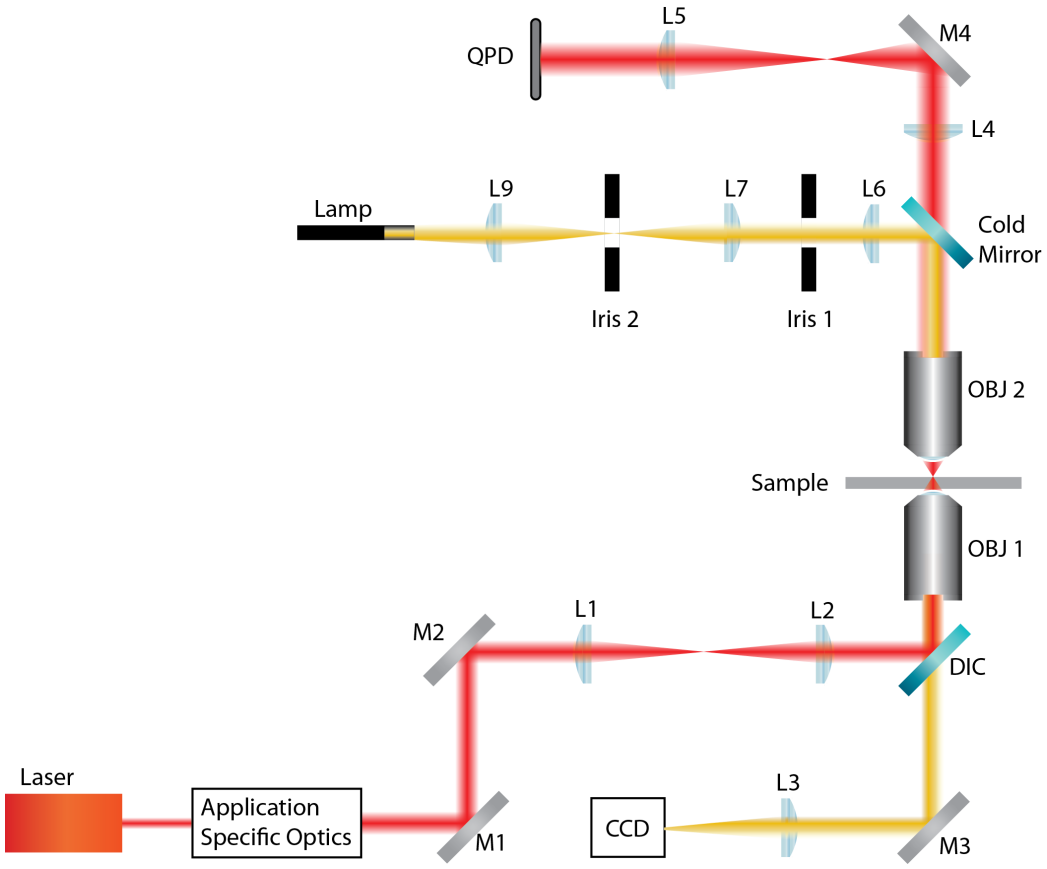

Figure 5.3: Force measuring optical tweezers system used for static adhesion assays. OBJ 1, Nikon 1.25 NA 100x oil immersion objective; OBJ 2, Mitutoyo 0.55 NA 100x long working distance objective; DIC, dichroic mirror; QPD, quadrant photodiode; L#, lens; M#, mirror. Application specific optics, for the static adhesion measurements, refer to expansion and beam steering optics. The sample was placed on a Thorlabs MAX302/M NanoMax piezoelectric stage, which was connected to a Thorlabs MDT630A 3-Axis piezo controller.

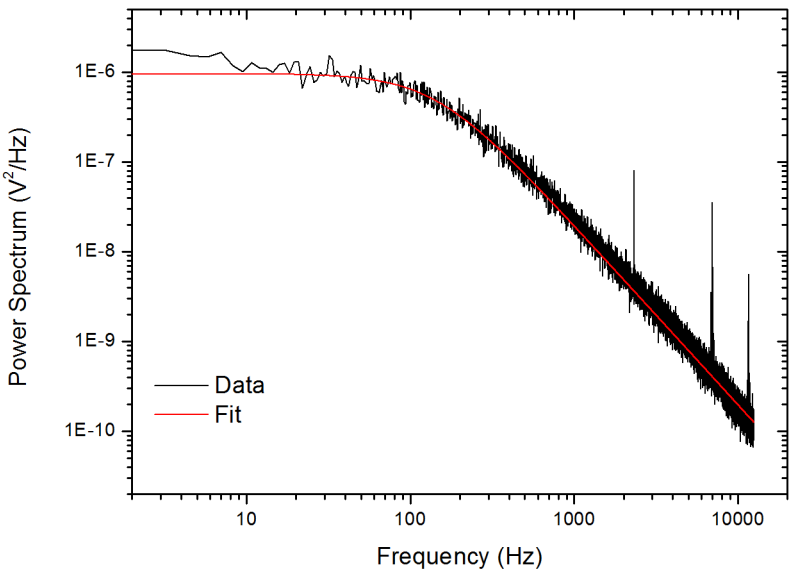

Figure 5.4: Example power spectrum obtained for an optically trapped 2.56 μm, ICAM-1 coated bead. Plot shows both the averaged data, black, and the Lorentzian fit, red. The fitted Lorentzian function gives a corner frequency of ≈ 150 Hz, which corresponds to a trap stiffness of ≈ 22 pN/μm.

Trap stiffness measurement

Before the binding between bead and cell can be measured, the stiffness of the optical trap must first be determined in order to satisfy equation 2.8. Therefore, the first 20 s of each adhesion measurement was used to record the particle position fluctuations, as a function of time, in a stationary trap. Once a silica bead was trapped, the QPD was sampled, in 4 s windows of $400,000$ samples, at a rate of 100 kHz and the x and y position of the bead calculated and saved for post-experimental analysis. Power spectra were calculated from the average signal of five of these windows. Data was fitted between 1 Hz to $10,000$ Hz and the trap stiffness in x and y (k_x and k_y, respectively) determined from the corner frequency, figure 5.4.

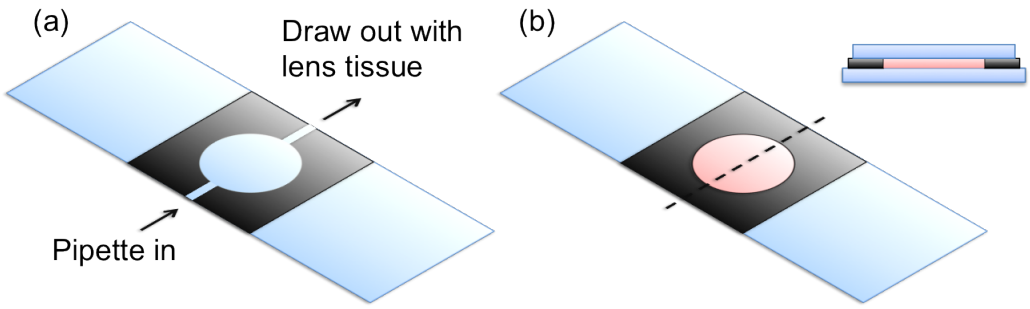

Figure 5.5: (a) Construction of a QPD calibration sample. (b) Illustration of the sample chamber. Inset shows cross section through dashed line. Note, images are not to scale.

Detector calibration

Although trap stiffness can be determined from an uncalibrated detector, the QPD must be calibrated before position measurements can be performed and, therefore, before a force can be calculated. A calibration slide was constructed by first cutting a channel in the vinyl spacer used to construct a trapping sample and then sandwiching this between two microscope cover slips. A sample of 2.56 μm silica beads suspended in a solution of 1 M sodium chloride (NaCl) was pipetted between the two cover slips, figure 5.5(a), and the channel was left in a humid environment overnight to allow the beads to stick to the slide. The salt water was then drawn out from one side of the channel with a piece of lens cleaning tissue, while deionised water was slowly pipetted into the opposite side of the channel.

A single, immobilised, silica bead was scanned back and forth, in a triangular wave fashion, through the centre of the optical trap by the piezoelectric stage, while the QPD signal was monitored. Before calibration data for one axis was recorded, the signal from the other axes was minimised by careful aligning of the bead movement to the axis of interest. Each calibration scan consisted of three passes of the bead through the trap centre and the average of five scans (i.e. fifteen passes of the bead through the trap centre) was taken

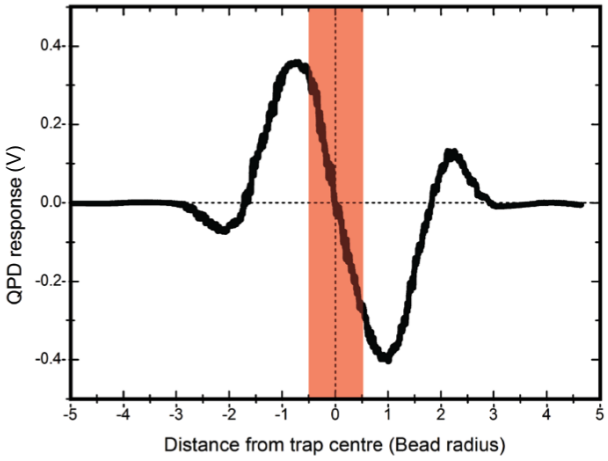

Figure 5.6: Example calibration curve obtained during QPD calibration. The slope of the linear region, shaded red, gives the calibration constant β.

for each axis. Calibration curves, similar to the curve shown in figure 5.6, were calculated in this manner for three different silica beads. From the slope of the linear region in the centre of the curve, the calibration constant, β, can be calculated for both the x and y QPD axis, with an average β calculated from the average of the calibration constants obtained for the three separate beads, giving $\beta_x = (0.31 \pm 0.03)$ V/μm and $\beta_y = (0.28 \pm 0.05)$ V/μm (mean $\pm$ std. error).

5.5 Cell adhesion under static conditions

Samples for the static adhesion force investigation were prepared by mixing 15 μl of cells with 5 μl of silica beads. The mixture was then placed between two type 1 microscope coverslips, separated by a 100 μm vinyl spacer, figure 5.5(b). The cells were left to settle for $15 - 30$ minutes, allowing them to stick to the coverslip, before adhesion experiments began. This was to ensure

that cells did not float away when pushed against the bead, nor jump in to the optical trap when brought close.

5.5.1 Single-beam adhesion program

The binding between cell and bead was measured using a custom written LabVIEW program, which performed an adhesion measurement using a five step process, illustrated in figure 5.7. Before executing the program, a silica bead must be trapped and positioned approx. 10 μm from a cell. The program would then perform a trap stiffness measurement, as outlined above in section 5.4, before moving the piezo-electric stage in order to bring the cell in to contact with the bead. During this "pushing" stage of the program the number of samples of the QPD would decrease to $8,000$ samples to allow the program to monitor the displacement of the bead in pseudo-real time and stop the piezo- stage once the cell and bead were pushed together with a set force. At this point, the piezo- stage would be stopped, the cell and bead would remain in contact for a set adhesion time, and then the cell would be pulled away by the piezo stage, with an average force loading rate on the cell of (30 ± 4) pN/s, and the QPD sample number increased to $800,000$. The QPD would then continue to be monitored by the adhesion program until the piezo- stage returns to its starting position. An integrin-ligand bond is broken when the bead jumps back in to the centre of the trap, producing a similar QPD voltage trace to that of figure 5.8.

5.5.2 Single bond frequency

The number of bonds formed during an adhesion measurement is related to the frequency of successful bonding events, with the number of bonds formed, N_b, following a Poisson distribution [252]. From this statistical distribution, quantitative bond number assessment is possible [4, 23]. It follows that the

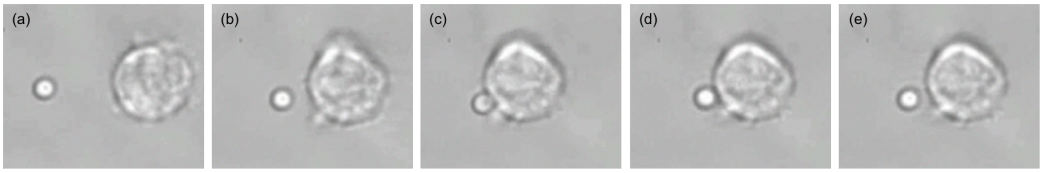

Figure 5.7: The five steps of a static adhesion measurement: (a) trap stiffness - the Brownian motion of the trapped 2.56 μm bead is monitored; (b) approach - the cell is moved towards the bead; (c) stick - the cell is pushed against the side of the bead with a set force for a set time; (d) pull - the cell is pulled away from the trapped bead, with the applied force recorded by the QPD; (e) bond break - the bead jumps back in to the trap once the integrin-ligand bond breaks.

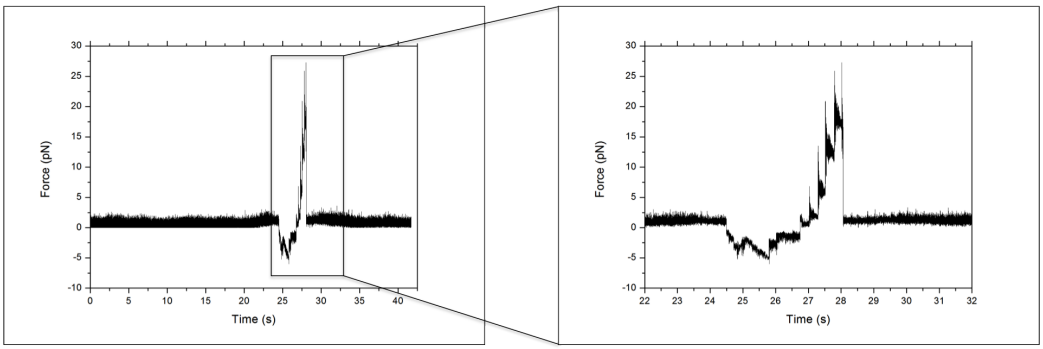

Figure 5.8: Typical force versus time graph obtained for an integrin-ligand unbinding event. The large peak, enlarged in the inset, represents the maximum unbinding force required to disrupt an integrin-ligand bond. The jagged profile of the peak is due to the piezoelectric stage moving in discrete "steps".

probability of forming a given number of bonds is

$$P\left(N_b\right) = \frac{\lambda^{N_b} \exp\left(-\lambda\right)}{N_b!} \tag{5.1}$$

where λ is the mean bond number, $\langle N_b \rangle$. Determination of $\langle N_b \rangle$ is achieved by assuming that any measurement attempt that leads to no adhesive event is representative of $N_b = 0$ [253]. Therefore, $\langle N_b \rangle = -\ln P\left(N_b = 0\right)$, where $P\left(N_b = 0\right)$ is the fraction of adhesion attempts that resulted in no bond formation. Once $\langle N_b \rangle$ is known, the fraction of measurements with a given number of bonds between the cell and bead can be calculated using equation 5.1. A successful binding rate of $< 30\%$ was sought to ensure that the majority of measured adhesion events were single bond formations, in accordance with literature values [30, 253–256]

Three outcomes were possible when performing an adhesion measurement: the bead and cell would not stick together; the bead and cell would remain stuck together; or the bead would jump into the trap, breaking the bond with the cell. A successful measurement of bond strength was achieved when both the video and QPD showed a single, clear break between bead and cell. Successful adhesion events occurred with an average frequency of $\sim 25\%$ for WT cells and $\sim 21\%$ for KI cells. Due to Poisson distribution statistics [4, 23], this is indicative of a single LFA-1 - ICAM-1 bond probability for WT cells of 86.3%, while 12.4% will be double bonds and $\sim 1\%$ will have three or more bonds [22, 253]. The slightly lower average daily success frequency for KI cells gives bond probabilities of 88.7%, 10.5% and $\sim 1\%$ for, respectively, single, double and three or more bonds.

5.5.3 WT vs KI bond strength

Coated and uncoated silica beads were trapped with ~ 200 mW (measured in the sample plane) and the adhesion program was set to exert a force of ~ 5 pN on the cell by the bead, for a time of 1 s.

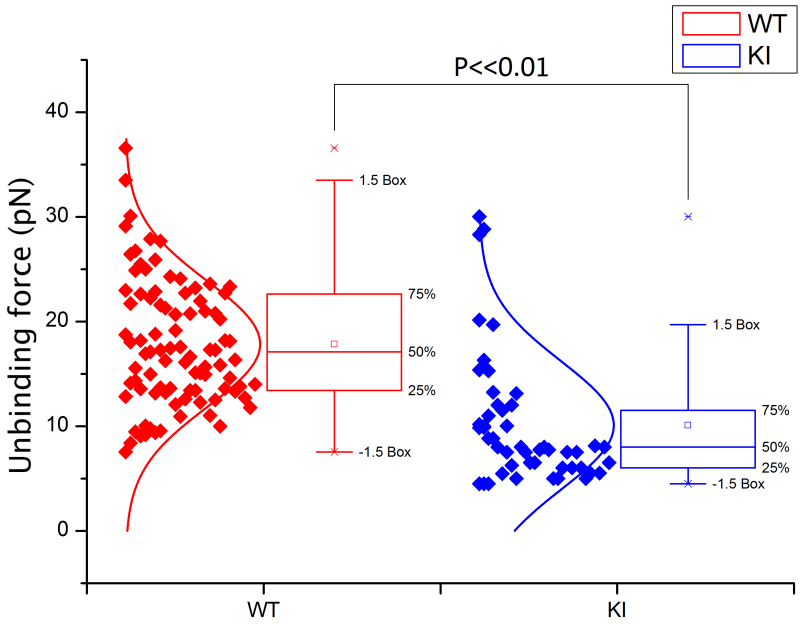

Figure 5.9: Unbinding force of integrin-ligand pairs for both WT and KI cells, as measured by an optically trapped 2.56 μm bead, coated with 2 μg/ml ICAM-1, left in contact with the cell for 1 s. WT adhesion strength was measured as (17.9 ± 0.6) pN, with KI adhesion strength significantly lower at (10.1 ± 0.9) pN. (mean ± std. error, $p \ll 0.01$)

An integrin-ligand unbinding force of (17.9 ± 0.6) pN was measured for WT cells, based on the average force calculated from a total of 91 successful adhesion measurements, figure 5.9. As expected, the unbinding force of the KI was significantly lower ($p \ll 0.01$, calculated using a two-tailed two-sample T test), with an unbinding force of (10.1 ± 0.9) pN calculated from the average of 49 successful adhesion measurements, figure 5.9. In both cases, unbinding force is given as mean ± standard error. No bonds were measured as forming between the uncoated silica beads, which were used as a control.

The cell and bead remaining stuck together could be due to any number

of reasons, such as the bead sticking to filopodia or inducing phagocytosis. The maximum force exerted by the tweezers, however, was higher than the highest force recorded for a successful bond breaking measurement. Thus, it can be hypothesised that when the bead and cell remain stuck together it is due to a different effect, operating in a higher force regime than integrin-ligand binding. Therefore, this data can be discarded when investigating integrin-ligand bond strength.

The data presented in figure 5.9 show that both WT and KI murine effector T cells express LFA-1 and that this integrin can form spontaneous adhesive contacts to ICAM-1, its corresponding ligand. The significant reduction of kindlin3 binding to the integrin achieved through mutation of the TTT motif in the β2 integrin cytoplasmic domain to AAA is mirrored in the reduction of binding strength of the integrin to the ligand. Bond strength for the KI cells is significantly lower than that of the WT cells, thus highlighting the necessity of kindlin3-β2 interaction for the firm adhesion of effector T cells. Previous work by Morrison *et al.* showed that there was not a significant decrease in integrin expression of KI effector T cells when compared to WT effector T cells [251]. Therefore, the significantly decreased adhesion exhibited by the KI cells is not due to reduced integrin surface expression.

Furthermore, Morrison *et al.* showed that, under shear flow, primary murine effector T cells that had TTT/AAA-mutated integrins were able to mediate normal cell rolling on ICAM-1, which is a process that requires integrin-ligand interaction but not firm adhesion [251]. The authors postulated that, although kindlin3 binding to the β2 integrin has been abolished, initial integrin-ligand bonds can still form. This hypothesis appears to be confirmed by the data in figure 5.9: although there has been a significant reduction in integrin-ligand binding strength for KI cells, when compared to WT cells, there is still a noticeable, and measurable, integrin-ligand interaction. This would, therefore, account for for the cell rolling under shear flow which Morrison *et al.* observed [251].

5.6 Cell adhesion under shear flow

Shear flow was introduced into the system by switching the sample slide from two coverslips to an Ibidi $I^{0.4}$ μ-slide, with the QPD recalibrated for this new slide using the procedure outlined in section 5.4. After pipetting 200 μl of cells into the channel, and topping up the entrance well with silica beads, the slide was connected, via silicone tubing, to a 5 ml syringe (BD Plastipak). A neMESYS microfluidic pump was used to flow cell culture medium at 0.04 ml per minute, which corresponds to a shear stress of 0.05 dynes per cm^2 in the channel (N.B., the convention for adhesion based flow assays in the field of immunology is to measure shear stress in the centimetre-gram-second unit of dynes per cm^2, where 1 dyne = 10^{-5} N).

5.6.1 CASBAH: Co-Aligned Single-Beam And Holographic optical trapping systems

To allow for cell adhesion under shear flow to be measured, the experimental system was modified to a dual trap arrangement, utilising co-aligned single-beam and HOT systems (CASBAH), figure 5.10. If shear flow had been introduced to the system outlined in section 5.4, there would be a very high possibility of cells being washed from the surface of the slide. Moving to a holographic based system allowed for both the cell and bead to be trapped under shear flow, thus negating this risk during a measurement. The beam from the 1.5 W (maximum output) 1064 nm diode-pumped solid-state laser (Model Ventus 1064, Laser Quantum) was initially split by the half-wave plate and polarising beam splitting cube (PBS), with the transmitted arm following standard expansion and beam steering optics to form the single-beam optical trap, as described in section 5.4. The reflected arm was used to form the HOT by expanding the beam to slightly overfill a Holoeye PLUTO SLM, designed for use with 1064 nm light. Before entering the final beam steering lens relay system before the trapping objective, both the single-beam

and HOT beams are brought together with half-wave plates and a PBS. This allows both beams to be aligned along a common axis, through the relay system and into the trapping objective, while still remaining separate due to their orthogonal polarisations.

While it has been shown that HOTs can be used to exert and measure forces on biomaterials [257], a liquid crystal SLM does introduce positional and intensity instabilities [258, 259]. Methods have been reported that allow for the calibration of HOTs in order to overcome these instabilities [260], with trap oscillation amplitudes of less than 1 nm (in the sample plane) achievable with analogue-addressed SLMs with a modulation frequency of 480 Hz [259], a result which is comparable to that of non-holographic tweezers. However, by exploiting the orthogonal polarisation of the beams, the HOT beam could be extinguished to allow the QPD to monitor only the single-beam trap. A third half-wave plate and PBS combination was used after the Mitutoyo 0.55 NA 100x long working distance objective to again split the single-beam and HOT beams. Therefore, the force experienced by the stationary trap can be measured, while positional instabilities in the holographic trap will not lead to noise in the power spectrum. Additionally, by utilising such an arrangement, movement of the HOT trap will not lead to a changing QPD signal.

5.6.2 CASBAH adhesion program

Just as with the experimental system, when moving to adhesion measurements under shear flow the adhesion program had to be modified from the form described in section 5.5.1. Although the general functionality of the program and the five step approach to taking a measurement were not changed, the method in which the cell and bead were brought together was adapted for the CASBAH system. Before executing an adhesion measurement, a coated silica bead would be trapped in the single-beam trap and a cell would be trapped in the HOT trap, positioned approx. 10 μm from each

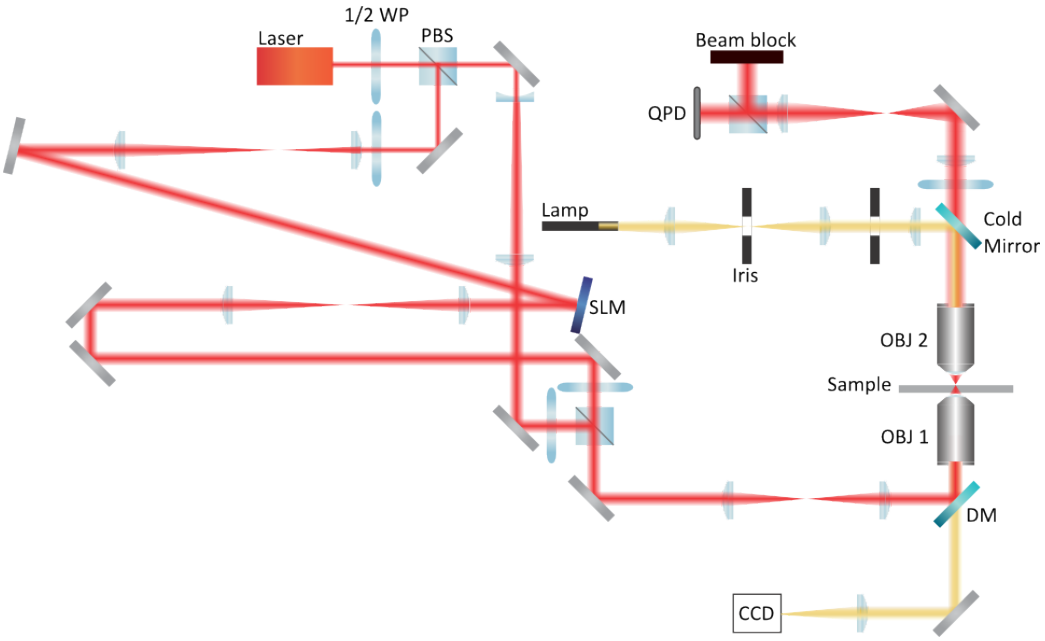

Figure 5.10: Force measuring CASBAH system used for measuring cell adhesion under flow. The reflected beam from the half-wave plate (1/2 WP) and polarising beam splitting cube (PBS) arrangement forms the HOT system using a Holoeye PLUTO phase only SLM, while the transmitted beam forms the single-beam trap. Both systems are combined by half-wave plates and a PBS before entering the core of the tweezers, on the right of the image. A third half-wave plate and PBS combination splits the beam before the QPD, dumping the HOT beam and transmitting the static, single-beam trap.

other. As before, upon starting a measurement, the trap stiffness would first be determined, before the cell and bead are brought together for a set time, with a set force, and then pulled apart. However, for the CASBAH system, the holographic trap containing the cell is brought to the single-beam trap containing the silica bead. A simple gratings and lenses [186] algorithm was used to calculate the kinoforms and update the SLM in real-time. The cell is moved across the flow, rather than with it, to avoid any downstream effects from the cell affecting the particle. Sample rates and times remain unchanged from before, see section 5.5.1 for details.

5.6.3 Binding under shear flow - proof of concept

The single-beam spot was used to optically trap 2 μg/ml ICAM-1 coated 2.56 μm silica beads with 16.1 mW, while WT effector T cells were trapped with 42.0 mW in the HOT spot, both powers were measured in the sample plane. After starting the shear flow, the cell and bead were pushed together with a force of ~ 5 pN for a time of 1 s, before the HOT spot was moved away. As with adhesion measurements under static conditions, three outcomes were possible: cell and bead don't stick, cell and bead remain stuck, cell and bead separate after a binding event. However, the CASBAH system was unable to rupture an integrin-ligand binding event under shear flow conditions. As shown in figure 5.11, if a bond was formed between the cell and coated bead then, upon pulling the cell away, the cell and bead would remain adhered to each other. Therefore, either the cell would jump out of the HOT trap and remain attached to the bead, figure 5.11 (a) - (e), or the bead would jump from the single-beam trap and remain stuck to the cell.

Integrins are generally kept in the inactive state and undergo *in situ* activation from both biochemical and mechanical signals from flow-derived shear forces [237, 243]. Alon and Feigelson have proposed that the actin cytoskeleton may act as a solid support inside the cell for integrins to link to, thus aiding in ICAM-1-induced activation of integrins by shear flow forces

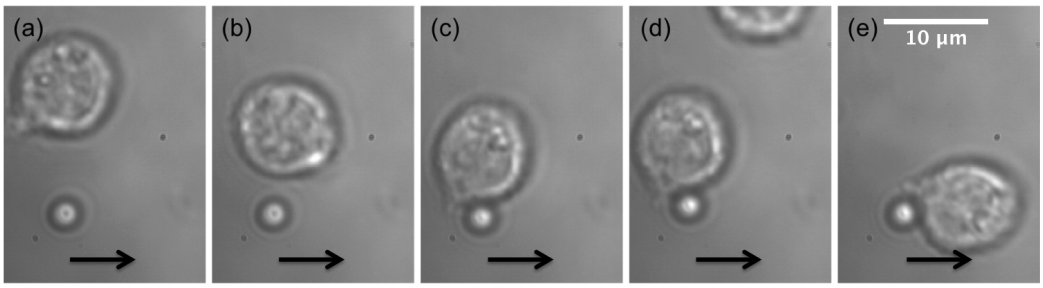

Figure 5.11: CASBAH five step adhesion measurement of integrin-ligand binding under shear flow conditions, flow donated by direction of arrows. (a) - (e) shows binding event under shear flow conditions: (a) trap stiffness; (b) approach; (c) contact; (d) pull; (e) the LFA-1-ICAM-1 bond does not break, the effector T cell jumps out of the HOT trap, remains stuck to the coated bead and is washed behind the bead due to the flow. Not shown: bead jumping out of single-beam trap and remaining stuck to cell.

[242]. Building on this work, Lek *et al.* proposed that further activation of the integrin by shear flow forces, after initial ICAM-1 contacts have formed, is possible due to the mechanical linkage of the integrin to the cytoskeleton, therefore allowing for a strong adhesion between integrin and ligand [27]. Additionally, effector T cells that have bound to ICAM-1 under shear flow will reorganise their actin cytoskeleton and spread out on the ligand, a shape change that likely aids their resistance to shear flow forces [27]. Therefore, it is conceivable that LFA-1 binding to ICAM-1 has been sufficiently increased through the application of shear flow that the CASBAH system is unable to rupture the bond.

In order to test this hypothesis, the strength of LFA-1 adhesion to ICAM-1 was probed under static conditions using the CASBAH system. Cell-bead samples were prepared in a similar manner to the static adhesion experiments, section 5.5, and the CASBAH system recalibrated to account for the new sample slide. Trapping and force parameters remained unchanged (i.e. bead trapped with 16.1 mW, WT effector T cells trapped with 42.0 mW), as did the adhesion measuring procedure. Unfortunately, the CASBAH system

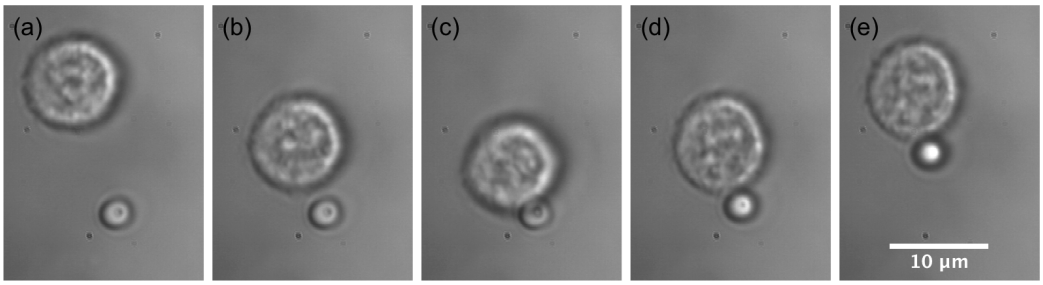

Figure 5.12: Integrin-ligand binding measurement under static conditions using the CASBAH system. (a) - (e) shows binding event with no shear flow: (a) trap stiffness; (b) approach; (c) contact; (d) pull; (e) cell and bead remain bonded together. However, this time the bead jumps from the single-beam trap to remain stuck to the effector T cell trapped in the HOT trap. Not shown: cell jumping from the HOT trap to remain stuck to the bead.

was unable to rupture bonds between cell and bead under static conditions. As with adhesion under shear flow, either the cell or bead would jump out of their respective traps and remain stuck to each other, figure 5.12.

Optical tweezers that incorporate SLMs are infamous in the field of optical trapping as being very optically inefficient. While there has been a large amount of work performed in an effort to combat this [155, 191, 261–263], the CASBAH system does not capitalise on these solutions. Due to the inability of the CASBAH system to rupture even a single integrin-ligand bond under static conditions, when bond strength should be lower than that of binding under shear flow, it is clear that the system has been significantly weakened by moving to a holographic-based solution and utilising an SLM with a reflectivity of 62% and diffraction efficiency of 80%, as stated by the manufacturer. This is further highlighted by the alarming reduction in optical power in the trapping plane of the CASBAH system in comparison to the single-beam system in section 5.4. For example, the maximum measured trap stiffness for the 2.56 µm silica bead when using the CASBAH system was $\sim$ 5.6 pN/µm. Additionally, at times, forces as low as $\sim$ 1 pN were all that was required to pull the cell from the holographic trap, which can be

attributed to the reduction in optical power in the trapping plane and large size of the cell, leading to lower achievable trap stiffnesses for the cell than for a trapped bead. However, figures 5.11 and 5.12 clearly show that it is possible to form bonds between cell and bead under shear flow and, through improvements in efficiency, the strength of these bonds could be determined, under shear flow, by using the CASBAH system.

5.6.4 The future of CASBAH

Although the CASBAH system was unable to measure the binding force between LFA-1 and ICAM-1, section 5.6.3 clearly shows that such measurements should be possible through simple improvements to the system. These improvements can be as simple as increasing trap stiffness by using a more powerful laser source or increasing the NA of the trapping objective. Indeed, preliminary results using a Nikon CFI Plan Apo Lambda 1.45 NA 100x oil immersion objective as the trapping objective on the single-beam system indicate that the trap power can be approximately halved and still achieve cell-bead detachment.

As previously mentioned, section 5.6.3, the optical efficiency of SLMs is low, leading to a low throughput efficiency of the optical system. By replacing the SLM with galvanometer mirrors [17, 158] or electrooptic deflectors (EOD) [17, 131], optical throughput of the system can be significantly improved. However EOD's come at a high cost and offer a limited deflection angle [17, 131], while galvanometer mirrors may require feedback stabilisation to account for the wobble and jitter of the trap caused by the mirror's mechanical nature [17, 131].

Before purchasing additional components and replacing the SLM in the CASBAH system, efficiency gains could be obtained by focussing on the diffraction efficiency of the holograms used to generate the HOT spot. By moving away from the simple gratings and lenses [186] algorithm to more sophisticated, non-iterative methods of hologram generation, such as ran-

dom mask encoding of Fourier components [221] more optical power could be diffracted into the trapping spots. Additionally, by combining wavefront correction techniques [191], aberrations in the optical train can be compensated for, thus trap stiffness can be increased by generating an optimally focussed trapping spot.

Increasing hologram diffraction efficiency has the added advantage of allowing for more complex trapping geometries to be exploited by the system. Rather than trapping the cell in a single holographically created trap, it would be advantageous to trap the effector T cell with three individual spots arranged in a triangular fashion, figure 5.13. By moving to a three spot geometry, the cell "trap" can be made much stiffer as it becomes equivalent to trapping the cell "as a whole", much like a silica bead, rather than forming a trap within the cell [264]. Cell roll, or re-orientation, can also be minimised by utilising this three trap geometry, allowing for accurate position tracking of the cell to be implemented, if desired in the future [264]. The main advantage, however, of employing three traps is that cells can be trapped for much longer, or with higher powers, without significant reduction in cell viability [265]. For example, in a single-beam trap, a T cell will begin to die after about 20 minutes, when trapped with 180 mW of 1064 nm trapping light [265]. However, this time increases to over 30 minutes when the same power is split between three traps [265], giving not only a more stiffly trapped cell but also a healthier cell.

The aforementioned suggestions focus on improving the CASBAH system, either the equipment itself or the holographically generated trapping spot. Until recently, the main focus for generating higher trapping forces has been to improve the trapping system or to shape the beam in some fashion [266]. However, over the past five years, there has been a growing interest in looking at the problem from the other side of the coin - using the trapped object itself to help generate higher trapping forces [266, 267]. The forces required to break the integrin-ligand bond could be achieved by replacing the silica bead

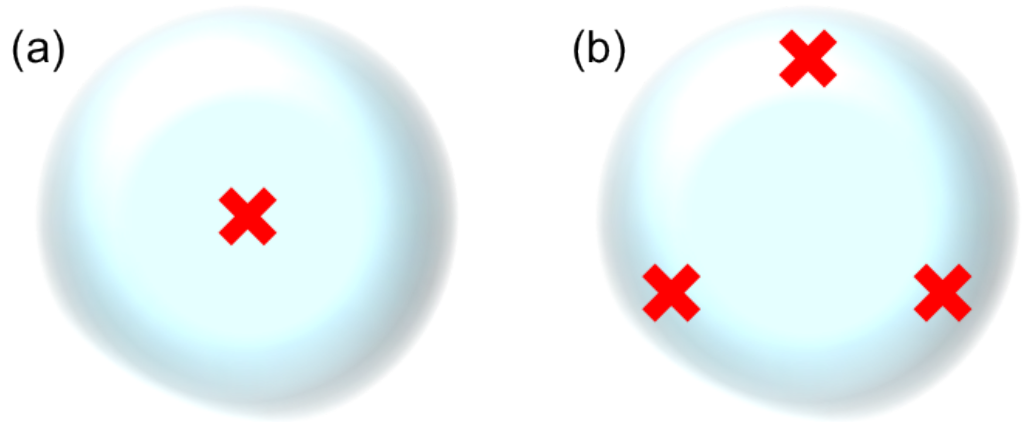

Figure 5.13: (a) Cell trapped with single Gaussian beam - cell rolls and viability decreases quickly. (b) Cell trapped with three SLM created Gaussian traps - minimises cell roll and increases trapped cell lifetime [264, 265].

with an anti-reflection coated, high-refractive-index titania microsphere [267]. Such beads have been shown to generate nanonewton optical trapping forces at high trapping powers (1.4 W), while also generating similar, piconewton-regime, forces as silica beads but at significantly lower trap power [267]. Furthermore, coating the titania microspheres in a thin layer of silica did not negatively influence the trapping performance [267], therefore coating the beads in ICAM-1 should be possible and the beads should be biologically compatible [268, 269]. Thus, it is possible that integrin-ligand bonds could form between the titania microspheres and effector T cells, with enough optical force generated from the titania microspheres, at the low trapping powers currently found in the CASBAH system, to then rupture these bonds.

5.7 Conclusion

Through the use of interferometric particle tracking and power spectrum analysis, the binding strength between the ICAM-1 ligand and the β2 integrin LFA-1, naturally expressed on primary murine effector T cells, has

been quantified. Loss of β2 integrin expression or function is associated with genetic syndrome Leukocyte Adhesion Deficiency (LAD) [239]. Morrison *et al* showed that there was no significant reduction in integrin expression of effector T cells from TTT/AAA-β2-integrin knock-in (KI) mice [251], however the mice, while appearing healthy, have neutrophils similar to those from LAD patients. Effector T cells from healthy, wild type (WT) mice were found to adhere to 2.56 μm silica beads, coated with 2 μg/ml ICAM-1, with a force of (17.9 ± 0.6) pN, under static conditions. This binding strength dropped to (10.1 ± 0.9) pN when effector T cells from KI mice were probed, thus highlighting the importance of cell mechanotransduction as a therapeutic target [234–236].

Activation in effector T cells has been shown to increase under shear flow conditions [237,243], with binding strength of effector T cells to ICAM-1 proposed to also increase [27,242]. Although qualitatively shown, the binding increase has not been quantitively measured. In an effort to do so, a Co-Aligned Single-Beam And Holographic optical tweezer (CASBAH) system was constructed, thus allowing for both the cell and bead to be trapped, brought together and pulled apart under shear flow conditions. Unfortunately, by moving to a holographic-based approach, the adhesion measurement system was significantly weakened and was unable to rupture any LFA-1-ICAM-1 bonds. However, it was shown that these bonds can form between optically trapped cells and beads, under shear flow conditions, in the CASBAH system. Therefore, a proof of concept has been provided, which shows that such measurements would be possible if the forces in the system are increased. By using a more powerful laser source, or employing anti-reflection coated, high-refractive-index titania microspheres [267] to generate large trapping forces, it should be possible to rupture the integrin-ligand bonds formed under shear flow conditions in the CASBAH system, thus allowing for the acquisition of this greatly desired information.

Chapter 6

Low-cost Optical Manipulation using Polymer Lenses and Bubble Wrap

6.1 Low-cost solutions for high-tech problems

The world is far more complex than science can currently grasp. Slowly, but surely, however, complicated problems are being solved by more and more complex techniques. Light microscopes, which have become ubiquitous in modern research laboratories, are often combined with optical tweezers to produce high-end systems that are capable of providing insight into the physical, chemical and biological processes occurring in aerosols [270], liquids [271] and single molecules [68]. Quantitative measurements of biomarkers have helped tackle cancer and disease, while assays have been developed that probe the safety of food and water. Indeed, the previous chapter showed how optical tweezers can be used as a quantitative tool capable of making single molecule force measurements. These sophisticated systems, however, come with an associated high cost, thus limiting their use in not only pedagogical settings but also in research labs throughout the world. Notably, populations

in developing countries, where the need for such tools can often be of greatest importance, often do not have access to the required resources.

In response to this, there has been a large push within the scientific community to develop low-cost alternatives through repurposing materials that are already designed and produced in large quantities, at a low cost. This "adaptive use" has led to the development of paper based microfluidics [272–276] and the use of an egg beater as a centrifuge [277]. Wearable body sensors have been created by fusing graphene, prepared by a kitchen blender [278], with rubber bands [279]. Furthermore, the high-quality digital camera found on mobile phones has been exploited to create low-cost, miniature microscopes and dermascopes [280–284] .

Following in a similar manner of repurposing common materials, a low-cost and low-tech method of fabricating an optical micromanipulation system is presented in this chapter. Through the adaptive use of equipment that is often found, discarded, in the laboratory, the trapping and imaging lens can be fabricated from polydimethylsiloxane (PDMS) and coupled to a smartphone for imaging. During fabrication, the imaging lens is doped with Sudan II dye, prior to moulding, to produce a long pass filter with negligible autofluorescence [285]. By integrating the imaging lens and long pass filter, a more compact system can be created while still effectively filtering the 532 nm trapping light, thus preventing saturation of the smartphone camera. Illumination was provided by shining a lamp into polystyrene foam packaging, perpendicular to the imaging path, producing a diffuse light source that was sufficient for resolving silica beads [286].

Chapter 5 highlighted the power of optical tweezers as a tool in the life sciences. Presented here is a low-cost extension of optical tweezers into this field, achieved through the adaptive use of bubble wrap [287]. It was found that the flat side of bubble wrap is of sufficient optical quality that the bubbles can be used as an optical trapping chamber. The sterile, and gas permeable, bubbles allowed for primary murine effector T cells to be cultured

in the bubbles for over a week, before being trapped, in the bubbles, by the PDMS droplet lenses. This further reduces the cost of our optical manipulation system making it beneficial in resource-limited regions. Furthermore, it allows for direct cell culturing in the trapping chamber: convention would be to culture in a vessel away from the trapping chamber and then transfer the cells. A bubble wrap based system removes this extra step which may damage cells, and may facilitate the handling of pathogens in a more straightforward manner. Additionally, it enables the simple study of cell-cell interactions during cell growth. However, it should be noted, that bubble wrap should not be considered as a replacement to lab equipment, merely an alternative in certain situations. For example, large scale cultures would prove to be time consuming as the volume of individual bubbles is significantly lower than large cell culture flasks, so many bubbles would have to be seeded with cells as opposed to one flask.

At all stages of fabrication of the system, methods which make use of materials that are often found discarded or over looked in the lab, or are easily obtainable for a low cost, are presented. Neglecting the cost of a laser, which could be replaced by a laser pointer, or other low cost alternative, the optical manipulation system can be constructed for approximately £23.23, with a full cost breakdown of all components required also given. Measurements of the trapping ability and efficiency of a droplet lens based optical tweezers system are given.

6.1.1 Repurposing materials

Adaptive use of bubble wrap

Reagents and samples for analysis tend to be stored in solid containers (cell culture flasks, multi-well plates, etc), which are convenient in well-funded laboratories but are of little use in resource-limited settings. These containers can be expensive and therefore unaffordable; difficult to sterilise and dispose

of; and brittle, thus capable of generating "sharps". It was demonstrated by Whitesides *et al.* that bubble wrap can be repurposed as containers to store liquid samples, to act as electrochemical cells, and used to perform bioanalysis and culture bacteria [288]. As bubble wrap is very inexpensive and readily available throughout the world, it is a very attractive material for repurposing. It is very flexible, easily disposed of by burning and can be easily cut to size without generating "sharps". Furthermore, a sterile environment is found inside the bubbles, which themselves are formed by a gas permeable plastic, allowing for the culture and storage of cells and bacteria [287, 288].

Elastomeric optics

A low-cost, high quality, alternative to many optical components was introduced through the development of elastomeric optics using polydimethylsiloxane (PDMS) [289]. The high refractive index ($n = 1.47 - 1.55$) and high transparency ($> 95\%$), within the visible wavelength range, of PDMS makes it an ideal material to fashion lenses from. PDMS is easy to work with in the lab due to its low moulding temperature ($< 100°C$) negating the need for specialised, high-temperature equipment [289]. An increasing number of novel applications, such as biologically inspired wide field lenses [290], a rubber microscope [291] and anti-reflection shielding on LEDs [292]. Additionally, hanging droplets of PDMS can be used to form lenses and have been coupled to mobile phones in the fabrication of a low-cost dermascope [284] and low-cost optical tweezers [286, 287].

6.2 Materials and methods

6.2.1 Cell culture in bubble wrap

In order to generate effector T cells, splenocytes from wild type mice were activated for 2 days with 0.5 μg/mL anti-CD3 (clone 2C11, R&D Systems)

together with 20 ng/mL IL-2 (R&D Systems). The bubble wrap was quickly cleaned with a spray of 70% ethanol/30% water before a 1 mL syringe (BD Plastipak), with attached 26 G 23 needle (Terumo Neolus), was used to inject cells into bubble wrap with 1 cm diameter bubbles. Clear nail polish (obtained from local pharmacist) was used to seal the puncture in order to maintain the sterile environment inside the bubbles. Due to the differing volume of air in each bubble, cells were injected until the pressure in the bubble rounded out the shape of the plastic, approx. $200 - 300$ µl.

After 2 days, cells were removed from the bubble wrap, washed free of the activating agent and then maintained in 20 ng/mL IL-2 for 6 more days. Throughout the culture, cells were passaged every 2 days to approx. 1×10^6 cells per ml. Cells were injected into a different bubble, and the puncture sealed with clear nail polish, each time they were split.

In order to verify the sterility of the bubble wrap, sterile growth medium was injected into bubbles as a control experiment. Both the cell containing bubble wrap and the control bubble wrap were incubated at 37 °C with 5% CO_2 throughout the culture duration.

6.2.2 Making trapping lens and curing with lamp

Small objects can be magnified with liquid droplets [293, 294]. When the interfacial energies (liquid, air and solid surface) attain equilibrium with gravity, a hanging droplet is formed [293, 295]. Indeed, it is precisely this natural curvature that tuneable liquid lenses try to harness, through the application of electrical [296], thermal [297] or mechanical force [298], for fast, single lens, focussing. Through the repeated layering and curing of hanging droplets of PDMS, Lee *et al.* formed low-cost elastomer lenses that were able to resolve structures as small as 4 µm [284]. These lenses were then shown to be suitable as the basis of low cost optical manipulation [286], making use of such lenses for the microscope objective and the condenser lens.

The trapping lens was formed from hanging droplets of PDMS, which had been prepared using the typical soft lithography PDMS procedure, and followed similar steps to those outlined by Lee *et al.* [284], shown in figures 6.1 (a) - (c). That is to say, PDMS monomer and hardener were mixed at a ratio of 10 : 1 v/v (Sylgard 184 Silicone Elastomer kit, Dow Corning) and then placed in a vacuum desiccator until all bubbles were removed. A 1 mL syringe was carefully filled with PDMS and pressure applied until a single drop (< 100 µL) fell onto a microscope coverslip, thickness no. 1. The coverslip was immediately inverted and suspended, ≈ 20 mm, above a sheet of tin foil on the lab bench. Any excess PDMS falls from the slide until single drips are formed.

Heat for the curing step was provided by lowering a 100 W incandescent light bulb, in an anglepoise lamp, to ≈ 20 mm above the coverslip, with heat reflected back towards the droplet lens from the tin foil. Temperature was crudely controlled by raising and lowering the light bulb, with temperatures in excess of 100 °C easily reached. Droplet lenses were left in the "oven" to cure for up to 15 minutes, with temperatures maintained between $70 - 80\,^{\circ}\mathrm{C}$. In order to increase the numerical aperture (NA) of the lens, and decrease the focal length, up to four droplets were layered one on top of the other, with each droplet cured in an inverted fashion before the next was applied. Due to the maximum surface tension that the droplet can hold before falling, the eventual droplet shape at the apex of the lens resembles that of a parabola, with a curvature that increases with layer number. The finished lens on coverslip, figure 6.1(d), cost approximately £0.06, assuming that the purchase of tin foil and a lightbulb is not required [286].

Droplet lens length (L) was found to vary, with measured values typically ranging between (7.38 ± 0.15) mm and (8.48 ± 0.19) mm. However, it was found that the back aperture (BA) and diameter of the entrance pupil (D) remained roughly constant, with average values of, respectively, (6.1 ± 0.2) mm and (2.6 ± 0.3) mm. This led to a slight variation in focal length, with

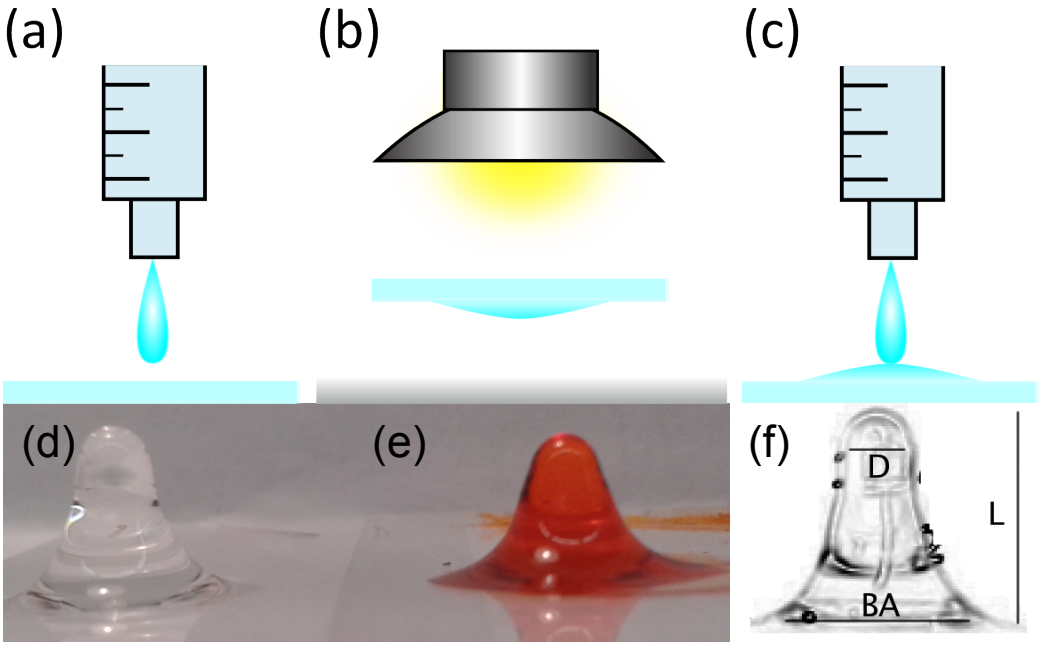

Figure 6.1: Steps used to fabricate a droplet lens: (a) droplet of PDMS deposited on microscope coverslip from syringe; (b) 100 W incandescent bulb used to cure inverted PDMS droplet, suspended above tin foil; (c) additional droplet of PDMS layered on top of cured droplet. Steps (b) and (c) are repeated to increase droplet curvature. Four invert and cure steps were preformed for the lenses presented here. (d) and (e) show, respectively, the fabricated lenses used for trapping and imaging, with a schematic of how lenses were measured shown in (f).

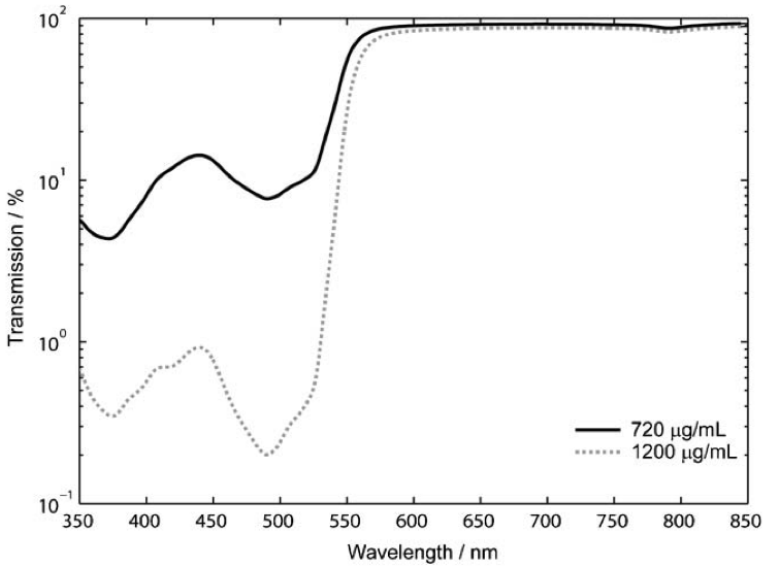

Figure 6.2: Transmission spectrum of PDMS doped with Sudan II dye. Image reproduced from [300].

used trapping lenses having focal lengths of (0.9 ± 0.2) mm and (1.0 ± 0.3) mm. The effective NA of these lenses was estimated as 0.70 ± 0.17 and 0.68 ± 0.18 [286].

6.2.3 Making imaging lens and combining with phone

With the unprecedented growth of the mobile phone market, high-quality digital cameras are readily and widely available and much recent work in the lab on a chip field makes use of smartphone sensing capabilities [299]. Thus, a mobile phone camera was chosen to image the trapped beads. Integration of the imaging lens with a long pass filter allowed for a more compact system, while still effectively blocking the 532 nm trapping light, preventing saturation of the camera [286]. The transmission curve of PDMS doped with Sudan II dye is shown in figure 6.2 [285, 300].

This was achieved by doping the PDMS mixture with 1400 $\mu g/mL^{-1}$ Sudan II dye prior to moulding. 14 mg of Sudan II dye (Sigma-Aldrich)

was first dissolved in ≈ 1 mL of toluene and then added to premixed PDMS monomer and hardener, ratio of 10 : 1 v/v, to give a dye-loading of 1400 $\mu g/mL^{-1}$ [285]. Manual mixing was continued until a uniform PDMS colour was observed. The coloured PDMS was then used to fabricate a hanging droplet lens, figure 6.1(e), using the steps outlined in section 6.2.2 , at an increased cost of £0.08 per lens [286].

6.2.4 Illumination and optical tweezers setup assembly

The low-cost experimental system used, shown in figure 6.3, made use of a 1.5 W (maximum output) 532 nm solid-state laser (Model: Ventus, Laser Quantum) as the trapping source. In order to keep the system as simple as possible, no expansion optics were used before the droplet lens. A 50 : 50 beam splitter (ESB1, Thorlabs, £23.08) reflected the trapping beam up to the clear PDMS droplet lens, while transmitting the white light illumination. As it was necessary to place the mobile phone in direct contact with the imaging lens, transmission microscopy, where the sample is imaged from above and illuminated below, was used [286].

Illumination of the sample was achieved by shining a lamp into polystyrene foam packaging, perpendicular to the imaging path, figure 6.3, thus producing a diffuse light source, which was sufficient to illuminate the sample without saturating the camera. The images presented in section 6.3 were taken with a Thorlabs OSL1-EC fibre illuminator as it was convenient. However, illumination can be provided from any sufficiently bright lamp, with torches, bike lamps and camera flash from a mobile phone all successfully tested. Stray laser light was found to be reflecting from the foam packaging and illuminating the sample with scattered laser light, thus reducing image contrast. To counteract this, a single droplet of coloured PDMS on a microscope coverslip was cured in a non-inverted geometry, to make a PDMS filter. The droplet filter was placed in the illumination pathway, preventing the scatter from degrading the image quality.

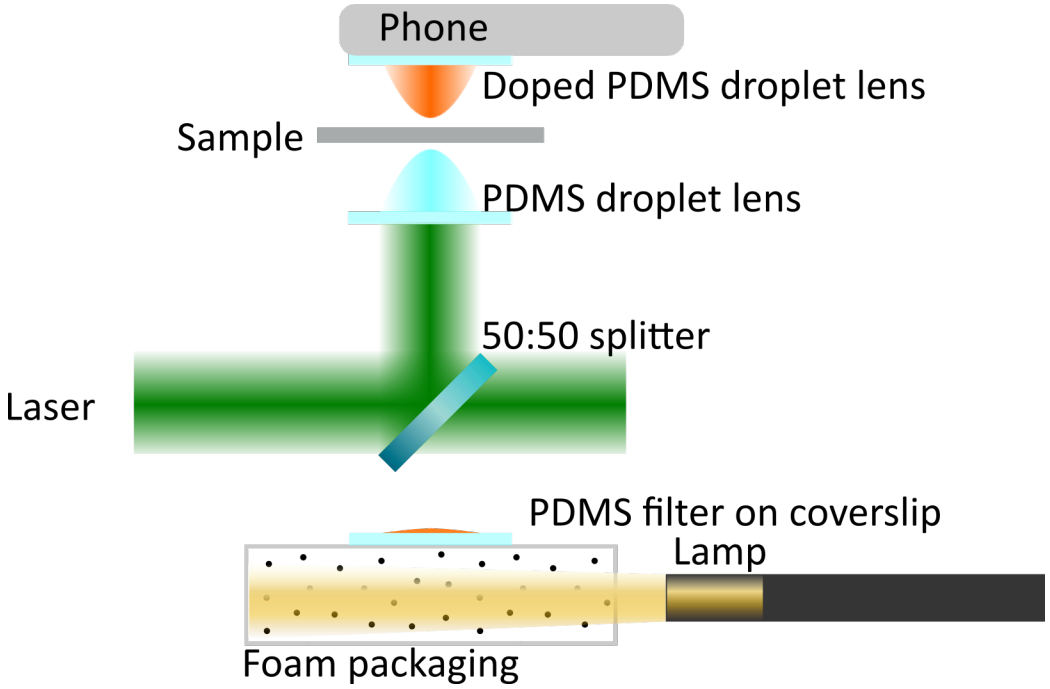

Figure 6.3: Experimental system used for low-cost optical tweezers based on hanging droplets of PDMS.

It should be noted that the use of a high quality laser as used here suggests that this is not a particularly low cost system. However, as reported in section 6.3.3, trapping with $\approx$ 34 mW [286] is possible, with more recent developments pushing this minimum to as low as 20 mW. This puts the system well within the range of a high power laser pointer or equivalent low cost laser diode.

6.3 Results and discussion

6.3.1 Trapping in bubble wrap

Initial experiments for trapping in bubble wrap were performed on a standard set of optical tweezers, in order to test the optical quality of the flat side of the bubble wrap. A 1.5 W (maximum output) 1064 nm solid-state laser (Model: Ventus, Laser Quantum), after going through the standard expansion and relay optics, was focussed by a Nikon 1.25 NA 100x oil immersion microscope objective, in a standard inverted microscope fashion, to form the optical trap.

Various sizes of silica beads (1.01 μm $-$ 5.2 μm) were trapped inside the bubble wrap, figure 6.4(a), which was placed in direct contact with the objective, with no noticeable loss in trapping performance. However, due to the surface tension of the immersion oil, the flexible bubble wrap would be pulled down and sag across the sample holder. This could be avoided by either placing the bubble wrap on a coverslip or pulling the bubble wrap taut and fixing it to the sample holder with tape, before it came in contact with the oil [287].

6.3.2 Trapping cells in bubble wrap

No bacterial growth was observed in the control bubbles of sterile growth medium after 8 days of culturing in bubble wrap, thus confirming the results of Whitesides *et al.* that the interior of the bubbles is sterile [288]. Bubbles

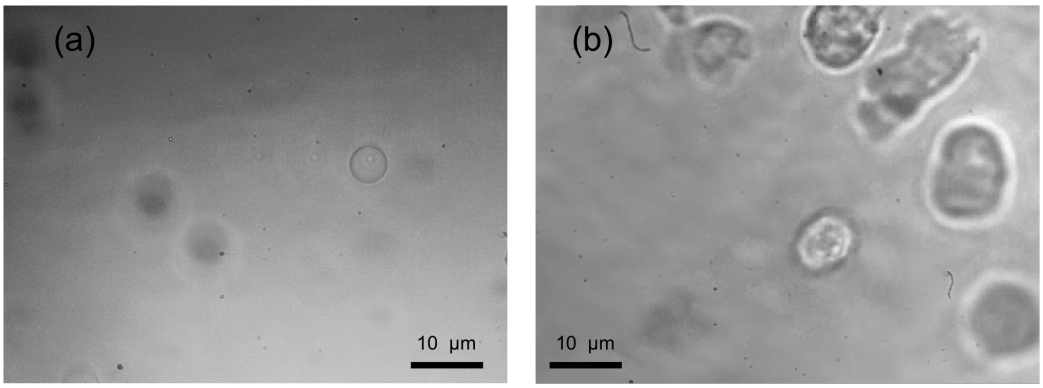

Figure 6.4: (a) Optically trapped (in focus) and untrapped (out of focus) 5.2 μm silica beads in bubble wrap. (b) Optically trapped cell (in focus) in bubble wrap, sitting among untrapped, and therefore out of focus, cells. In both (a) and (b) the object is trapped with a Nikon 1.25 NA oil immersion microscope objective on a standard set of optical tweezers (outlined in section 6.3.1).

that contained effector T cells showed growth and division of cells, proving that it was not a lack of oxygen diffusion that prevented bacterial growth in the bubbles.

Using the system outlined in section 6.3.1, and ensuring that the same precautions were followed, i.e. pulling the bubble wrap taut or placing on a microscope coverslip, optical trapping of cells in bubble wrap was possible. Thus, bubble wrap can be used to not only store and culture cells, due to the sterility and gas permeability of bubble wrap, but can also find use as optical trapping chambers [287]. Figure 6.4(b) shows an in focus, optically trapped cell among untrapped, and therefore out of focus, cells in bubble wrap. Straightforward integration with optical tweezers systems, for analysis of bacterial or cellular growth, is therefore possible.

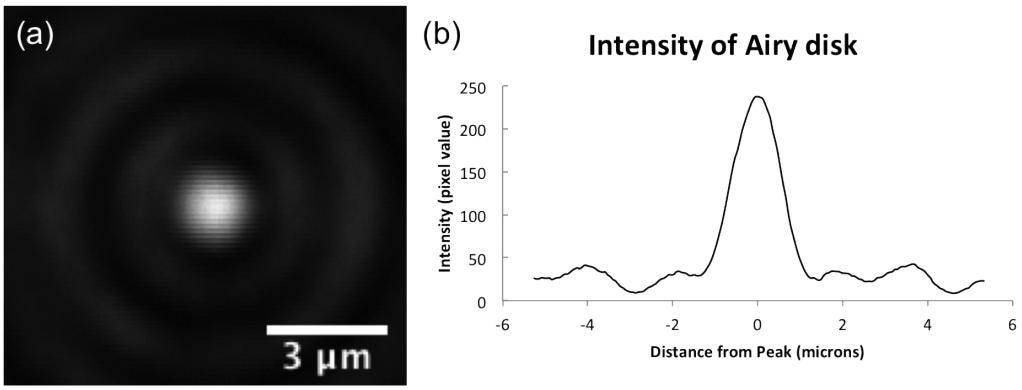

Figure 6.5: (a) Experimental Airy disk produced by a PDMS droplet lens, imaged with a Mitutoyo 0.55 NA 100x long working distance objective. (b) Line profile through the centre of the Airy disk.

6.3.3 Trapping with drip lens

To ensure a focal spot of sufficient quality to trap was produced by the droplet lens, a Mitutoyo 0.55 NA 100x long working distance objective was used to image the focal spot on to a CCD camera. The experimental Airy disk obtained from a trapping lens is shown in figure 6.5, and corresponds to an Airy disk that is approximately 6 times the width of the theoretically obtainable diffraction limit calculated by equation 2.7. The focal length of the lens was measured as (0.9 ± 0.2) mm, giving an estimated effective NA of 0.70 ± 0.17.

The trapping sample consisted of a suspension of 3.93 µm diameter silica beads in deionised water, between two microscope coverslips separated by a vinyl spacer. Particle size was chosen as previous studies [284] have shown the smallest resolvable structure with the droplet lens to be 4 µm. Shown in figure 6.6 is a 3.93 µm silica bead, which has been trapped with a clear PDMS droplet lens and imaged with the Mitutoyo objective mentioned above. Particle height was observed to change with trap power, indicating two dimensional trapping, i.e. optical levitation. The minimum power to trap was found to be (34.0 ± 0.4) mW in the trapping spot, however, recent work has

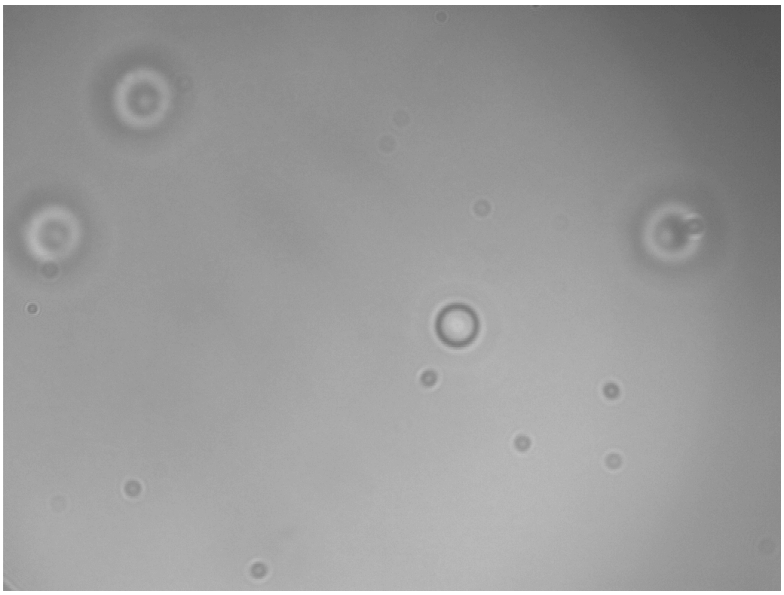

Figure 6.6: Using a clear PDMS droplet lens, an optically trapped 3.93 μm silica bead (in focus) sits among untrapped, therefore out of focus, beads. Imaged with a Mitutoyo 0.55 NA 100x long working distance objective.

shown that this power can be further reduced to a minimum of 20 mW.

To examine the ability of the droplet based tweezers to function as a more robust research grade instrument, a simple measure of the transverse Q value [86] of the trapping spot was made. Through the use of the Stokes' drag technique, outlined in section 2.3.2, and equations 2.3 and 2.12, trapping efficiency can be determined. The 3.93 μm beads were trapped with (54.48 ± 0.08) mW of laser power and a Q value of 0.0089 ± 0.0001 was measured.

Quantitative measurements, or measurements that require high optical forces, may not be suitable with a low-cost optical tweezers based on droplet lenses, as indicated by the low Q value. However, trial experiments and qualitative measurements could be easily performed.

6.3.4 Trapping with drip lens in bubble wrap

Optical tweezers are highly attractive to the biophysical sciences, therefore it is imperative to the design of a low-cost system that the droplet lens based tweezers can trap in bubble wrap. The trapping sample was injected into the bubble wrap and placed above a droplet lens of (0.9 ± 0.2) mm. When trapping cells, it was necessary to prepare the sample first by moving the cells from the bubble in which they had been cultured to a new bubble in the bubble wrap. This was due to the majority of effector T cells settling and sticking to the surface of the bubble with more force than could reasonably be overcome by the optical tweezers. Trapped cell height, as with the silica spheres, was observed to change as a function of power, indicating two dimensional trapping, i.e. optical levitation.

Due to the focal length of the droplet lenses being less than the height of the bubble wrap, imaging of the sample was from above via a Mitutoyo 0.55 NA 100x long working distance objective. Surface tension in the trapping sample, causing it to "round up", led to lensing effects which, when coupled with the irregular surface of the hemispherical part of the bubble wrap, significantly distorted the image when viewed from above. Therefore, to counteract this, the bubble should be fully inflated with air when preparing a trapping sample, in order to smooth out the irregular surface. Additionally, lensing effects caused by droplets of the trapping sample can be minimised by injecting just enough liquid to cover the lower surface of the bubble. Thus, the sample spreads out and forms a meniscus, rather than rounding up due to surface tension. The trapped object can then be imaged through the centre of bubble wrap and meniscus, where the surfaces are relatively flat, as illustrated by figure 6.7. Optically trapped cells could, therefore, be imaged in the bubble wrap but with a decrease in image quality, figure 6.8.

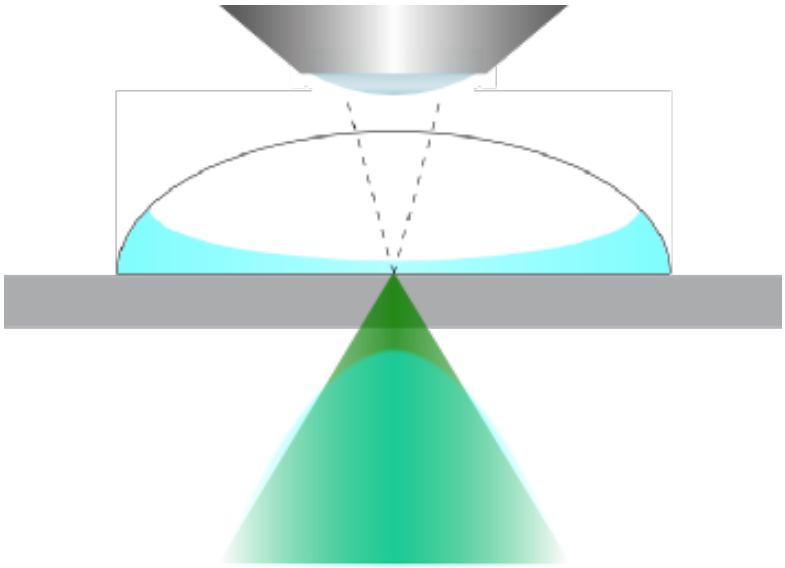

Figure 6.7: Imaging through the bubble wrap and meniscus.

6.3.5 Imaging with drip lens and phone

The CCD camera and Mitutoyo objective were removed and replaced with the doped PDMS droplet lens and the camera from a Samsung Galaxy S3 Mini smartphone. It should be noted that the vast majority of smartphone models should be suitable with this system. The trapping laser was turned off, at first, to ensure that the addition of the Sudan II dye did not negatively impact the imaging ability of the lens. Through the use of the digital zoom and macro photography autofocus features of the smartphone camera, the 3.93 μm beads were observable. Each pixel was found to correspond to (0.22 ± 0.01) μm, when the camera's 4x digital zoom was exploited.

Laser power was then turned on and slowly increased, while the smartphone camera was monitored for any sign of laser light bleeding through the filter lens. Trap power was increased until optical trapping was observed, as shown in figure 6.9. To test the filtering ability of the doped droplet lens, trap power was further increased to (112.2 ± 0.2) mW, more than 3 times the minimum trapping power required. At this power, the trapping light became

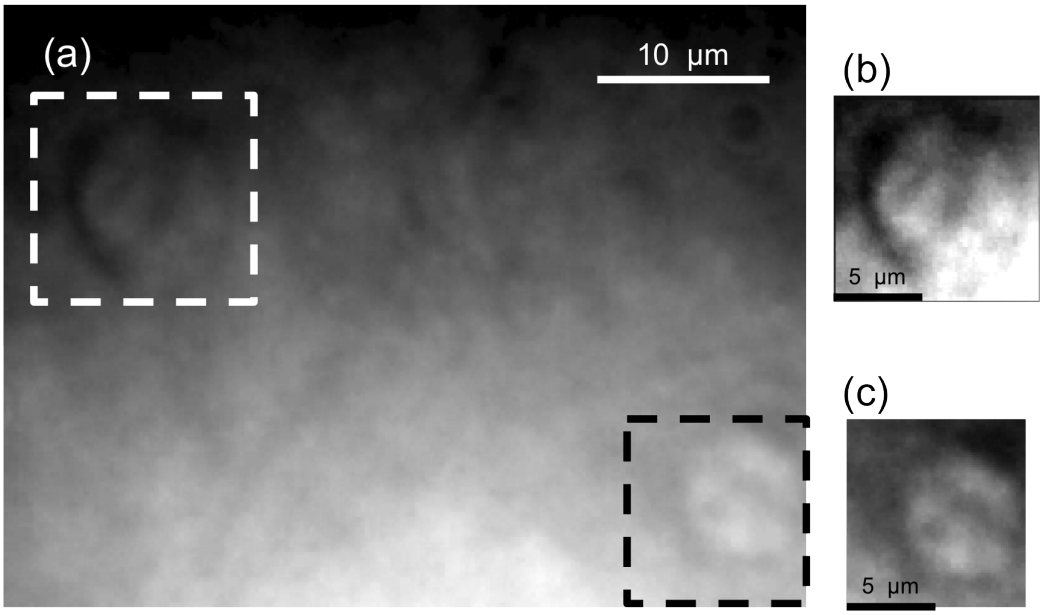

Figure 6.8: (a) Optically trapped effector T cell in bubble wrap (black box) next to untrapped cell (white box). The cell is trapped using a PDMS droplet lens and imaged with a Mitutoyo 0.55 NA 100x long working distance objective. (b) and (c) enhanced contrast view of cell bounded by, respectively, the white and black boxes. (b) and (c) have been provided for clarity.

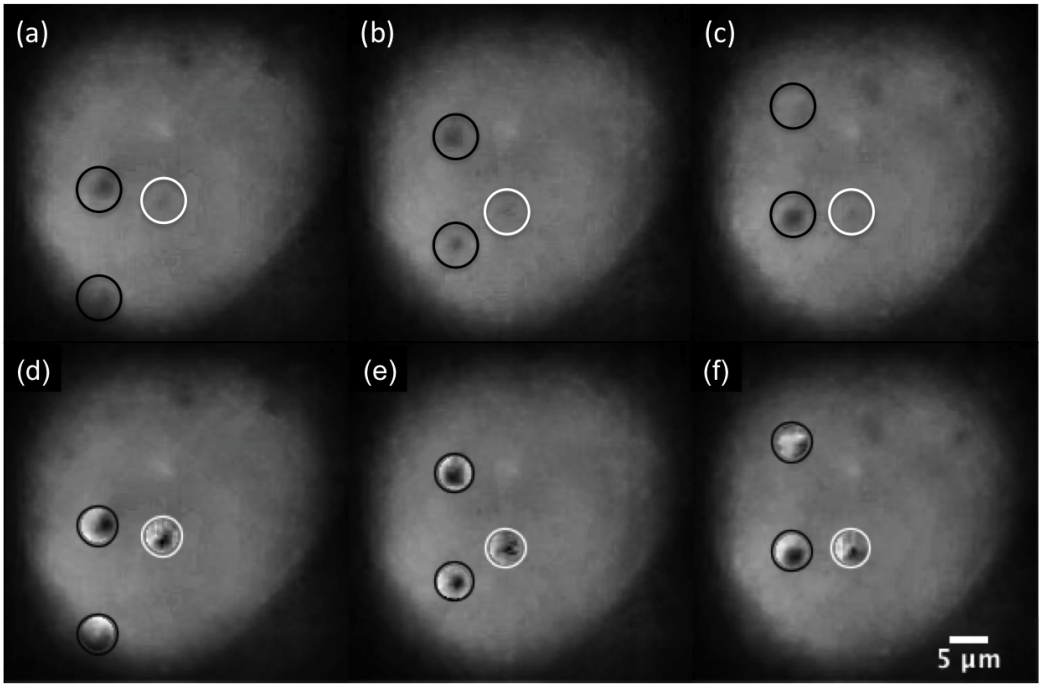

Figure 6.9: Bead trapped with a clear PDMS droplet lens and imaged with a Sudan II doped PDMS droplet lens attached to a smartphone camera. Panels (a) - (c) show an optically trapped 3.93 µm bead (circled in white) moving between two untrapped, reference beads (circled in black). Panels (d) - (f) are reproductions of the panels above, however the contrast has been adjusted within the circles for clarity.

visible through the doped PDMS droplet lens.

6.4 Conclusion and future work

The optical tweezers presented here can be fabricated with very little optical experience and at a very low cost. Qualitative and low precision quantitative measurements could be easily performed on such a system, as well as trial experiments. However, high precision or high force measurements may not be suitable. Optical trapping systems based on hanging droplets could

be constructed in any lab with access to a laser, as the materials used in fabrication are easy to handle and are readily found in many labs (including non-optics labs), or are attainable for a low cost. Although some variation in droplet lens length was observed, the material properties of PDMS lead to the droplets naturally taking similar shapes, causing the other dimensions of the lenses to be roughly constant. Due to the low trapping power, the cost of the overall optical tweezers system could be significantly reduced by exchanging the trapping source for a laser pointer, or similar, with sufficient output beam quality. Thus allowing for the use of such systems in schools or university research labs without access to significant resources. As all components of the system can be made from scratch, this would also make an excellent undergraduate laboratory project.

An imaging lens with an integrated long pass filter suitable for fluorescence detection was created through the addition of Sudan II dye. As much of the system is made from PDMS, integration with other microfluidic systems to create simple optofluidic [301] devices should be straightforward. By allowing for the simple incorporation of optical tweezers, fluorescence microscopy techniques and microfluidics this work, therefore, contributes to the burgeoning field of disposable, point-of-care diagnostic devices.

Using lego [167] or a 3D printer to create the microscope structure would be an obvious extension for such a system. Printers that print/cure polymers are currently in use, with the methodology presented here serving as a precursor for the full 3D printing of an optical tweezers system. Such a system would be much better engineered than the device presented in this chapter, thus allowing for much higher precision work, all incorporated onto a mobile phone camera. This is perfectly plausible, with the growing interest in 3D printing lab equipment, with a particular focus on the developing world, as indicated in a recent paper by Baden *et al.* [302]. Developing this low cost trapping system into a compact form would allow for field studies of aerosols: part of the development of compact, mobile, urban sensors for airborne

aerosols [303]. Thus, the initial development presented here appears to have a number of future developmental options.

Chapter 7

Conclusion and Outlook

7.1 Discussion

The work presented in this thesis has explored several applications of optical tweezers: moving from optical beam shaping and the control afforded to the end user through such techniques to more general, low-tech approaches to high-tech problems, while characterising the trapping properties of such systems. It would be the height of hubris to suggest that this thesis represents a fully completed body of work rather than providing yet another stepping stone in the long road of scientific discovery.

This thesis began with an introduction to optical trapping, discussing the history of the device and how such tools were originally developed. Optical tweezers could easily have become an experimental curiosity had it not been for their impressive ability to exert and measure forces, with a high spatial and temporal resolution, thus turning them in to a very powerful tool. As such, a brief overview of the groundbreaking research achievable through the use of optical tweezers was provided and their versatility highlighted once beam shaping techniques are employed.

The second chapter provided the theoretical basis of the optical manipulation techniques used throughout this thesis. The practicalities of designing

and constructing an optical trapping system were discussed, as well as what considerations must be made when measuring the force exerted by the tweezers. As powerful as optical tweezers are, the limits of what a single-beam trap can achieve are quickly reached. Therefore, beam shaping techniques that can be employed to circumvent this problem are discussed, with their relative advantages and disadvantages highlighted.

Each of the subsequent chapters of this thesis detailed the experimental work conducted in the lab. Each individual chapter introduced the requisite theory while providing a justification of the work performed.

Building on the theory of optical trapping in a Gaussian beam outlined previously, chapter 3 discussed trapping within a shaped beam, namely a conically refracted beam, and provided a characterisation of its trapping properties. Insertion of a biaxial crystal into the beam path transformed the single-beam, Gaussian trap optical tweezers into a set of conical refraction optical tweezers. A conically refracted beam consists of three distinct regions (the Lloyd/Poggendorff rings and the upper and lower Raman spots) and optical trapping of silica beads was demonstrated in all three locations. Through the use of power spectrum analysis, the trapping properties of each of these three trapping regimes was quantified by calculating the trap stiffnesses of 5.2 μm and 2.56 μm beads, at three different powers. It was demonstrated that the lower Raman spot had the highest trap stiffness, which increased linearly with respect to trap power, allowing it to function as a conventional, gradient force, optical trap. Trapping in the Lloyd/Poggendorff rings was achievable but led to a decrease in trap stiffness. However, trapping of particles in three dimensions was still possible and rotational control of the particle around the circumference of the rings was acquired. Sacrificing yet more trap stiffness and trapping in the upper Raman spot, led to optical levitation rather than gradient trapping. Here, guiding of a 5.2 μm particle over a distance of 35 μm by varying the trap power was demonstrated. Applications which require trapping, rotation and guiding could, therefore, be

achieved through the use of a single conically refracted beam, negating the need for complex beam shaping techniques, such as techniques requiring an SLM. Therefore, systems with higher optical throughput could be designed if power is of concern.

Due to the hollow cone at the centre of the conically refracted beam, the study of photophoretic manipulation offers an attractive research direction, as both light absorbing and light reflecting particles could be trapped simultaneously with one beam. The trapping properties of conically refracted, non-Gaussian beams could provide future interesting work. For example, the trapping properties of Gaussian and Laguerre-Gaussian beams have been compared but how does a conically refracted Laguerre-Gaussian beam differ in trapping ability from a conically refracted Gaussian beam? Furthermore, with the growing use of STED microscopy, the conically refracted beam could prove of use due to it's small dark volume that is enclosed by light.

Having demonstrated the power of static beam shaping, chapter 4 shows the versatility and control of optical traps that can be achieved by dynamic beam shaping methods. Through the use of a Microsoft Kinect connected to a Holographic Optical Tweezer (HOT), an intuitive control system using a full body interface, called HoloHands, was developed. The straightforward control system would allow a novice or non-expert user to control basic, research grade, optical tweezers. However, in its current iteration, the HoloHands system was deemed inappropriate for precision work due to the system's low trapping efficiency ($Q = 0.0045 \pm 0.0002$ for hand movement) and tendency for the trapped particle to lag behind the user's hand. Indeed, it was shown that lags of up to 0.5 s were not uncommon, which resulted in instantaneous jumps of the particle of, at times, over 1.5 μm. Therefore, the type of precision measurements demonstrated in chapter 5 would not be possible with the HoloHands system. However, qualitative experiments would be possible, as would the deployment of the system as a demonstration in schools or science centres.

Technological innovations have led to Microsoft releasing more advanced versions of their Kinect controller, which could allow for more accurate position tracking and, therefore, more accurate optical trap movement with the HoloHands program. Indeed, it would be beneficial to couple this more accurate Microsoft Kinect with a skeleton detection algorithm that is calibrated to account for person to person size variations, thus allowing for different users to move particles over the same distance and with the same precision. Further gestures could be integrated into the HoloHands code to allow for the generation of more complex beam shapes, such as LG beams, or grouping of particles to move more than one trap at a time. Additionally, employing more sophisticated, non-iterative methods of hologram generation which are more optically efficient could lead to an increase in trap stiffness and, hence, trapping performance. However, in the current version of HoloHands, it could prove interesting to bring the system to science centres and school settings and begin to engage the wider public with cutting edge physics.

An application of the trap calibration techniques demonstrated in chapter 3, combined with the holographic methods discussed in chapter 4, is given in chapter 5. More specifically, chapter 5 demonstrated the importance of optical trapping techniques as a quantitative tool in the life sciences. Through the construction, calibration and programming of a set of force measuring optical tweezers, the binding strength of integrin-ligand pairs was quantified under static conditions. It was shown that the kindlin-3 - β2 interaction affects β2 - LFA-1 binding of effector T cells. An unbinding force of (17.9 ± 0.6) pN, at an average force loading rate on the cell of (30 ± 4) pN/s, was measured for WT effector T cells. A reduction in the kindlin-3 - β2 interaction, as present in the TTT/AAA-β2-integrin KI mice, showed a significant reduction of integrin-ligand unbinding force to (10.1 ± 0.9) pN. This confirms that there is still an integrin-ligand interaction without kindlin-3 binding, but that kindlin-3 indeed affects the binding strength between single integrin-ligand pairs. The work presented in the first half of this chapter, therefore, brings

new information about the role of kindlin-3 in regulating LFA-1 mediated T cell adhesion events necessary for proper immune system function and highlights the importance of cell mechanotransduction as a therapeutic target. It has been demonstrated that receptor - ligand bonds are catch bonds, i.e. the bond can become stronger or longer lived when subjected to mechanical force [304]. Therefore, varying the force loading rate on the WT and KI cells studied could prove to be an interesting study: do integrin - ligand bonds demonstrate this catch bond behaviour in both the WT and KI cells and, if so, what would be the maximum force loading rate before the bonds begin to fail? Additionally, while bond strength under a constant force loading rate has been studied, bond lifetime under a constant applied force could provide a valuable insight into the role of kindlin-3 binding to the β2 integrin.

The system was then modified to allow for the quantification of the binding strength of these cells under shear flow conditions, where adhesion is thought to increase. By moving to a holographic based solution, the system was unable to generate the forces required to rupture the bonds. However, integrin-ligand binding under shear flow was demonstrated in the system as a proof of concept. The next stages of development for the CASBAH system would be to increase the optical trapping forces, either through improvements to the hologram generation and system throughput, or by employing anti-reflection coated, high-refractive-index titania microspheres. This would allow for the rupture force of integrin - ligand pairs under shear flow conditions to be investigated and, hopefully, quantify the increase in rupture force which has been qualitatively demonstrated.

The application of optical tweezers to problems in the life sciences is clearly of importance, but comes at a high cost, limiting their use not only in pedagogical settings but also in resource-limited research labs throughout the world. Chapter 6 addresses this issue through the presentation of a low-cost extension of optical tweezers into this field through the adaptive use of bubble wrap. Effector T cells were cultured for over a week in bubble wrap

before being optically trapped. The overall cost of the system was further reduced by fabricating lenses from hanging droplets of polydimethylsiloxane (PDMS) and the adaptive use of equipment that is often found, discarded, in the laboratory. Dying of the PDMS with Sudan II dye, prior to moulding of the lens, produced a lens with an integrated long pass filter. Therefore, a more compact system could be created, while still effectively filtering the 532 nm trapping light, allowing for the trapped objects to be imaged with a smartphone

Optical trapping systems based upon PDMS lenses and bubble wrap presents many future development possibilities, such as replacing the trapping laser with a low cost source, such as a laser pointer, or 3D printing the microscope structure. The initial development presented here can serve as a precursor to the development of devices such as a compact, mobile, urban sensors for airborne aerosols [303]. Indeed, one compelling project would be to mount such a low-cost and lightweight system on a remote controlled drone to optically trap cloud droplets or cloud condensation nuclei *in situ*, however the latter may prove too small for a PDMS lens based system without additional improvements to the trapping lens [305].

7.2 Final thoughts

The work presented in this thesis has demonstrated the strength and flexibility afforded by optical manipulation techniques, notably when beam shaping techniques are employed. The benefits of interdisciplinary research has been highlighted, especially in biophotonics, as has the associated need for easily accessible systems for the non-expert user. Of course, the research presented in this thesis does not stand alone but contributes to the ever burgeoning field of optical micromanipulation. As described in this chapter, many interesting avenues of research remain to be explored, with this thesis providing a foundation for much of this work.

Bibliography

[1] M. J. Padgett. On diffraction within a dielectric medium as an example of the Minkowski formulation of optical momentum. *Optics Express*, 16(25):20864, 2008.

[2] O. Firstenberg, T. Peyronel, Q.-Y. Liang, A. V. Gorshkov, M. D. Lukin, and V. Vuletić. Attractive photons in a quantum nonlinear medium. *Nature*, 502(7469):71–5, 2013.

[3] S. W. Hell and J. Wichmann. Breaking the diffraction resolution limit by stimulated emission: stimulated-emission-depletion fluorescence microscopy. *Optics Letters*, 19(11):780–782, 1994.

[4] R. Merkel, P. Nassoy, A. Leung, K. Ritchie, and E. Evans. Energy landscapes of receptor–ligand bonds explored with dynamic force spectroscopy. *Nature*, 397(6714):50–53, 1999.

[5] B. Liu, W. Chen, B. D. Evavold, and C. Zhu. Accumulation of dynamic catch bonds between TCR and agonist peptide-MHC triggers T cell signaling. *Cell*, 157(2):357–368, 2014.

[6] W. H. Wing. Electrostatic Trapping of Neutral Atomic Particles. *Physical Review Letters*, 45(8):631–634, 1980.

[7] M. Krishnan, N. Mojarad, P. Kukura, and V. Sandoghdar. Geometry-induced electrostatic trapping of nanometric objects in a fluid. *Nature*, 467(7316):692–695, 2010.

[8] J. Voldman, R. A. Braff, M. Toner, M. L. Gray, and M. A. Schmidt. Holding forces of single-particle dielectrophoretic traps. *Biophysical Journal*, 80(1):531–41, 2001.

[9] P. Cheng, M. J. Barrett, P. M. Oliver, D. Cetin, and D. Vezenov. Dielectrophoretic tweezers as a platform for molecular force spectroscopy in a highly parallel format. *Lab on a Chip*, 11(24):4248, 2011.

[10] J. Q. Boedicker, M. E. Vincent, and R. F. Ismagilov. Microfluidic confinement of single cells of bacteria in small volumes initiates high-density behavior of quorum sensing and growth and reveals its variability. *Angewandte Chemie International Edition*, 48(32):5908–5911, 2009.

[11] O. Sipos, K. Nagy, R. Di Leonardo, and P. Galajda. Hydrodynamic trapping of swimming bacteria by convex walls. *Physical Review Letters*, 114(25):258104, 2015.

[12] P. Glynne-Jones, R. J. Boltryk, M. Hill, N. R. Harris, and P. Baclet. Robust acoustic particle manipulation: a thin-reflector design for moving particles to a surface. *The Journal of the Acoustical Society of America*, 126(3):EL75–L79, 2009.

[13] G. Sitters, D. Kamsma, G. Thalhammer, M. Ritsch-Marte, E. J. G. Peterman, and G. J. L. Wuite. Acoustic force spectroscopy. *Nature Methods*, 12(1):47–50, 2014.

[14] K. C. Neuman and A. Nagy. Single-molecule force spectroscopy: optical tweezers, magnetic tweezers and atomic force microscopy. *Nature Methods*, 5(6):491–505, 2008.

[15] I. De Vlaminck and C. Dekker. Recent Advances in Magnetic Tweezers. *Annual Review of Biophysics*, 41(1):453–472, 2012.

[16] A. Ashkin, J. M. Dziedzic, J. E. Bjorkholm, and S. Chu. Observation of a single-beam gradient-force optical trap for dielectric particles. *Optics Letters*, 11(5):288–290, 1986.

[17] K. C. Neuman and S. M. Block. Optical trapping. *The Review of Scientific Instruments*, 75(9):2787–809, 2004.

[18] K. L. P. Sung, L. L. Steele, D. Whittermore, J. Hagan, and W. H. Akeson. Adhesiveness of human ligament fibroblasts to laminin. *Journal of Orthopaedic Research*, 13(2):166–173, 1995.

[19] K. L. P. Sung, L. Yang, D. E. Whittemore, Y. Shi, G. Jin, A. H. Hsieh, W. H. Akeson, and L. A. Sung. The differential adhesion forces of anterior cruciate and medial collateral ligament fibroblasts: effects of tropomodulin, talin, vinculin, and alpha-actinin. *Proceedings of the National Academy of Sciences of the United States of America*, 93(17):9182–7, 1996.

[20] K. L. P. Sung, D. E. Whittemore, L. Yang, D. Amiel, and W. H. Akeson. Signal pathways and ligament cell adhesiveness. *Journal of Orthopaedic Research*, 14(5):729–735, 1996.

[21] J. Huang, V. I. Zarnitsyna, B. Liu, L. J. Edwards, N. Jiang, B. D. Evavold, and C. Zhu. The kinetics of two-dimensional TCR and pMHC interactions determine T-cell responsiveness. *Nature*, 464(7290):932–936, 2010.

[22] W. Chen, J. Lou, and C. Zhu. Forcing switch from short- to intermediate- and long-lived states of the αA domain generates LFA-1/ICAM-1 catch bonds. *Journal of Biological Chemistry*, 285(46):35967–35978, 2010.

[23] S. E. Chesla, P. Selvaraj, and C. Zhu. Measuring two-dimensional receptor-ligand binding kinetics by micropipette. *Biophysical Journal*, 75(3):1553–1572, 1998.

[24] W. Chen, V. I. Zarnitsyna, K. K. Sarangapani, J. Huang, and C. Zhu. Measuring receptor–ligand binding kinetics on cell surfaces: from adhesion frequency to thermal fluctuation methods. *Cellular and Molecular Bioengineering*, 1(4):276–288, 2008.

[25] D. E. Discher and N. Mohandas. Kinematics of red cell aspiration by fluorescence-imaged microdeformation. *Biophysical journal*, 71(4):1680–1694, 1996.

[26] J. Sleep, D. Wilson, R. Simmons, and W. Gratzer. Elasticity of the red cell membrane and its relation to hemolytic disorders: an optical tweezers study. *Biophysical Journal*, 77(6):3085–95, 1999.

[27] H. S. Lek, V. L. Morrison, M. Conneely, P. A. Campbell, D. McGloin, S. Kliche, C. Watts, A. Prescott, and S. C. Fagerholm. The spontaneously adhesive leukocyte function-associated antigen-1 (LFA-1) integrin in effector T cells mediates rapid actin- and calmodulin-dependent adhesion strengthening to ligand under shear flow. *The Journal of Biological Chemistry*, 288(21):14698–708, 2013.

[28] L. Gross. Recent advances in submolecular resolution with scanning probe microscopy. *Nature Chemistry*, 3(4):273–278, 2011.

[29] J. Van Der Lit, F. Di Cicco, P. Hapala, P. Jelinek, and I. Swart. Submolecular resolution imaging of molecules by atomic force microscopy: the influence of the electrostatic force. *Physical Review Letters*, 116(9):2–6, 2016.

[30] C. Chu, E. Celik, F. Rico, and V. T. Moy. Elongated membrane tethers, individually anchored by high affinity $\alpha 4\beta 1$/VCAM-1 complexes, are the quantal units of monocyte arrests. *PLoS ONE*, 8(5):e64187, 2013.

[31] T. G. Kuznetsova, M. N. Starodubtseva, N. I. Yegorenkov, S. A. Chizhik, and R. I. Zhdanov. Atomic force microscopy probing of cell elasticity. *Micron*, 38(8), 2007.

[32] Y. Liu, J. Strauss, and T. A. Camesano. Adhesion forces between Staphylococcus epidermidis and surfaces bearing self-assembled monolayers in the presence of model proteins. *Biomaterials*, 29(33):4374–82, 2008.

[33] M. Rief, M. Gautel, F Oesterhelt, J. M. Fernandez, and H. E. Gaub. Reversible unfolding of individual titin immunoglobulin domains by AFM. *Science*, 276(5315):1109–1112, 1997.

[34] J. M Fernandez and H. B. Li. Force-clamp spectroscopy monitors the folding trajectory of a single protein. *Science*, 303(5664):1674–1678, 2004.

[35] D. J. Billingsley, W. A. Bonass, N. Crampton, J. Kirkham, and N. H. Thomson. Single-molecule studies of DNA transcription using atomic force microscopy. *Physical biology*, 9(2):021001, 2012.

[36] S. Nawaz, P. Sánchez, K. Bodensiek, S. Li, M. Simons, and I. A. T. Schaap. Cell visco-elasticity measured with AFM and optical trapping at sub-micrometer deformations. *PloS one*, 7(9):e45297, 2012.

[37] M. F. Crommie, C. P. Lutz, and D. M. Eigler. Confinement of electrons to quantum corrals on a metal surface. *Science*, 262(5131):218–220, 1993.

[38] D. S. Gray, J. L. Tan, J. Voldman, and C. S. Chen. Dielectrophoretic registration of living cells to a microelectrode array. *Biosensors and Bioelectronics*, 19(7):771–780, 2004.

[39] A. Rosenthal and J. Voldman. Dielectrophoretic traps for single-particle patterning. *Biophysical journal*, 88(3):2193–2205, 2005.

[40] A. Jesacher, S. Fürhapter, S. Bernet, and M. Ritsch-Marte. Size selective trapping with optical "cogwheel" tweezers. *Optics express*, 12(17):4129–4135, 2004.

[41] M. C. Wu. Optoelectronic tweezers. *Nature Photonics*, 5(6):322–324, 2011.

[42] A. T. Ohta, P. Y. Chiou, H. L. Phan, S. W. Sherwood, J. M. Yang, A. N. K. Lau, H. Y. Hsu, A. Jamshidi, and M. C. Wu. Optically controlled cell discrimination and trapping using optoelectronic tweezers. *IEEE Journal of Selected Topics in Quantum Electronics*, 13(2):235–243, 2007.

[43] H. Y. Hsu, A. T. Ohta, P. Y. Chiou, A. Jamshidi, S. L. Neale, and M. C. Wu. Phototransistor-based optoelectronic tweezers for dynamic cell manipulation in cell culture media. *Lab Chip*, 10(2):165–172, 2010.

[44] S. L. Neale, M. Mazilu, J. I. B. Wilson, K. Dholakia, and T. F. Krauss. The resolution of optical traps created by Light Induced Dielectrophoresis (LIDEP). *Optics express*, 15(20):12619–12626, 2007.

[45] S. L. Neale, A. T. Ohta, H. Y. Hsu, J. K. Valley, A. Jamshidi, and M. C. Wu. Trap profiles of projector based optoelectronic tweezers (OET) with HeLa cells. *Optics express*, 17(7):5232–9, 2009.

[46] J. K. Valley, A. T. Ohta, H. Y. Hsu, S. L. Neale, A. Jamshidi, and M. C. Wu. Optoelectronic tweezers as a tool for parallel single-cell ma-

nipulation and stimulation. *IEEE Transactions on Biomedical Circuits and Systems*, 3(6):424–431, 2009.

[47] M. Woerdemann, C. Alpmann, M. Esseling, and C. Denz. Advanced optical trapping by complex beam shaping. *Laser & Photonics Reviews*, 7(6):839–854, 2013.

[48] P. Y. Chiou, A. T. Ohta, and M. C. Wu. Massively parallel manipulation of single cells and microparticles using optical images. *Nature*, 436(7049):370–372, 2005.

[49] P. H. Jones, O. M. Marago, and G. Volpe. *Optical Tweezers Principles and Applications*. Cambridge University Press, Cambridge, 2015.

[50] J. K. Fisher, J. Cribb, K. V. Desai, L. Vicci, B. Wilde, K. Keller, R. M. Taylor, J. Haase, K. Bloom, E. Timothy O'Brien, and R. Superfine. Thin-foil magnetic force system for high-numerical-aperture microscopy. *Review of Scientific Instruments*, 77(2):023702, 2006.

[51] J. Yan, D. Skoko, and J. F. Marko. Near-field-magnetic-tweezer manipulation of single DNA molecules. *Physical Review E - Statistical, Nonlinear, and Soft Matter Physics*, 70(1):1–5, 2004.

[52] N. Ribeck and O. A. Saleh. Multiplexed single-molecule measurements with magnetic tweezers. *Review of Scientific Instruments*, 79(9):094301, 2008.

[53] T. R. Strick, V. Croquette, and D. Bensimon. Single-molecule analysis of DNA uncoiling by a type II topoisomerase. *Nature*, 404(6780):901–904, 2000.

[54] D. A. Koster, K. Palle, E. S. M. Bot, M.-A. Bjornsti, and N. H. Dekker. Antitumour drugs impede DNA uncoiling by topoisomerase I. *Nature*, 448(7150):213–217, 2007.

[55] M. P. MacDonald, A. Cochran, C. J. Weijer, D. Hughes, C. Demore, G. Brodie, and G. C. Spalding. Sonotweezers: complementing the size and force spectra of optical trapping. 199(2010), 2011.

[56] M. Groschl. Ultrasonic separation of suspended particles - part I: fundamentals. *Acustica*, 84:432–447, 1998.

[57] M. Hill and N. R. Harris. Ultrasonic Particle Manipulation. In *Microfluidic Technologies for Miniaturized Analysis Systems*, pages 357–392. Springer US, Boston, MA.

[58] T. Laurell, F. Petersson, and A. Nilsson. Chip integrated strategies for acoustic separation and manipulation of cells and particles. *Chem. Soc. Rev.*, 36(3):492–506, 2007.

[59] F. Petersson, A. Nilsson, C. Holm, H. Jonsson, and T. Laurell. Separation of lipids from blood utilizing ultrasonic standing waves in microfluidic channels. *The Analyst*, 129(10):938–943, 2004.

[60] C. E. Démoré, Y. Qiu, S. Cochran, P. Glynne-Jones, C. Ye, and M. Hill. Transducer arrays for ultrasonic particle manipulation. *Proceedings - IEEE Ultrasonics Symposium*, (c):412–415, 2010.

[61] C. R. P. Courtney, C.-K. Ong, B. W. Drinkwater, P. D. Wilcox, C. Demore, S. Cochran, P. Glynne-Jones, and M. Hill. Manipulation of microparticles using phase-controllable ultrasonic standing waves. *The Journal of the Acoustical Society of America*, 128(4):EL195–EL199, 2010.

[62] A. Ashkin. History of optical trapping and manipulation of small-neutral particle, atoms, and molecules. *IEEE Journal of Selected Topics in Quantum Electronics*, 6(6):841–856, 2000.

[63] A. Ashkin. Acceleration and trapping of particles by radiation pressure. *Physical Review Letters*, 24(4):156–159, 1970.

[64] A. Ashkin and J. M. Dziedzic. Optical levitation by radiation pressure. *Applied Physics Letters*, 19(8):283–285, 1971.

[65] T. N. Buican, M. J. Smyth, H. A. Crissman, G. C. Salzman, C. C. Stewart, and J. C. Martin. Automated single-cell manipulation and sorting by light trapping. *Applied Optics*, 26(24):5311–6, 1987.

[66] A. Constable, J. Kim, J. Mervis, F. Zarinetchi, and M. Prentiss. Demonstration of a fiber-optical light-force trap. *Optics Letters*, 18(21):1867–1869, 1993.

[67] R. Omori, T. Kobayashi, and A. Suzuki. Observation of a single-beam gradient-force optical trap for dielectric particles in air. *Optics Letters*, 22(11):816–8, 1997.

[68] K. Svoboda, C. F. Schmidt, B. J. Schnapp, and S. M. Block. Direct observation of kinesin stepping by optical trapping interferometry. *Nature*, 365(6448):721–727, 1993.

[69] J. R. Moffitt, Y. R. Chemla, S. B. Smith, and C. Bustamante. Recent advances in optical tweezers. *Annual Review of Biochemistry*, 77(1):205–28, 2008.

[70] M. J. Padgett, J. E. Molloy, and D. McGloin, editors. *Optical tweezers methods and applications*. CRC Press, 2010.

[71] I. Verdeny, A. Farré, J. Mas, and C. López-Quesada. Optical trapping : A review of essential concepts Trampas ópticas : Revisión de conceptos esenciales. *Optica Pura Y Aplicada*, 44(3):527–551, 2011.

[72] R. W. Bowman and M. J. Padgett. Optical trapping and binding. *Reports on Progress in Physics*, 76(2):026401, 2013.

[73] J. Kepler. *De cometis libelli tres*. Augustae Vindelicorum, 1619.

[74] K. Dholakia, G. C. Spalding, and M. P. MacDonald. Optical tweezers: the next generation. *Physics World*, 15:31–35, 2002.

[75] J. C. Maxwell. *Treatise on electricity and magnetism*. Calrendon Press, 1873.

[76] D. Normile. Mission to probe Venus's curious winds and test solar sail for propulsion. *Science*, 328(5979):677–677, 2010.

[77] P. N. Lebedev. Untersuchungen über die druckkräfte des lichtes. *Ann Der Physik*, 6:433 – 458, 1901.

[78] E. F. Nichols and G. F. Hull. A preliminary communication on the pressure of heat and light radiation. *Physical Review (Series I)*, 13(5):307–320, 1901.

[79] M. Jeng. A selected history of expectation bias in physics. *American Journal of Physics*, 74(7):578, 2006.

[80] A. Einstein. Zur quantentheorie der stahlung (on the quantum mechanics of radaiation). *Physikalische Zeitschrift*, 18:121 – 128, 1917.

[81] M. D. Summers, J. P. Reid, and D. McGloin. Optical guiding of aerosol droplets. *Optics Express*, 14(14):6373–6380, 2006.

[82] G. Guccione, M. Hosseini, S. Adlong, M. T. Johnsson, J. Hope, B. C. Buchler, and P. K. Lam. Scattering-free optical levitation of a cavity mirror. *Physical Review Letters*, 111(18):183001, 2013.

[83] K. G. Libbrecht and E. D. Black. Toward quantum-limited position measurements using optically levitated microspheres. *Physics Letters A*, 321(2):99–102, 2004.

[84] S. Singh, G. A. Phelps, D. S. Goldbaum, E. M. Wright, and P. Meystre. All-optical optomechanics: an optical spring mirror. *Physical Review Letters*, 105(21):213602, 2010.

[85] W. H. Wright, G. J. Sonek, and M. W. Berns. Parametric study of the forces on microspheres held by optical tweezers. *Applied Optics*, 33(9):1735–1748, 1994.

[86] A. Ashkin. Forces of a single-beam gradient laser trap on a dielectric sphere in the ray optics regime. *Biophysical Journal*, 61(2):569–582, 1992.

[87] J. Harris and G. McConnell. Optical trapping and manipulation of live T cells with a low numerical aperture lens. *Optics express*, 16(18):14036–14043, 2008.

[88] P. H. Jones, E. Stride, and N. Saffari. Trapping and manipulation of microscopic bubbles with a scanning optical tweezer. *Applied Physics Letters*, 89(8):081113, 2006.

[89] G. C. Spalding, P. M. Dahl, C. E. Démoré, Z. Yang, P. Glynne-Jones, A. Melzer, S. Cochran, and M. P. MacDonald. Mapping out tractor beams: topological angular momentum and reduced axial flux; gradient versus non-conservative forces. In Kishan Dholakia and Gabriel C. Spalding, editors, *Proceedings of SPIE*, volume 8810, page 881004, sep 2013.

[90] Z. Yang. *Optical and acoustic beam shaping for imaging and manipulation.* PhD thesis, University of Dundee, 2015.

[91] D. B. Ruffner and D. G. Grier. Optical conveyors: a class of active tractor beams. *Physical Review Letters*, 109(16):163903, 2012.

[92] C. E. Démoré, P. M. Dahl, Z. Yang, P. Glynne-Jones, A. Melzer, S. Cochran, M. P. MacDonald, and G. C. Spalding. Acoustic Tractor Beam. *Physical Review Letters*, 112(17):174302, 2014.

[93] C. E. Démoré, Z. Yang, A. Volovick, S. Cochran, M. P. MacDonald, and G. C. Spalding. Mechanical evidence of the orbital angular momentum to energy ratio of vortex beams. *Physical Review Letters*, 108(19):194301, 2012.

[94] D. Bardell. The first record of microscopic observations. *BioScience*, 33(1):36 – 38, 1983.

[95] J. E. Molloy, J. E. Burns, J. Kendrick-Jones, R. T. Tregear, and D. C. White. Movement and force produced by a single myosin head. *Nature*, 378(6553):209–12, 1995.

[96] J. Guck, R. Ananthakrishnan, H. Mahmood, T. J. Moon, C. C. Cunningham, and J. Käs. The optical stretcher: a novel laser tool to micromanipulate cells. *Biophysical Journal*, 81(2):767–84, 2001.

[97] M. D. Wang, H. Yin, R. Landick, J. Gelles, and S. M. Block. Stretching DNA with optical tweezers. *Biophysical Journal*, 72(3):1335–46, 1997.

[98] C. G. Baumann, S. B. Smith, V. A. Bloomfield, and C. Bustamante. Ionic effects on the elasticity of single DNA molecules. *Proceedings of the National Academy of Sciences of the United States of America*, 94(12):6185–90, 1997.

[99] M. W. Berns. A history of laser scissors (microbeams). *Methods in Cell Biology*, 82, 2007.

[100] R. Wiegand, G. Weber, K. Zimmermann, S. Monajembashi, J. Wolfrum, and K. O. Greulich. Laser-induced fusion of mammalian cells and plant protoplasts. *Journal of Cell Science*, 88 (Pt 2):145–149, 1987.

[101] S. Sato, E. Higurashi, Y. Taguchi, and H. Inaba. Achievement of laser fusion of biological cells using UV pulsed dye laser beams. *Applied Physics B Photophysics and Laser Chemistry*, 54:531–533, 1992.

[102] M. K. Kreysing, T. R. Kießling, A. W. Fritsch, C. Dietrich, J. Guck, and J. A. Käs. The optical cell rotator. *Optics Express*, 16(21):16984–16992, 2008.

[103] T. R. Kießling, R. Stange, J. A. Käs, and A. W. Fritsch. Thermorheology of living cells - impact of temperature variations on cell mechanics. *New Journal of Physics*, 15:045026, 2013.

[104] T. Yasokawa, I. Ishimaru, M. Kondo, S. Kuriyama, T. Masaki, K. Takegawa, and N. Tanaka. A method for measuring the three-dimensional refractive-index distribution of single cells using proximal two-beam optical tweezers and a phase-shifting Mach-Zehnder interferometer. *Optical Review*, 14(4):161–164, 2007.

[105] A. M. Packer, L. E. Russell, H. W. P. Dalgleish, and M. Häusser. Simultaneous all-optical manipulation and recording of neural circuit activity with cellular resolution in vivo. *Nature Methods*, 12(2):140 – 146, 2015.

[106] M. C. Zhong, X. B. Wei, J. H. Zhou, Z. Q. Wang, and Y. M. Li. Trapping red blood cells in living animals using optical tweezers. *Nature Communications*, 4:1768, 2013.

[107] K. Svoboda and S. M. Block. Biological applications of optical forces. *Annual Review of Biophysics and Biomolecular Structure*, 23:247–85, 1994.

[108] G. Pesce, A. Sasso, and S. Fusco. Viscosity measurements on micron-size scale using optical tweezers. *Review of Scientific Instruments*, 76:115105, 2005.

[109] C. Hertlein, L. Helden, A. Gambassi, S. Dietrich, and C. Bechinger. Direct measurement of critical Casimir forces. *Nature*, 451:172–175, 2008.

[110] R. Di Leonardo, F. Ianni, and G. Ruocco. Colloidal attraction induced by a temperature gradient. *Langmuir*, 25(8):4247–4250, 2009.

[111] A. D. Ward, M. G. Berry, C. D. Mellor, and C. D. Bain. Optical sculpture: controlled deformation of emulsion droplets with ultralow interfacial tensions using optical tweezers. *Chemical Communications*, (43):4515–4517, 2006.

[112] A. Einstein. *Investigations on the theory of the Brownian movement.* Methuen Co., 1926.

[113] K. Berg-Sørensen and H. Flyvbjerg. The colour of thermal noise in classical Brownian motion: a feasibility study of direct experimental observation. *New Journal of Physics*, 7(38), 2005.

[114] R. M. Simmons, J. T. Finer, S. Chu, and J. A. Spudich. Quantitative measurements of force and displacement using an optical trap. *Biophysical Journal*, 70(4):1813–1822, 1996.

[115] A. Rohrbach and E. H. K. Stelzer. Three-dimensional position detection of optically trapped dielectric particles. *Journal of Applied Physics*, 91(8):5474, 2002.

[116] O. Otto, C. Gutsche, F. Kremer, and U. F. Keyser. Optical tweezers with 2.5 kHz bandwidth video detection for single-colloid electrophoresis. *The Review of Scientific Instruments*, 79(2 Pt 1):023710, 2008.

[117] F. Gittes and C. F. Schmidt. Interference model for back-focal-plane displacement detection in optical tweezers. *Optics Letters*, 23(1):7–9, 1998.

[118] Y. Deng, J. Bechhoefer, and N. R. Forde. Brownian motion in a modulated optical trap. *Journal of Optics A: Pure and Applied Optics*, 9:S256–S263, 2007.

[119] A. Jannasch, M. Mahamdeh, and E. Schäffer. Inertial effects of a small Brownian particle cause a colored power spectral density of thermal noise. *Physical Review Letters*, 107(22):228301, 2011.

[120] J. Arlt, V. Garces-Chavez, W. Sibbett, and K. Dholakia. Optical micromanipulation using a Bessel light beam. *Optics Communications*, 197:239–245, 2001.

[121] H. He, M. E. J. Friese, N. R. Heckenberg, and H. Rubinsztein-Dunlop. Direct observation of transfer of angular momentum to absorptive particles from a laser beam with a phase singularity. *Physical Review Letters*, 75(5):826–829, 1995.

[122] L. Paterson, M. P. MacDonald, J. Arlt, W. Sibbett, P. E. Bryant, and K. Dholakia. Controlled rotation of optically trapped microscopic particles. *Science*, 292(5518):912–4, 2001.

[123] A. Turpin, V. Shvedov, C. Hnatovsky, Y. V. Loiko, J. Mompart, and W. Krolikowski. Optical vault : a reconfigurable bottle beam based on conical refraction of light. *Optics Express*, 21(22):26335–26340, 2013.

[124] C. McDougall, R. Henderson, D. J. Carnegie, G. S. Sokolovskii, E. U. Rafailov, and D. McGloin. Flexible particle manipulation techniques with conical refraction-based optical tweezers. *Proc. SPIE*, 8458:845824–845824–7, 2012.

[125] S.-H. Lee, Y. Roichman, and D. G Grier. Optical solenoid beams. *Optics Express*, 18(7):6988–93, 2010.

[126] M. Woerdemann, C. Alpmann, and C. Denz. Optical assembly of microparticles into highly ordered structures using Ince-Gaussian beams. *Applied Physics Letters*, 98(11):111101, 2011.

[127] Z. Zheng, B. F. Zhang, H. Chen, J. Ding, and H. T. Wang. Optical trapping with focused Airy beams. *Applied Optics*, 50(1):43–49, 2011.

[128] J. A. Rodrigo, T. Alieva, E. Abramochkin, and I. Castro. Shaping of light beams along curves in three dimensions. *Optics Express*, 21(18):20544–55, 2013.

[129] A. P. Porfirev and R. V. Skidanov. Optical trapping and manipulation of light-absorbing particles by means of a Hermite–Gaussian laser beam. *Journal of Optical Technology*, 82(9):587, 2015.

[130] J. E. Curtis, B. A. Koss, and D. G. Grier. Dynamic holographic optical tweezers. *Optics Communications*, 207:169–175, 2002.

[131] K. Visscher, S. P. Gross, and S. M. Block. Construction of multiple-beam optical traps with nanometer-resolution position sensing. *IEEE Journal of Selected Topics in Quantum Electronics*, 2(4):1066–1076, 1996.

[132] D. P. O'Dwyer, C. F. Phelan, K. E. Ballantine, Y. P. Rakovich, J. G. Lunney, and J. F. Donegan. Conical diffraction of linearly polarised light controls the angular position of a microscopic object. *Optics Express*, 18(26):27319–26, 2010.

[133] D. P. O'Dwyer, K. E. Ballantine, C. F. Phelan, J. G. Lunney, and J. F. Donegan. Optical trapping using cascade conical refraction of light. *Optics Express*, 20(19):21119 – 25, 2012.

[134] C. McDonald, C. McDougall, E. U. Rafailov, and D. McGloin. Characterizing conical refraction optical tweezers. *Optics Letters*, 39(23):6691–4, 2014.

[135] M. P. MacDonald, G. C. Spalding, and K. Dholakia. Microfluidic sorting in an optical lattice. *Nature*, 426(6965):421–424, 2003.

[136] Y. Y. Sun, L. S. Ong, and X. C. Yuan. Composite-microlens-array-enabled microfluidic sorting. *Applied Physics Letters*, 89(14):141108, 2006.

[137] D. R. Burnham. *Microscopic applications of holographic beam shaping and studies of optically trapped aerosols.* PhD thesis, University of St. Andrews, 2009.

[138] E. Hecht. *Optics.* Addison Wesley, 4th edition, 2002.

[139] C. McDougall. *Advanced photonic methodologies for the in vitro manipulation of cellular systems.* Phd thesis, University of St. Andrews, 2010.

[140] L. Novotny and B. Hecht. *Principles of Nano-Optics.* Cambridge University Press, Cambridge, 2006.

[141] K. Svoboda and S. M. Block. Optical trapping of metallic Rayleigh particles. *Optics Letters*, 19(13):930–932, 1994.

[142] A. Rohrbach and E. H. K. Stelzer. Optical trapping of dielectric particles in arbitrary fields. *Journal of the Optical Society of America. A*, 18(4):839–853, 2001.

[143] A. R. Zakharian, P. Polynkin, M. Mansuripur, and J. V. Moloney. Single-beam trapping of micro-beads in polarized light: numerical simulations. *Optics Express*, 14(8):3660–3676, 2006.

[144] J. W. Goodman. *Introduction to Fourier Optics.* McGraw-Hill Higher Education, 2nd edition, 1996.

[145] J. A. Lock and G. Gouesbet. Generalized Lorenz-Mie theory and applications. *Journal of Quantitative Spectroscopy and Radiative Transfer*, 110(11):800–807, 2009.

[146] T. A. Nieminen, V. L. Y. Loke, A. B. Stilgoe, G. Knöner, A. M. Brańczyk, N. R. Heckenberg, and H. Rubinsztein-Dunlop. Optical tweezers computational toolbox. *Journal of Optics A*, 9(8):S196–S203, 2007.

[147] R. C. Gauthier. Computation of the optical trapping force using an FDTD based technique. *Optics Express*, 13(10):3707–3718, 2005.

[148] S. H. Simpson and S. Hanna. Optical trapping of spheroidal particles in Gaussian beams. *Journal of the Optical Society of America. A*, 24(2):430–443, 2007.

[149] S. M. Barnett and R. Loudon. On the electromagnetic force on a dielectric medium. *Journal of Physics B: Atomic, Molecular and Optical Physics*, 39(15):S671–S684, 2006.

[150] A. Callegari, M. Mijalkov, A. B. Gököz, and G. Volpe. Computational toolbox for optical tweezers in geometrical optics. *Journal of the Optical Society of America B*, 32(5):B11, 2015.

[151] D. C. Appleyard, K. Y. Vandermeulen, H. Lee, and M. J. Lang. Optical trapping for undergraduates. *American Journal of Physics*, 75(1):5 – 14, 2007.

[152] S. P. Smith. Inexpensive optical tweezers for undergraduate laboratories. *American Journal of Physics*, 67(1):26–35, 1999.

[153] F. C. Cheong, B. Sun, R. Dreyfus, J. Amato-Grill, K. Xiao, L. Dixon, and D. G. Grier. Flow visualization and flow cytometry with holographic video microscopy. *Optics Express*, 17(15):13071–13079, 2009.

[154] J. Crocker and D. G. Grier. Methods of digital video microscopy for colloidal studies. *Journal of Colloid and Interface Science*, 179(1):298–310, 1996.

[155] R. W. Bowman, G. M. Gibson, A. Linnenberger, D. B. Phillips, J. A. Grieve, D. M. Carberry, S. Serati, M. J. Miles, and M. J. Padgett. Red tweezers: fast, customisable hologram generation for optical tweezers. *Computer Physics Communications*, 185(1):268–273, 2014.

[156] D. G. Grier. A revolution in optical manipulation. *Nature*, 424(6950):810–816, 2003.

[157] S.-H. Lee and D. G. Grier. Holographic microscopy of holographically trapped three-dimensional structures. *Optics Express*, 15(4):1505–12, 2007.

[158] J. E. Molloy and M. J. Padgett. Lights, action: optical tweezers. *Contemporary Physics*, 43(4):241–258, 2002.

[159] D. McGloin. Optical tweezers: 20 years on. *Philosophical transactions. Series A, Mathematical, physical, and engineering sciences*, 364(1849):3521–3537, 2006.

[160] S. C. Kuo. Using optics to measure biological forces and mechanics. *Traffic*, 2(11):757–763, 2001.

[161] W. Koechner. *Solid State Laser Engineering*. Springer, New York, 6th edition, 2006.

[162] W. M. Lee, P. J. Reece, R. F. Marchington, N. K. Metzger, and K. Dholakia. Construction and calibration of an optical trap on a fluorescence optical microscope. *Nature Protocols*, 2(12):3226–38, 2007.

[163] N. English. *Choosing and Using a Refracting Telescope*. Patrick Moore's Practical Astronomy Series. Springer New York, New York, NY, 2011.

[164] J. B. Pawley, editor. *Handbook Of Biological Confocal Microscopy*. Springer US, Boston, MA, 2006.

[165] A. K. J. V. Köhler. New method of illumination for phomicrographical purposes. *Journal of the Royal Microscopical Society*, 14(2):261 – 262, 1894.

[166] P. N. Prasad. *Introduction to Biophotonics*. John Wiley & Sons, Inc., Hoboken, NJ, USA, 2003.

[167] F. Quercioli, B. Tiribilli, A. Mannoni, and S. Acciai. Optomechanics with LEGO. *Applied Optics*, 37(16):3408–16, 1998.

[168] Z. Zhang and C. H. Menq. Three-dimensional particle tracking with subnanometer resolution using off-focus images. *Applied Optics*, 47(13):2361–2370, 2008.

[169] R. Bowman, D. Preece, G. Gibson, and M. Padgett. Stereoscopic particle tracking for 3D touch, vision and closed-loop control in optical tweezers. *Journal of Optics*, 13(4), 2011.

[170] K. Berg-Sørensen and H. Flyvbjerg. Power spectrum analysis for optical tweezers. *Review of Scientific Instruments*, 75(3):594, 2004.

[171] M. W. Allersma, F. Gittes, M. J. DeCastro, R. J. Stewart, and C. F. Schmidt. Two-dimensional tracking of ncd motility by back focal plane interferometry. *Biophysical Journal*, 74(2 Pt 1):1074–85, 1998.

[172] E. L. Florin, A. Pralle, E. H. K. Stelzer, and J. K. H. Hörber. Photonic force microscope calibration by thermal noise analysis. *Applied Physics A: Materials Science and Processing*, 66(7):75–78, 1998.

[173] A. Rohrbach, C. Tisher, D. Neumayer, E. L. Florin, and E. H. K. Stelzer. Trapping and tracking a local probe with a photonic force microscope. *Review of Scientific Instruments*, 75(6):2197–2210, 2004.

[174] P. S. Alves and M. S. Rocha. Videomicroscopy calibration of optical tweezers by position autocorrelation function analysis. *Applied Physics B*, 107(2):375–378, 2012.

[175] I. M. Tolić-Nørrelykke, K. Berg-Sørensen, and H. Flyvbjerg. MatLab program for precision calibration of optical tweezers. *Computer Physics Communications*, 159(3):225–240, 2004.

[176] P. M. Hansen, I. M. Tolić-Nørrelykke, H. Flyvbjerg, and K. Berg-Sørensen. tweezercalib 2.0: Faster version of MatLab package for precise calibration of optical tweezers. *Computer Physics Communications*, 174(6):518–520, 2006.

[177] P. M. Hansen, I. M. Tolic-Nørrelykke, H. Flyvbjerg, and K. Berg-Sørensen. tweezercalib 2.1: Faster version of MatLab package for precise calibration of optical tweezers. *Computer Physics Communications*, 175(8):572–573, 2006.

[178] M. Lankers, J. Popp, G. Rössling, and W. Kiefer. Raman investigations on laser-trapped gas bubbles. *Chemical Physics Letters*, 277(4):331–334, 1997.

[179] V. Garcés-Chávez, D. McGloin, H. Melville, W. Sibbett, and K. Dholakia. Simultaneous micromanipulation in multiple planes using a self-reconstructing light beam. *Nature*, 419(6903):145–147, 2002.

[180] P. Prentice, M. P. MacDonald, T. Frank, A. Cuschieri, G. C. Spalding, W. Sibbett, P. A. Campbell, and K. Dholakia. Manipulation and filtration of low index particles with holographic Laguerre-Gaussian optical trap arrays. *Optics Express*, 12(4):593–600, 2004.

[181] W. M. Lee, X. C. Yuan, and W. C. Cheong. Optical vortex beam shaping by use of highly efficient irregular spiral phase plates for optical micromanipulation. *Optics Letters*, 29(15):1796–1798, 2004.

[182] M. J. Lang, C. L. Asbury, J. W. Shaevitz, and S. M. Block. An automated two-dimensional optical force clamp for single molecule studies. *Biophysical Journal*, 83(1):491–501, 2002.

[183] C. Mio, T. Gong, A. Terray, and D. W. M. Marr. Design of a scanning laser optical trap for multiparticle manipulation. *Review of Scientific Instruments*, 71(5):2196, 2000.

[184] A. Lafong, W. J. Hossack, J. Arlt, T. J. Nowakowski, and N. D. Read. Time-multiplexed Laguerre-Gaussian holographic optical tweezers for biological applications. *Optics Express*, 14(7):3065–72, 2006.

[185] G. Siviloglou and J. Broky. Observation of accelerating Airy beams. *Physical Review Letters*, 99(21):213901, 2007.

[186] J. Liesener, M. Reicherter, T. Haist, and H. J. Tiziani. Multi-functional optical tweezers using computer-generated holograms. *Optics Communications*, 185(1-3):77–82, 2000.

[187] R. W. Gerchberg and W. O. Saxton. A practical algorithm for the determination of phase from image and diffraction plane pictures. *Optik*, 35(2):237–246, 1972.

[188] L. Brandt, C. Muldoon, T. Thiele, J. Dong, E. Brainis, and A. Kuhn. Spatial light modulators for the manipulation of individual atoms. *Applied Physics B*, 102(3):443–450, 2011.

[189] A. R. Faustov, M. R. Webb, and D. R. Walt. Note: Toward multiple addressable optical trapping. *Review of Scientific Instruments*, 81(2):026109, 2010.

[190] Y. Jiang, I. Oh, Y. Matsumoto, Y. Hosokawa, and H. Masuhara. Spatial light modulating and multi-trapping with a DMD. *Modern Physics Letters B*, 21(4):175–181, 2007.

[191] T. Čižmár, M. Mazilu, and K. Dholakia. In situ wavefront correction and its application to micromanipulation. *Nature Photonics*, 4(6):388–394, 2010.

[192] W. R. Hamilton. Third supplement to an essay on the theory of systems of rays. *Transactions of the Royal Irish Academy*, 17(Part 1):1–144, 1837.

[193] H. Lloyd. On the Phenomena Presented by Light in its Passage Along the Axes of Biaxial Crystals. *Transactions of the Royal Irish Academy*, 17(Part 1):145 – 157, 1837.

[194] M. Mansuripur. *Classical Optics and its Applications*. Chapter 29. Cambridge University Press, 2nd edition, 2009.

[195] M. Born and E. Wolf. *Principles of Optics*. Chapter 14. Pergamon Press, 6th edition, 1980.

[196] M. V. Berry, M. R. Jeffrey, and J. G. Lunney. Conical diffraction: observations and theory. *Proceedings of the Royal Society A: Mathematical, Physical and Engineering Sciences*, 462(2070):1629–1642, 2006.

[197] M. V. Berry and M. R. Jeffrey. Chapter 2 Conical diffraction: Hamilton's diabolical point at the heart of crystal optics. *Progress in Optics*, 50(07):13–50, 2007.

[198] V. Peet. The far-field structure of Gaussian light beams transformed by internal conical refraction in a biaxial crystal. *Optics Communications*, 311:150–155, 2013.

[199] G. S. Sokolovskii, D. J. Carnegie, T. K. Kalkandjiev, and E. U. Rafailov. Conical refraction: new observations and a dual cone model. *Optics Express*, 21(9):11125–11131, 2013.

[200] S. D. Grant, S. A. Zolotovskaya, W. A. Gillespie, T. K. Kalkandjiev, and A. Abdolvand. Azimuthally and radially polarized light in conical diffraction. *Optics Letters*, 39(7):1988–91, 2014.

[201] Y. Hayamizu. Analysis of internal conical refraction using ray tracing formulas for the biaxial crystal. *Optical Review*, 13(4):169–183, 2006.

[202] W. D. Callister. *Materials Science and Engineering: An Intoduction.* John Wiley & Sons, Inc., 7th edition, 2007.

[203] A. Turpin, Y. V. Loiko, T. K. Kalkandjiev, and J. Mompart. Conical refraction: fundamentals and applications. *Laser & Photonics Reviews*, 10(5):750–771, 2016.

[204] S. D. Grant. *Conical diffraction photonics.* PhD thesis, University of Dundee, 2016.

[205] A. Turpin, Y. V. Loiko, A. Peinado, A. Lizana, T. K. Kalkandjiev, J. Campos, and J. Mompart. Polarization tailored novel vector beams based on conical refraction. *Optics Express*, 23(5):5704, 2015.

[206] G. M. Gibson, J. Leach, S. Keen, A. J. Wright, and M. J. Padgett. Measuring the accuracy of particle position and force in optical tweezers using high-speed video microscopy. *Optics Express*, 16(19):14561, 2008.

[207] V. Peet. Biaxial crystal as a versatile mode converter. *Journal of Optics*, 12(9):095706, 2010.

[208] V. Peet. Conical refraction and formation of multiring focal image with Laguerre–Gauss light beams. *Optics Letters*, 36(15):2913, 2011.

[209] V. Peet. Experimental study of internal conical refraction in a biaxial crystal with Laguerre–Gauss light beams. *Journal of Optics*, 16(7):075702, 2014.

[210] M. Esseling, P. Rose, C. Alpmann, and C. Denz. Photophoretic trampoline—Interaction of single airborne absorbing droplets with light. *Applied Physics Letters*, 101(13):131115, 2012.

[211] C. Pacoret, R. W. Bowman, G. M. Gibson, S. Haliyo, D. Carberry, A. Bergander, S. Régnier, and M. J. Padgett. Touching the microworld with force-feedback optical tweezers. *Optics Express*, 17(12):10259–64, 2009.

[212] K. Onda and F. Arai. Multi-beam bilateral teleoperation of holographic optical tweezers. *Optics Express*, 20(4):3633–41, 2012.

[213] J. A. Grieve, A. Ulcinas, S. Subramanian, G. M. Gibson, M. J. Padgett, D. M. Carberry, and M. J. Miles. Hands-on with optical tweezers: a multitouch interface for holographic optical trapping. *Optics Express*, 17(5):3595–602, 2009.

[214] R. W. Bowman, G. M. Gibson, D. Carberry, L. Picco, M. J. Miles, and M. J. Padgett. iTweezers: optical micromanipulation controlled by an Apple iPad. *Journal of Optics*, 13(4):044002, 2011.

[215] G. Whyte, G. M. Gibson, J. Leach, M. J. Padgett, D. Robert, and M. Miles. An optical trapped microhand for manipulating micron-sized objects. *Optics Express*, 14(25):12497–502, 2006.

[216] C. McDonald, M. McPherson, C. McDougall, and D. McGloin. HoloHands: games console interface for controlling holographic optical manipulation. *Journal of Optics*, 15(3):035708, 2013.

[217] C. Muhiddin, D. B. Phillips, M. J. Miles, L. Picco, and D. M. Carberry. Kinect 4 ... holographic optical tweezers. *Journal of Optics*, 15(7):75302, 2013.

[218] L. Shaw, D. Preece, and H. Rubinsztein-Dunlop. Kinect the dots: 3D control of optical tweezers. *Journal of Optics*, 15(7):075303, 2013.

[219] E. R. Dufresne, G. C. Spalding, M. T. Dearing, S. A. Sheets, and D. G. Grier. Computer-generated holographic optical tweezer arrays. *Review of Scientific Instruments*, 72(3):1810, 2001.

[220] http://rsb.info.nih.gov/ij/ last accessed: 23/11/2016.

[221] M. Montes-Usategui, E. Pleguezuelos, J. Andilla, and E. Martín-Badosa. Fast generation of holographic optical tweezers by random mask encoding of Fourier components. *Optics Express*, 14(6):2101–7, 2006.

[222] https://www.leapmotion.com/ last accessed: 23/11/2016.

[223] Z. Tomori, M. Antalik, P. Kesa, J. Kanka, P. Jakl, M. Sery, S. Bernatova, and P. Zemanek. Holographic Raman tweezers controlled by hand gestures and voice commands. *Optics and Photonics Journal*, 03(02):331–336, 2013.

[224] S. Chu, J. E. Bjorkholm, A. Ashkin, and A. Cable. Experimental observation of optically trapped atoms. *Physical Review Letters*, 57(3):314–317, 1986.

[225] A. Ashkin and J. M. Dziedzic. Optical trapping and manipulation of viruses and bacteria. *Science*, 235(4795):1517–1520, 1987.

[226] A. Ashkin, J. M. Dziedzic, and T. Yamane. Optical trapping and manipulation of single cells using infrared laser beams. *Nature*, 330(6150):769–771, 1987.

[227] A. Ashkin and J. M. Dziedzic. Internal cell manipulation using infrared laser traps. *Proceedings of the National Academy of Sciences*, 86(20):7914–8, 1989.

[228] H. Liang, W. H. Wright, S. Cheng, W. He, and M. W. Berns. Micromanipulation of chromosomes in PTK2 cells using laser microsurgery (optical scalpel) in combination with laser-induced optical force (optical tweezers). *Experimental Cell Research*, 204(1):110–120, 1993.

[229] E. A. Abbondanzieri, W. J. Greenleaf, J. W. Shaevitz, R. Landick, and S. M. Block. Direct observation of base-pair stepping by RNA polymerase. *Nature*, 438(7067):460–465, 2005.

[230] S. de Lorenzo, M. Ribezzi-Crivellari, J. R. Arias-Gonzalez, S. B. Smith, and F. Ritort. A temperature-jump optical trap for single-molecule manipulation. *Biophysical Journal*, 108(12):2854–2864, 2015.

[231] F. Kohler and A. Rohrbach. Surfing along filopodia: a particle transport revealed by molecular-scale fluctuation analyses. *Biophysical Journal*, 108(9):2114–2125, 2015.

[232] M. L. Dustin. T cells have a light touch. *Biophysical Journal*, 108(9):2089–2090, 2015.

[233] H. Yang, X. Gou, Y. Wang, T. M. Fahmy, A. Y. H. Leung, J. Lu, and D. Sun. A dynamic model of chemoattractant-induced cell migration. *Biophysical Journal*, 108(7):1645–1651, 2015.

[234] H. Ulbrich, E. E. Eriksson, and L. Lindbom. Leukocyte and endothelial cell adhesion molecules as targets for therapeutic interventions in inflammatory disease. *Trends in Pharmacological Sciences*, 24(12):640–647, 2003.

[235] A. D. Luster, R. Alon, and U. H. von Andrian. Immune cell migration in inflammation: present and future therapeutic targets. *Nature Immunology*, 6(12):1182–1190, 2005.

[236] S. L. Goodman and M. Picard. Integrins as therapeutic targets. *Trends in Pharmacological Sciences*, 33(7):405–412, 2012.

[237] A. Sigal, D. A. Bleijs, V. Grabovsky, S. J. van Vliet, O. Dwir, C. G. Figdor, Y. van Kooyk, and R. Alon. The LFA-1 integrin supports rolling adhesions on ICAM-1 under physiological shear flow in a permissive cellular environment. *The Journal of Immunology*, 165(1):442–452, 2000.

[238] R. Evans, I. Patzak, L. Svensson, K. De Filippo, K. Jones, A. McDowall, and N. Hogg. Integrins in immunity. *Journal of Cell Science*, 122(2):215–25, 2009.

[239] M. MacPherson, H. S. Lek, V. L. Morrison, and S. C. Fagerholm. Leukocyte beta2-integrins; genes and disease. *Journal of Genetic Syndromes & Gene Therapy*, 04(06):1000154, 2013.

[240] R. O. Hynes. Integrins: bidirectional, allosteric signaling machines. *Cell*, 110(6):673–687, 2002.

[241] C. T. Lefort and K. Ley. Neutrophil arrest by LFA-1 activation. *Frontiers in Immunology*, 3(00157):1–10, 2012.

[242] R. Alon and S. W. Feigelson. Chemokine-triggered leukocyte arrest: force-regulated bi-directional integrin activation in quantal adhesive contacts. *Current Opinion in Cell Biology*, 24(5):670–676, 2012.

[243] R. Alon and K. Ley. Cells on the run: shear-regulated integrin activation in leukocyte rolling and arrest on endothelial cells. *Current Opinion in Cell Biology*, 20(5):525–532, 2008.

[244] M. Moser, M. Bauer, S. Schmid, R. Ruppert, S. Schmidt, M. Sixt, H. V. Wang, M. Sperandio, and R. Fässler. Kindlin-3 is required for beta2 integrin-mediated leukocyte adhesion to endothelial cells. *Nature Medicine*, 15(3):300–305, 2009.

[245] B. H. Luo, C. V. Carman, and T. A. Springer. Structural basis of integrin regulation and signaling. *Annual Review of Immunology*, 25(1):619–647, 2007.

[246] W. A. Muller. Getting leukocytes to the site of inflammation. *Veterinary Pathology*, 50(1):7–22, 2013.

[247] C. A. Janeway Jr, P. Travers, M. Walport, and M. J. Shlomchik. *Immunobiology: the immune system in health and disease.*, chapter Principles of innate and adaptive immunity. Garland Science, New York, 5th edition, 2001.

[248] A Etzioni. *Immune-mediated diseases: from theory to therapy*, chapter Leukocyte adhesion deficiencies: molecular basis, clinical findings, and therapeutic options. Springer, New York, 2007.

[249] A. Etzioni. Genetic etiologies of leukocyte adhesion defects. *Current Opinion in Immunology*, 21(5):481–486, 2009.

[250] S. Hanna and A. Etzioni. Leukocyte adhesion deficiencies. *Annals of the New York Academy of Sciences*, 1250(1):50–55, 2012.

[251] V. L. Morrison, M. Macpherson, T. Savinko, H. S. Lek, A. Prescott, and S. C. Fagerholm. The beta2 integrin-kindlin-3 interaction is essential for T cell homing but dispensable for T cell activation in vivo. *Blood*, 122(8):1428–1437, 2013.

[252] C. Capo, F. Garrouste, A. M. Benoliel, P. Bongrand, A. Ryter, and G. I. Bell. Concanavalin-a-mediated thymocyte agglutination: a model for a quantitative study of cell adhesion. *Journal of Cell Science*, 56(1):21–48, 1982.

[253] D. F. Tees, R. E. Waugh, and D. A. Hammer. A microcantilever device to assess the effect of force on the lifetime of selectin-carbohydrate bonds. *Biophysical journal*, 80(2):668–682, 2001.

[254] R. Alon, S. W. Feigelson, E. Manevich, D. M. Rose, J. Schmitz, D. R. Overby, E. Winter, V. Grabovsky, V. Shinder, B. D. Matthews, M. Sokolovsky-Eisenberg, D. E. Ingber, M. Benoit, and M. H. Ginsberg. $\alpha 4\beta 1$ -dependent adhesion strengthening under mechanical strain

is regulated by paxillin association with the $\alpha 4$ -cytoplasmic domain. *The Journal of Cell Biology*, 171(6):1073–1084, 2005.

[255] X. Fu, Y. Xu, C. Wu, V. T. Moy, and X. F. Zhang. Anchorage-dependent binding of integrin I-domain to adhesion ligands. *Journal of Molecular Recognition*, 28(6):385–392, 2015.

[256] X. Zhang, S. E. Craig, H. Kirby, M. J. Humphries, and V. T. Moy. Molecular basis for the dynamic strength of the integrin $\alpha 4\beta 1$/VCAM-1 interaction. *Biophysical Journal*, 87(5):3470–3478, 2004.

[257] A. Farré, A. van der Horst, G. A. Blab, B. P. B Downing, and N. R. Forde. Stretching single DNA molecules to demonstrate high-force capabilities of holographic optical tweezers. *Journal of Biophotonics*, 3(4):224–33, 2010.

[258] A. van der Horst, B. P. B. Downing, and N. R. Forde. Position and intensity modulations in holographic optical traps created by a liquid crystal spatial light modulator. In *Advances in Imaging*, page OMB3. Optical Society of America, 2009.

[259] A. Farré, M. Shayegan, C. López-Quesada, G. A. Blab, M. Montes-Usategui, N. R. Forde, and E. Martín-Badosa. Positional stability of holographic optical traps. *Optics Express*, 19(22):21370–21384, 2011.

[260] A. van der Horst and N. R. Forde. Calibration of dynamic holographic optical tweezers for force measurements on biomaterials. *Optics Express*, 16(25):20987–1003, 2008.

[261] R. Di Leonardo, F. Ianni, and G. Ruocco. Computer generation of optimal holograms for optical trap arrays. *Optics Express*, 15(4):1913–1922, 2007.

[262] M. Persson, D. Engström, and M. Goksör. Reducing the effect of pixel crosstalk in phase only spatial light modulators. *Optics Express*, 20(20):22334, 2012.

[263] M. Polin, K. Ladavac, S. H. Lee, Y. Roichman, and D. G. Grier. Optimized holographic optical traps. *Optics Express*, 13(15):5831–5845, 2005.

[264] N. McAlinden, D. G. Glass, O. R. Millington, and A. J. Wright. Accurate position tracking of optically trapped live cells. *Biomedical Optics Express*, 5(4):1026, 2014.

[265] N. McAlinden, D. G. Glass, O. Millington, and A. J. Wright. Viability studies of optically trapped T-cells. In *SPIE Proceedings Vol. 8097*, page 80970J, September 2011.

[266] J. Glückstad. Optical manipulation: sculpting the object. *Nature Photonics*, 5(1):7–8, 2011.

[267] A. Jannasch, A. F. Demirörs, P. D. J. van Oostrum, A. van Blaaderen, and E. Schäffer. Nanonewton optical force trap employing anti-reflection coated, high-refractive-index titania microspheres. *Nature Photonics*, 6(7):469–473, 2012.

[268] V. Bormuth, A. Jannasch, M. Ander, C. M. van Kats, A. van Blaaderen, J. Howard, and E. Schäffer. Optical trapping of coated microspheres. *Optics Express*, 16(18):13831–13844, 2008.

[269] F. M. Fazal and S. M. Block. Optical tweezers study life under tension. *Nature Photonics*, 5(6):318–321, 2011.

[270] D. R. Burnham and D. McGloin. Holographic optical trapping of aerosol droplets. *Optics Express*, 14(9):4176–82, 2006.

[271] A. Pralle, E. L. Florin, E. H. K. Stelzer, and J. K. H. Hörber. Local viscosity probed by photonic force microscopy. *Applied Physics A: Materials Science and Processing*, 66(7):S71–S73, 1998.

[272] A. W. Martinez, S. T. Phillips, M. J. Butte, and G. M. Whitesides. Patterned paper as a platform for inexpensive, low-volume, portable bioassays. *Angewandte Chemie - International Edition*, 46(8):1318–1320, 2007.

[273] A. W. Martinez, S. T. Phillips, and G. M. Whitesides. Three-dimensional microfluidic devices fabricated in layered paper and tape. *Proceedings of the National Academy of Sciences of the United States of America*, 105(50):19606–19611, 2008.

[274] A. K. Ellerbee, S. T. Phillips, A. C. Siegel, K. A. Mirica, A. W. Martinez, P. Striehl, N. Jain, M. Prentiss, and G. M. Whitesides. Quantifying colorimetric assays in paper-based microfluidic devices by measuring the transmission of light through paper. *Analytical Chemistry*, 81(20):8447–8452, 2009.

[275] B. J. Toley, B. McKenzie, T. Liang, J. R. Buser, P. Yager, and E. Fu. Tunable-delay shunts for paper microfluidic devices. *Analytical Chemistry*, 85(23):11545–11552, 2013.

[276] S. Ramachandran, E. Fu, B. Lutz, and P. Yager. Long-term dry storage of an enzyme-based reagent system for ELISA in point-of-care devices. *The Analyst*, 139(6):1456–62, 2014.

[277] A. P. Wong, M. Gupta, S. S. Shevkoplyas, and G. M Whitesides. Egg beater as centrifuge: isolating human blood plasma from whole blood in resource-poor settings. *Lab on a Chip*, 8(12):2032–2037, 2008.

[278] K. R. Paton, E. Varrla, C. Backes, R. J. Smith, U. Khan, A. O'Neill, C. Boland, M. Lotya, O. M. Istrate, P. King, T. Higgins, S. Barwich,

P. May, P. Puczkarski, I. Ahmed, M. Moebius, H. Pettersson, E. Long, J. Coelho, S. E. O'Brien, E. K. McGuire, B. M. Sanchez, G. S. Duesberg, N. McEvoy, T. J. Pennycook, C. Downing, A. Crossley, V. Nicolosi, and J. N. Coleman. Scalable production of large quantities of defect-free few-layer graphene by shear exfoliation in liquids. *Nature Materials*, 13(6):624–30, 2014.

[279] C. S. Boland, U. Khan, C. Backes, A. O'Neill, J. McAuley, S. Duane, R. Shanker, Y. Liu, I. Jurewicz, A. B. Dalton, and J. N. Coleman. Sensitive, high-strain, high-rate, bodily motion sensors based on graphene-rubber composites. *ACS Nano*, 8(9):8819–8830, 2014.

[280] D. N. Breslauer, R. N. Maamari, N. A. Switz, W. A. Lam, and D. A. Fletcher. Mobile phone based clinical microscopy for global health applications. *PloS one*, 4(7):e6320, 2009.

[281] L. Bellina and E. Missoni. Mobile cell-phones (M-phones) in telemicroscopy: increasing connectivity of isolated laboratories. *Diagnostic Pathology*, 4(1):1–4, 2009.

[282] Z. J. Smith, K. Chu, A. R. Espenson, M. Rahimzadeh, A. Gryshuk, M. Molinaro, D. M. Dwyre, S. Lane, D. Matthews, and S. Wachsmann-Hogiu. Cell-phone-based platform for biomedical device development and education applications. *PloS one*, 6(3):e17150, 2011.

[283] A. Skandarajah, C. D. Reber, N. A. Switz, and D. A. Fletcher. Quantitative imaging with a mobile phone microscope. *PloS one*, 9(5):e96906, 2014.

[284] W. M. Lee, A. Upadhya, P. J. Reece, and T. G. Phan. Fabricating low cost and high performance elastomer lenses using hanging droplets. *Biomedical Optics Express*, 5(5):1626–35, 2014.

[285] O. Hofmann, X. Wang, A. Cornwell, S. Beecher, A. Raja, D. D. C. Bradley, A. J. deMello, and J. C. deMello. Monolithically integrated dye-doped PDMS long-pass filters for disposable on-chip fluorescence detection. *Lab on a Chip*, 6(8):981–7, 2006.

[286] C. McDonald and D. McGloin. Low-cost optical manipulation using hanging droplets of PDMS. *RSC Advances*, 5(68):55561–55565, 2015.

[287] C. McDonald and D. McGloin. Bubble wrap for optical trapping and cell culturing. *Biomedical Optics Express*, 6(10):3757, 2015.

[288] D. K. Bwambok, D. C. Christodouleas, S. A. Morin, H. Lange, S. T. Phillips, and G. M. Whitesides. Adaptive use of bubble wrap for storing liquid samples and performing analytical assays. *Analytical Chemistry*, 86(15):7478–85, 2014.

[289] J. L. Wilbur, R. J. Jackman, and G. M. Whitesides. Elastomeric optics. *Chemistry of Materials*, 8(7):1380–1385, 1996.

[290] K.-H. Jeong, J. Kim, and L. Lee. Biologically inspired artificial compound eyes. *Science*, 312(5773):557–61, 2006.

[291] Y. Gambin, O. Legrand, and S. R. Quake. Microfabricated rubber microscope using soft solid immersion lenses. *Applied Physics Letters*, 88(17):174102, 2006.

[292] J.-J. Kim, Y. Lee, H. G. Kim, K.-J. Choi, H.-S. Kweon, S. Park, and K.-H. Jeong. Biologically inspired LED lens from cuticular nanostructures of firefly lantern. *Proceedings of the National Academy of Sciences*, 109(46):18674–18678, 2012.

[293] H. Ren, S. Xu, and S. T. Wu. Effects of gravity on the shape of liquid droplets. *Optics Communications*, 283(17):3255–3258, 2010.

[294] F. A. Chowdhury and K. J. Chau. Variable focus microscopy using a suspended water droplet. *Journal of Optics*, 14(5):055501, 2012.

[295] R. Tadmor, P. Bahadur, A. Leh, H. E. N'guessan, R. Jaini, and L. Dang. Measurement of lateral adhesion forces at the interface between a liquid drop and a substrate. *Physical Review Letters*, 103(26):266101, 2009.

[296] T. Krupenkin, S. Yang, and P. Mach. Tunable liquid microlens. *Applied Physics Letters*, 82(3):316–318, 2003.

[297] Y. L. Sung, J. Jeang, C. H. Lee, and W. C. Shih. Fabricating optical lenses by inkjet printing and heat-assisted in situ curing of polydimethylsiloxane for smartphone microscopy. *Journal of Biomedical Optics*, 20(4):047005, 2015.

[298] N. Chronis, G. Liu, K. H. Jeong, and L. Lee. Tunable liquid-filled microlens array integrated with microfluidic network. *Optics Express*, 11(19):2370–2378, 2003.

[299] D. Erickson, D. O'Dell, L. Jiang, V. Oncescu, A. Gumus, S. Lee, M. Mancuso, and S. Mehta. Smartphone technology can be transformative to the deployment of lab-on-chip diagnostics. *Lab on a Chip*, 14(17):3159–3164, 2014.

[300] C. L. Bliss, J. N. McMullin, and C. J. Backhouse. Integrated wavelength-selective optical waveguides for microfluidic-based laser-induced fluorescence detection. *Lab on a chip*, 8(1):143–51, 2008.

[301] P. Fei, Z. Chen, Y. Men, A. Li, Y. Shen, and Y. Huang. A compact optofluidic cytometer with integrated liquid-core/PDMS-cladding waveguides. *Lab on a Chip*, 12(19):3700, 2012.

[302] T. Baden, A. M. Chagas, G. Gage, T. Marzullo, L. L. Prieto-Godino, and T. Euler. Open Labware: 3-D Printing Your Own Lab Equipment. *PLOS Biology*, 13(3):e1002086, 2015.

[303] M. Budde, M. Busse, and M. Beigl. Investigating the use of commodity dust sensors for the embedded measurement of particulate matter. *Networked Sensing Systems (INSS), 2012 Ninth International Conference on Networked Sensing*, pages 1–4, 2012.

[304] W. Thomas. Catch Bonds in Adhesion. *Annual Review of Biomedical Engineering*, 10(1):39–57, 2008.

[305] F. Tampieri and C. Tomasi. Size distribution models of fog and cloud droplets in terms of the modified gamma function. *Tellus*, 28(4):333–347, 1976.